5-27-2010

Material Synthesis and Characterization on Low-Dimensional Cobaltates

Hao Sha
Florida International University, hsha001@fiu.edu

DOI: 10.25148/etd.FI10081001

FLORIDA INTERNATIONAL UNIVERSITY

Miami, Florida

MATERIAL SYNTHESIS AND CHARACTERIZATION ON LOW-DIMENSIONAL COBALTATES

A dissertation submitted in partial fulfillment of the

requirements for the degree of

DOCTOR OF PHILOSOPHY

in

PHYSICS

by

Hao Sha

2010

To: Dean Kenneth Furton
College of Arts and Sciences

This dissertation, written by Hao Sha, and entitled Material Synthesis and Characterization on Low-Dimensional Cobaltates, having been approved in respect to style and intellectual content, is referred to you for judgment.

We have read this dissertation and recommend that it be approved.

_____
Xuewen Wang

_____
Wenzhi Li

_____
Yesim Darici

_____
Chunlei Wang

_____
Jiandi Zhang, Major Professor

Date of Defense: May 27, 2010

The dissertation of Hao Sha is approved.

_____
Dean Kenneth Furton
College of Arts and Sciences

_____
Interim Dean Kevin O'Shea
University Graduate School

Florida International University, 2010

DEDICATION

I dedicate this thesis to my wife, Feng Qiu, my parents, Ruyun Shi and Changmei Sha and my sister, Xiaoyi Sha. Without their patience, understanding, support, and most of all love, the completion of this work would not have been possible.

Also, I dedicate this thesis to my daughter, Allison Rudi Sha, whose birth has brought wonderful fun, great motivation and bright inspiration into my life.

ACKNOWLEDGMENTS

There are many people I would like to thank, who have contributed in some way towards this thesis. First I wish to express my gratitude to my supervisor, Professor Jiandi Zhang. His extraordinary passion for research, weariless endeavor, great knowledge and resourcefulness has been such an inspiration. He has provided insight and clear guidance throughout, and his support has been invaluable. I also want to thank Professor Rongying Jin who provided me all the opportunities in the laboratory at ORNL, and let me stay at her home during my experiment at Oak Ridge. She has also given me a lot of invaluable suggestions during my experiments and paper writing. I also would like to thank Feng Ye who trained and helped me in my early days of neutron scattering experience. I would like to acknowledge my committee members for their time and advice.

I also would like to thank my committee members for their encouragement, support and suggestions. The discussion with Dr. Xuewen Wang, Dr. Wenzi Li and Dr. Yesim Darici gave me both theoretical and experimental suggestions. It is also my great pleasure that Dr. Chunlei Wang joined my committee and guided me from engineering point of view.

I would like to give my special thanks to the Dissertation Year Fellowship (DYF) provided by the Graduate School in FIU. It greatly supported me in writing this dissertation in the final year of my Ph.D study financially.

I am deeply grateful to my colleagues at FIU that have provided the environment for sharing their experiences about the problem issues involved as well as participated in stimulating discussions. Most of my research work has been conducted at High Flux

Isotope Reactor (HFIR) and NIST Center for Neutron Research (NCNR). I am deeply indebted to Dr. Jaime Fenandez-Baca and Dr. Jeff Lynn who have provided so many opportunities. I would like to express my gratitude to Dr. Qingzheng Huang and Vasile O. Garlea who helped me solving the lattice and magnetic structures. The assistance and discussions offered by my collaborators have been very helpful, and I therefore wish to thank David Mandrus, Brian Sales, Pengcheng Dai, Mark Lumsdon, Ying Chen, Ward Plummer, Elbio Dagotto, Zhixian Zhou, Matthew Stone, Minghu Pan. The people in our group are so nice and helpful, so thanks to Lei Cai, Chenxi Lu, Dalgis Mesa, Haizhong Guo, Yanxin Liu, En Cai, Yi Li, Chiyat Yau, Darwin Urbina, Sarah Bryan, Stephane Stacco.

Finally I would like to thank my family. The love, encouragement and support from my beloved wife Feng has made everything so enjoyable. A very special thought is devoted to my parents, my sister and my daughter, Allison.

ABSTRACT OF THE DISSERTATION

MATERIAL SYNTHESIS AND CHARACTERIZATION

ON LOW-DIMENSIONAL COBALTATES

by

Hao Sha

Florida International University, 2010

Miami, Florida

Professor Jiandi Zhang, Major Professor

In this thesis, results of the investigation of a new low-dimensional cobaltates $Ba_{2-x}Sr_xCoO_4$ are presented. The synthesis of both polycrystalline and single crystalline compounds using the methods of conventional solid state chemical reaction and floating-zone optical furnace is first introduced. Besides making polycrystalline powders, we successfully, for the first time, synthesized large single crystals of Ba_2CoO_4. Single crystals were also obtained for Sr doped $Ba_{2-x}Sr_xCoO_4$. Powder and single crystal x-ray diffraction results indicate that pure Ba_2CoO_4 has a monoclinic structure at room temperature. With Sr doping, the lattice structure changes to orthorhombic when $x \geq 0.5$ and to tetragonal when $x = 2.0$. In addition, Ba_2CoO_4 and Sr_2CoO_4, have completely different basic building blocks in the structure. One is CoO_4 tetrahedron and the later is CoO_6 octahedron, respectively.

Electronic and magnetic properties were characterized and discussed. The magnetic susceptibility, specific heat and thermal conductivity show that Ba_2CoO_4 has an antiferromagnetic (AF) ground state with an AF ordering temperature $T_N = 25$ K.

However, the magnitude of the Néel temperature T_N is significantly lower than the Curie-Weiss temperature ($|\theta| \sim 110$ K), suggesting either reduced-dimensional magnetic interactions and/or the existence of magnetic frustration. The AF interaction persists in all the samples with different doping concentrations. The Néel temperature doesn't vary much in the monoclinic structure regime but decreases when the system enters orthorhombic.

Magnetically, Ba_2CoO_4 has an AF insulating ground state while Sr_2CoO_4 has a ferromagnetic (FM) metallic ground state. Neutron powder refinement results indicate a magnetic structure with the spin mostly aligned along the *a*-axis. The result from a μ-spin rotation/relaxation (μ^+SR) experiment agrees with our refinement. It confirms the AF order in the *ab*-plane. We also studied the spin dynamics and its anisotropy in the AF phase. The results from inelastic neutron scattering show that spin waves have a clear dispersion along *a*-axis but not along *c*-axis, indicating spin anisotropy.

This work finds the strong spin-lattice coupling in this novel complex material. The interplay between the two degrees of freedom results an interesting phase diagram. Further research is needed when large single crystal samples are available.

TABLE OF CONTENTS

LIST OF TABLES

LIST OF FIGURES

CHAPTER 1

INTRODUCTION

1.1 Brief Overview

The past several years have seen extensive experimental and theoretical activities in correlated electron systems. Transition metal oxides (TMOs) play a pivotal role in the search for understanding because of the exotic properties they exhibit. The optimal functionalities present immense opportunities and formidable challenges in condensed matter physics and materials science [1]. Materials in which electrons are strongly correlated exhibit many complex and collective phenomena, including high-temperature superconductivity (HTSC), metal-insulator transition (MIT), colossal magnetoresistance (CMR), and quantum phase transition (QPT) [1–14]. The signature of these materials is the multitude of competing ground states that can be turned or manipulated by chemical doping, structural manipulations, strain induction, or the application of external stimulus, such as pressure, electric or magnetic fields, etc. The interest of these materials stems from the richness of their novel properties, the complexity of underlying physics and the promise of technological applications.

Understanding of the various types of exotic behaviors exhibited by correlated electron systems has dramatically challenged our views of solids. Generally, a correlated electron material is one in which the potential energy is comparable to the kinetic energy. This leads to spectacular properties that result from the multitude of competing ground states - the equilibrium between phases is very subtle and small perturbations can induce large responses. It is believed that the physics behind these phenomena is a complex interplay between charge, lattice, orbital, and spin degrees of freedom, which creates electronic-to-magnetic, or magnetic-to-structural coupled phase transitions. Experiments have revealed unexpected spatial inhomogeneities and

multiscale modulations of charge, spin, orbital, and polarization in many complex transition-metal oxides such as cuprates, manganites, and ruthenates. Understanding these materials requires probing not only both local and long-range ordering but also low-level excitations and quasiparticles such as phonons, polarons, magnons, as well as their interactions.

Strongly correlated electron systems indeed have proved to be rather difficult to understand. For example, so far no one has been able to put forward a complete theory of high-temperature superconductivity. Indeed, many phenomena associated with strong electron correlations have proved difficult to explain, in large part a result of the fact that there are often several competing degrees of freedom in many of the technologically important classes of materials. The competition between different interactions can lead to quite complex phase diagrams, and any successful theory must be able to explain the physical properties of the system in all of these phases.

Faced with such a complicated set of problems, physicists have sought to find model systems in which one kind of interaction dominates over the others. By gathering experimental data on such systems, and devising theoretical models to explain their behavior, it is hoped that the understanding of more complicated materials can be improved iteratively.

In this chapter, I will consider some of the emergent phenomena that are observed in complex materials, such as superconductivity, colossal magnetoresistance and quantum phase transition. The motivation of this thesis and some prototype oxide compounds, which motivated me to work on the $Ba_{2-x}Sr_xCoO_4$ system, will be introduced thereafter.

1.2 Collective Interactions in Complex Materials

1.2.1 *Superconductivity*

Superconductivity below 4 K was first observed experimentally in mercury in 1911 by Kamerlingh Onnes [15]. There are a number of physical properties that are necessary conditions for a material to be a superconductor, and which distinguish such a material from a perfect conductor. The most obvious property of a superconductor is that below a critical temperature, T_C, the material has zero electrical resistance. This does not, however, distinguish it from a perfect conductor. A superconductor additionally exhibits the Meissner effect, whereby magnetic flux is completely excluded from the material's interior[1] and it becomes a perfect diamagnet, provided that any applied magnetic field is not above the material's critical field, H_C.

BCS Superconductivity

Following the Onnes' initial discovery of superconductivity in mercury many more materials were found to superconduct, though it was not until 1957 that a theoretical understanding of the phenomenon was achieved, when Bardeen, Cooper, and Schrieffer [16–18] proposed what has come to be known as BCS theory.

Put simply, in BCS theory electrons become bound together by exchanging virtual phonons and forming 'Cooper-pairs', decreasing their energy by doing so. These Cooper pairs are Bosons and therefore the Pauli Exclusion Principle does not apply, so if

[1] In fact magnetic flux does penetrate a short distance into the interior of a superconductor, although the flux decays exponentially with the distance from the surface. This finite penetration of flux can be phenomenologically explained using the London equations, which are themselves derived from Maxwell's equations. Note that the London equations do not encompass any microscopic information about the superconducting state.

one pair of electrons can save energy by becoming bound together, the other electrons are likely to do the same. Since Cooper pairs are Bosons there is no restriction on the number that exists in any particular quantum state. The binding energy (reduction in energy of the electron pair) is greatest if electrons with equal but opposite momentum become bound together.

Consider adding two electrons, with momenta $\boldsymbol{k}_1$ and $\boldsymbol{k}_2$ respectively, to a metal at zero temperature. If electron 1 emits a phonon with wavevector $\boldsymbol{q}$ then $\boldsymbol{k}_1 \rightarrow \boldsymbol{k}_1 - \boldsymbol{q} = \boldsymbol{k}_1'$, and $\boldsymbol{k}_2 \rightarrow \boldsymbol{k}_2 + \boldsymbol{q} = \boldsymbol{k}_2'$, and by conservation of momentum $\boldsymbol{K} = \boldsymbol{k}_1 + \boldsymbol{k}_2 = \boldsymbol{k}_1' + \boldsymbol{k}_2'$. Now the phonon has energy $\sim\hbar\omega_{Debye} \ll E_F$, and in adition, because of the Pauli exclusion principle, $k_F \leq k_1'$ and $k_2' \leq k_F + q$. The number of available states into which the electrons can be scattered is a maximum for $\boldsymbol{K} = 0$, i.e. $\boldsymbol{k}_1 = -\boldsymbol{k}_2$.

There are several physical properties exhibited by BCS superconductors that together can be used to identify them. There is an energy gap associated with the Cooper pairs, the energy saved by pair formation compared to the unpaired state, which can be probed using infra-red absorption. The peak in energy of the absorption will correspond to the energy gap. The BCS theory predicts that the gap at zero temperature $\Delta(0)$, corresponding to the energy required to break up a Cooper pair, is related to T_C by [19]

$$\frac{\Delta(0)}{k_B T_C} = 3.528. \qquad (1.2.1)$$

Furthermore, BCS theory also predicts the so-called 'isotope effect', in which the critical temperature is found to depend on the isotope mass of the superconducting material. The fact that phonon modes are affected by isotope mass, and virtual phonon

exchange is responsible for the superconductivity, makes it relatively straightforward to understand qualitatively why this is so.

Cuprate Superconductors

In 1986 Bednorz and Müller [20] made one of the most important discoveries in modern condensed matter physics when they found that La_2CuO_4 becomes superconducting when a certain amount of Ba^{2+} is substituted for La^{3+}. The unprecedentedly high critical temperature of the superconductivity was the most remarkable feature. This breakthrough quickly led to the discovery of other 'high-T_C' cuprate superconductors such as $YBa_2Cu_3O_{6+x}$ [8]. The superconductivity in these cuprate compounds was found to be inconsistent with the well established BCS theory, which correctly explained the properties of the non-cuprate superconductors known at that point in time [21]. For example the critical temperatures of the cuprates were much higher than those generally compatible with BCS theory. Also the energy gaps observed in the cuprates suggested a moderate strength phonon interaction within the BCS framework, which was inconsistent with the very strong interaction needed to explain the high values of T_C. A new theoretical approach was therefore required to explain the physics of the cuprate superconductors, and in order for this to be formulated a large body of experimental data was needed.

Putting together the evidence from a large number of experiments allowed the phase diagrams relating the critical temperature to doping to be mapped out for many superconductors, and it has become clear that they display many similarities. Figure 1.1 shows a generic phase diagram for a hole-doped superconductor.

Considering the phase diagram with increasing doping, starting with the undoped case, a number of different phenomena occur. At the lowest doping the material is a Mott insulator and the spins order antiferromagnetically [22]. As x is increased the Néel temperature decreases, eventually reaching zero. If x is increased beyond this critical point the material enters either what is known as the spin-glass phase, or the pseudogap phase, at lower and higher temperatures respectively. The pseudogap phase is one in which certain physical properties show behavior indicative of the existence of an energy gap. It seems that electrons are not totally forbidden from crossing the gap, however, and the symmetry of the gap has been shown to be that of *d*-wave electrons [23].

Further increases in the doping eventually lead to the superconducting phase[2]. Within

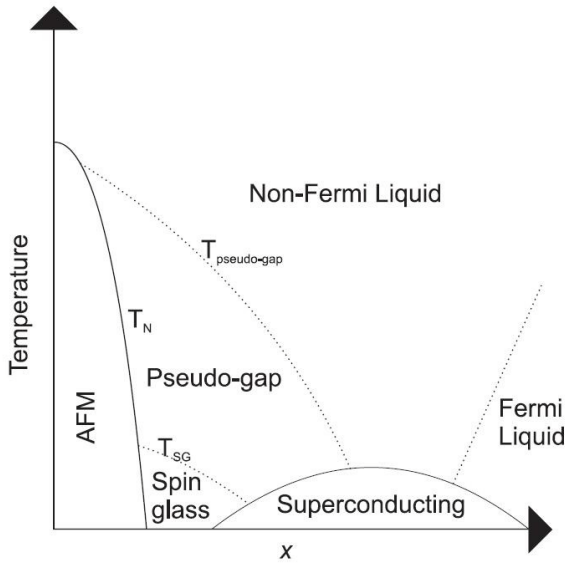

Figure 1.1 The generic phase diagram of a cuprate superconductor, showing the critical temperature T_C vs hole doping x [23].

[2] For doping lower than this lower critical level the material is said to be 'underdoped'. Likewise for doping higher than the upper critical level the material is said to be 'overdoped'.

this phase the critical temperature gradually increases with increasing x, until a maximum is reached whereupon T_C gradually reduces. A dip in T_C is also observed at $x = 1/8$, however it is too narrow to be shown in Fig. 1.1.

Eventually the doping x is increased enough that the superconducting transition temperature goes to zero. For higher doping than this critical level the material goes into the so-called Fermi liquid state. At low energies and temperatures we can consider a Fermi liquid state to consist of quasi-particles which separately contain the spin, charge and momentum of the fermions[3], and are weakly interacting. A final phase exists at higher temperatures for a wide range of doping, the so-called non-Fermi liquid phase. In this phase the physics of a Fermi liquid appear to break down and the properties of the system cannot be explained either by independent electrons, or quasiparticles. The precise nature of the non-Fermi liquid phase is not yet understood.

1.2.2 *The Colossal Magnetoresistance (CMR) Effect*

Introduction to Charge and Orbital Ordering

Charge Ordering Layered compounds isostructural to some cuprate superconductors, such as $La_{2-x}A_xMO_4$, with A = Sr, Ca, Ba . . . (hole dopants), and M = Ni, Co . . . [24, 25] have been found to exhibit charge order, i.e., the localization of the doped holes into periodic structures in the MO_2 planes. The spins of the M ions situated between the localized charges also tend to become ordered in periodic structures at the same time.

[3] i.e., one set of quasi-particles contain the spin, another set the charge, and another set the mo- mentum of the fermions

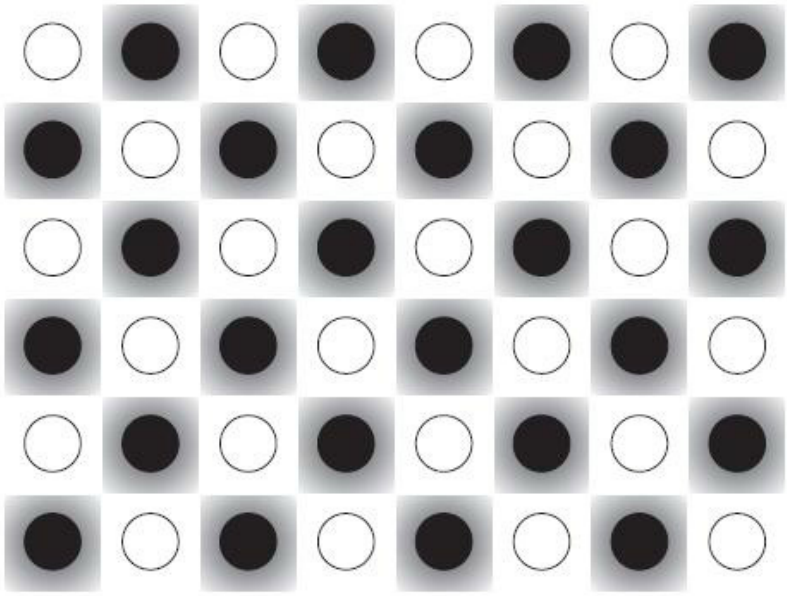

Figure 1.2 Schematic of a charge checkerboard for a half-doped $La_{2-x}A_xMO_4$ material, with circles representing ions on a square lattice and the shading representing localized charge.

The details of the charge order structures depend somewhat on *M*, but there are many features common to all of the materials. Two models commonly used to describe the charge order are the checkerboard model and the stripe model. In the former, a good example of which is found in $La_{1.5}Sr_{0.5}NiO_4$, the charge forms into the checkerboard-like structure as shown in Fig. 1.2 with alternate sites containing a hole, giving a periodicity of two lattice units. In $La_{5/3}Sr_{1/3}NiO_4$ the periodicity is three lattice units, and the charge structure is arranged into quasi-1D rivers (stripes) that run diagonally [26]. The presence of charge order can be detected directly using scanning tunneling microscopy (STM) [27], or indirectly using neutrons or x-rays to probe periodic structural distortions caused by Coulomb inter actions between the ordered charge and the ions in the lattice [28].

Orbital Ordering As has been mentioned above, the electron wavefunctions in solids tend not to be spherically symmetric and their orientation can therefore be affected by the symmetry of the local crystalline environment. In some materials, then, the energy can be lowered by the orbitals arranging themselves into a periodic structure - termed orbital ordering.

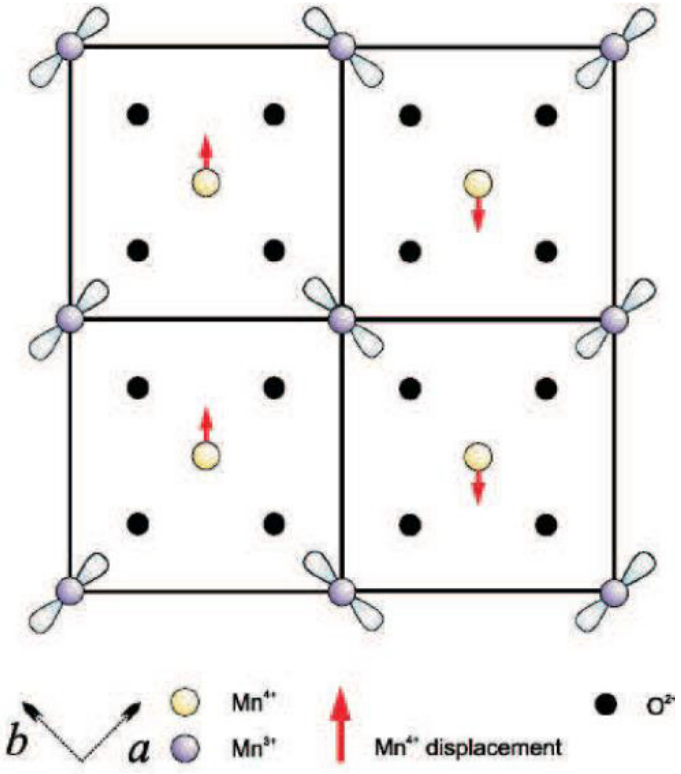

Figure 1.3 Schematic view of orbital order in $La_{0.5}Sr_{1.5}MnO_4$.

An example of a material in which orbital ordering occurs is $La_{0.5}Sr_{1.5}MnO_4$, which is, as with the charge ordered compounds discussed in section 1.2.2, isostructural to some cuprate superconductors [29]. In this material the $3d_{3z^2-r^2}$ orbitals of the e_g electrons on the Mn^{3+} sites form into zigzag chains in the *ab*-plane, shown schematically in Fig. 1.3. In general, the orientation of electron orbitals in a material has a strong effect on the

magnetic properties because they affect the strength of the inter-atomic exchange. These effects are described by the Goodenough-Kanamori-Anderson (GKA) rules [30].

Discovery of CMR Effect

Experimental work on manganites dramatically accelerated during the 1990s. This was caused by the observation of large magnetoresistance (MR) effects in these compounds. This property was noticed in the early studies (see Volger [31]), as already discussed, but its true magnitude was not appreciated, nor were its potential technological uses. The early relevant studies in this context include work on $Nd_{0.5}Pb_{0.5}MnO_3$ by Kusters *et al*. [32] (see Fig. 1.4).

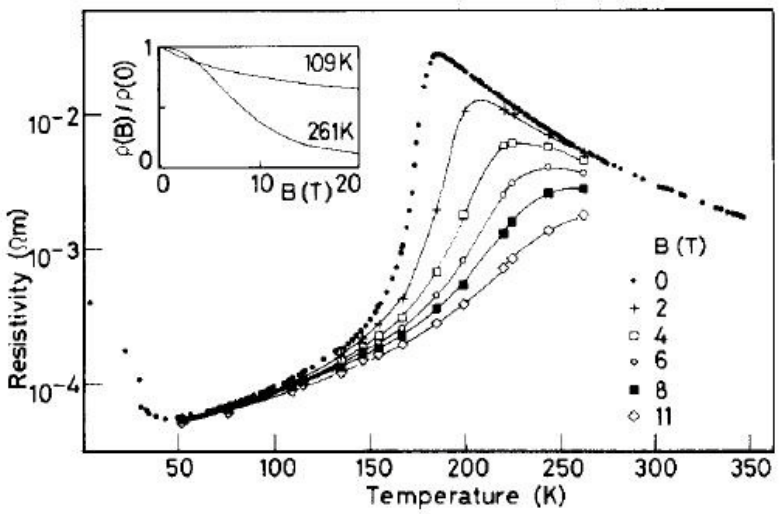

Figure 1.4 Resistivity of $Nd_{0.5}Pb_{0.5}MnO_3$ as a function of temperature and magnetic field. Inset illustrates the behavior of the magnetoresistance at two temperatures, above and below the ordering temperatures.

In that publication, a plot of resistivity vs. temperature at several magnetic fields revealed the large MR effect of these compounds. Work by von Helmolt *et al*. [33] on $La_{2/3}Ba_{1/3}MnO_x$ also revealed a large MR effect, this time at room temperature, using thin

films. The value of the MR was found to be larger than in 'giant' MR devices, which are artifially created arrangements of magnetic materials with large magnetoresistance. Similar conclusions were reached by Chahara *et al*. [34] using thin films of $La_{1-x}Ca_xMnO_3$ at $x = 0.25$. Ju *et al*. [35] also observed large MR thin films of $La_{1-x}Sr_xMnO_3$ near room temperature.

The explanation of CMR effect

After the early studies of manganites described above, Tokura *et al*. [36–38] proposed that the charge-ordering (CO) states observed by Jirák *et al*. [39] were very important for the explanation of the CMR effect. They presented results indicating an abrupt collapse of the CO state into a ferromagnetic (FM) state under the influence of a magnetic field. The competition between CO and FM is indeed a key component of the current theories of manganites aiming to explain the CMR phenomenon. It is clear from the experiments and the theory that the CO-FM transition should be first-order unless disordering effects smear it into a rapid but continuous transition. The huge CMR effect in some compounds at very low temperatures appears to be caused by the CO-FM first-order transition induced by magnetic fields. This physics is not contained at all in the early theoretical studies of manganites in the 1950s and 1960s, which were based on the so-called double-exchange effects and one-orbital models. Only in the late 1990s and early 2000s has the CO-FM competition been identified as the key ingredient of the CMR phenomenon.

1.2.3 *Quantum Phase Transition*

Another complex oxide, the single-layered $Ca_{2-x}Sr_xRuO_4$, is a quasi two-dimensional perovskite system, showing a rich array of interesting ground states [40, 41]. As shown in Fig. 1.5 [42], isovalent cation substitution of the smaller Ca^{2+} by the bigger Sr^{2+} ions

induces both structural distortion and an unusual variation of electronic and magnetic properties.

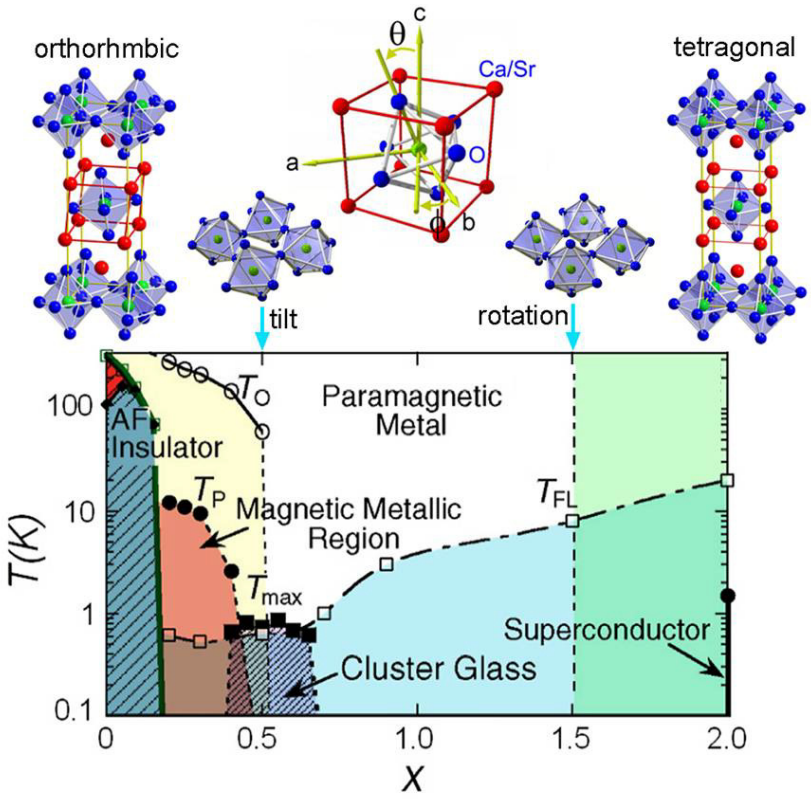

Figure 1.5 Phase diagram with structural evolution of $Ca_{2-x}Sr_xRuO_4$. T_O, T_P, and T_{max} are the orthorhombic structural transition temperature and the peak temperature of $\chi(T)$, and peak temperature of $M(T)$ curve with zero-field cooling, respectively. Both rotational (φ) and tilt (θ) distortion of RuO_6 octahedron are shown.

As is common in perovskites when the *A*-site cations with different ionic radii are substituted, Ca replacement for Sr gradually modulates the rotational and tilt distortion of the RuO_6 octahedra, starting with a tetragonal *I*4/*mmm* structure for Sr_2RuO_4, to an $I4_1/acd$ structure for $Ca_{1.5}Sr_{0.5}RuO_4$, and ending with an orthorhombic *S-Pbca* structure for Sr_2RuO_4 [43]. This in turn leads to an evolution of the ground state, from an unconventional '*p*-wave' superconducting state in Sr2RuO4 with possible spin-triplet

pairing [44], to a quantum critical point at $x = x_c \sim 0.5$ and to an antiferromagnetic Mott-insulating phase when $x < 0.2$ [40, 41]. All of these exciting phenomena strongly suggest an intriguing interplay between spin, lattice, and orbital degrees of freedom as well as the effect of reduced dimensionality [45].

1.3 Motivation of this Thesis

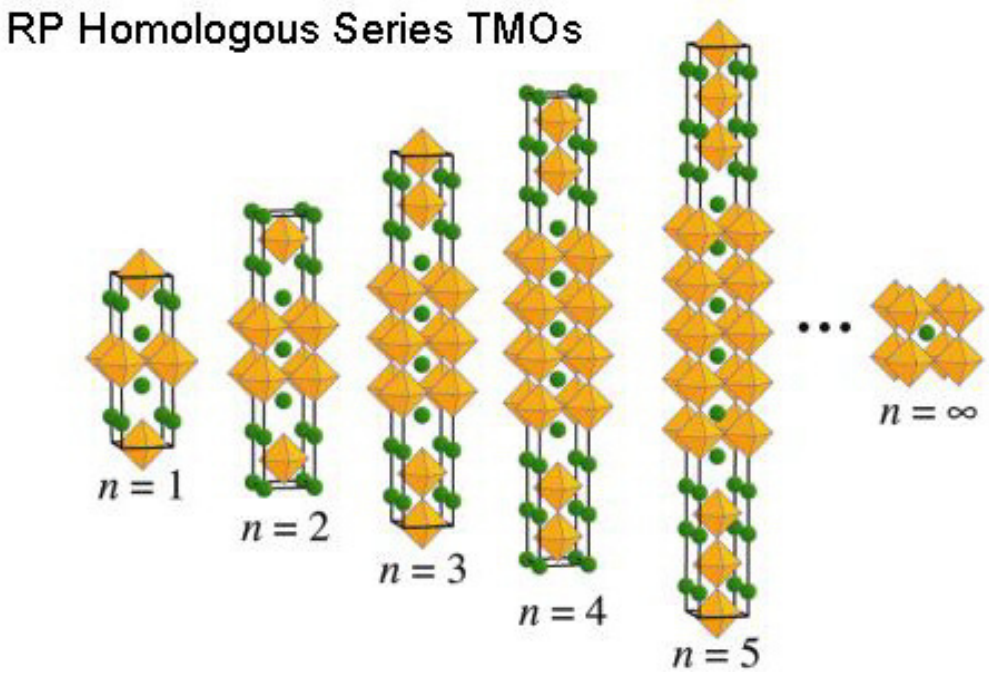

Figure 1.6 Schematic illustration of the perovskite structure of RP series: $A_{n+1}M_nO_{3n+1}$. The A cation ions are the dark spheres, and the M-O octahedra are the MO_6 complexes. The structural properties of the $n = 1$ and $n = 2$ phases are clearly low dimensional and are expected to lead to highly anisotropic physical properties.

The fascinating complex and collective phenomena introduced in the previous sections, which have been revealed in TMO compounds, present us profound and formidable challenges in condensed matter physics [1, 3]. Particularly, many exotic properties are intimately linked to the complexity of 'nature-designed' layered structures and associated with reduced dimensionality. This can be illustrated by considering the

Ruddlesden-Popper (RP) series, i.e., $A_{n+1}M_nO_{3n+1}$, as shown in Fig. 1.6. [46] A is normally a trivalent or divalent cation ion and M a transition metal ion. The structure is made up of n consecutive perovskite layers (AMO_3) alternating with rock salt layers so that their formula can be represented by $(AO)(AMO_3)_n$, where n represents the number of connected layers of vertex sharing MO_6 octahedra. Partial substitution of the A ions with other ions with different ionic size normally varies the bandwidth, while substitution with ions of different chemical valence, which creates multiple valences in the M ion sites, causes carrier doping thus changing the band filling.

Many TMOs are characterized by physical complexity resulting from the coexistence and competition between different kinds of order involving charge, orbital, lattice, and spin degrees of freedom. The relationship between these degrees of freedom is often synergistic and non-linear, thus creating many intriguing collective behaviors that rarely occur in simple materials like pure metals or semiconductors. The complexity of TMOs is directly responsible for their tunability. The balance between competing phases is very subtle and small changes in the composition can produce large changes in the physical properties.

In the past few decades, the cobaltates have attracted tremendous interests because of their complex phase diagram and intriguing magnetic and electronic properties. A wide variety of experimental results and theoretical investigations on these TMOs have convincingly demonstrated the intrinsic inhomogeneous electronic states.

Much work has been done on 3*d* TMOs because of the highly correlated electron related collective phenomena, such as high-temperature superconductivity in cuprates and colossal magnetoresistance in manganites. Although the Co element is two columns away

from either Mn or Cu in the periodic table, cobalt-based oxides are known to exhibit unique physical properties, originating from the rich electronic configurations and spin states. For instance, the rhombonhedrally distorted perovskite $LaCoO_3$ has a $3d^6$ electron configuration of Co^{3+} and because of the comparable crystal-field splitting and Hund's coupling energy, it undergoes a temperature-dependent spin-state transition between the high-spin ($S = 2$; $t_{2g}^4 e_g^2$) and low-spin ($S = 0$; t_{2g}^6) states [47-51]. Layered perovskite $La_{2-x}Sr_xCoO_4$ ($0.4 \leq x \leq 1.0$) shows drastic changes of the magnetic and electric properties, which suggest a high-spin state to intermediate-spin state transition of the Co^{3+} ions [52]. Most recently, possible stripe phases have been observed by neutron scattering in $La_{2-x}Sr_xCoO_4$ with $x > 0.3$ that exhibit incommensurate spin orderings [53, 54]. In the recent discovered superconductor, $Na_xCoO_2 \cdot yH_2O$ ($x \sim 0.35$, $y \sim 1.3$), Co ions were revealed lying on the two-dimensional triangular CoO_2 sheets. This compound has been confirmed as a magnetically frustrated system with low dimensionality [55]. In addition, $La_{2-x}Ba_xCuO_4$, which was the first high-T_C superconductor [20], has the similar chemical formula to $Ba_{2-x}Sr_xCoO_4$. With simple ion substitutions, single-layered ruthenates, $Ca_{2-x}Sr_xRuO_4$, provide a wide variety of novel phases because of the position of the Fermi level in multiple bands resulting from the hybridization of oxygen $2p$ and ruthenium $4d$ levels [10, 40, 41].

In the following several subsections, I will go through a few prototype compounds that motivated me doing this thesis work.

1.3.1 *$La_{2-x}Ba_xCuO_4$*

$La_{2-x}Ba_xCuO_4$ (hereafter referred to as LBCO) was the first high-T_C cuprate superconductor to be discovered [20], and very little time elapsed after this initial

discovery before the main features of the phase diagram as a function of doping were known. These follow the generic features described in section 1.2.1. Of particular interest is the very strong suppression of superconductivity near to $x = 1/8$. This suppression of T_C has been seen in all cuprates, however in certain materials, of which LBCO is one example, T_C decreases almost to zero. This contrasts with, for example, $La_{2-x}Sr_xCuO_4$, where the suppression of T_C is only a few percent [56, 57].

The crystal structure of LBCO is different from most cuprates, because on cooling to low temperatures ($T \leq 50$ K) it changes from orthorhombic to tetragonal [58], whereas most other cuprates tend to remain in an orthorhombic structural phase. Measurements of the resistivity [59] parallel to the CuO_2 planes show that in the normal state there is a sharp increase in resistivity on cooling to about 50 K and then a further more gradual increase in resistivity with decreasing temperature, indicating that the mobile charge carriers become more localized below 50 K. Such measurements do not, however, provide any information about the spatial distribution of these kinds of localized carriers (holes).

It would be natural to investigate whether the difference in the low temperature structure of LBCO compared to other cuprates is relevant to the strong suppression of superconductivity and the concomitant localization of the charge carriers. The most obvious way to do this would be to perform x-ray diffraction and neutron scattering measurements in order to probe the order parameters in the tetragonal state. Unfortunately the necessary large single crystals of LBCO have proved somewhat difficult to grow, and it has only been in recent years that such measurements have been possible.

Faced with this difficulty other materials were sought which displayed similar characteristics, and it was noticed quite quickly that substitution of a certain amount of Nd for $La_{2-x}Sr_xCuO_4$ stabilized a tetragonal phase at low temperatures [6]. It was found that the material $La_{2-x-y}Nd_ySr_xCuO_4$ (LNSCO) with $y = 0.4$ and $x = 1/8$ had many similarities with $x = 1/8$ LBCO, with the advantage that the crystals were easier to grow.

1.3.2 *$LaCoO_3$*

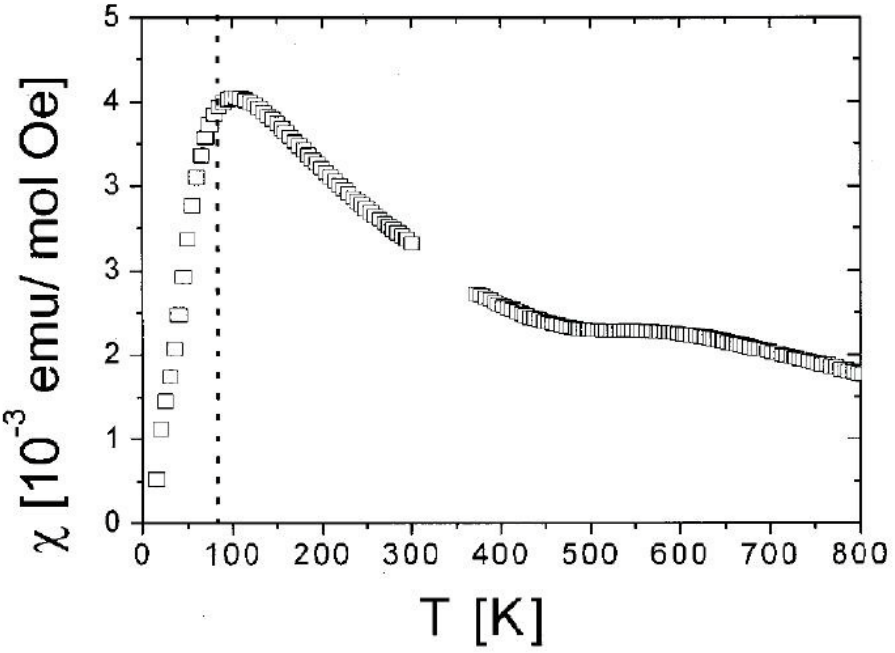

Figure 1.7 The magnetic susceptibility of $LaCoO_3$ as a function of temperature [47]. Van-Vleck and impurity contributions to the susceptibility have been subtracted from these data.

$LaCoO_3$ is a semiconductor that has been of interest for many years because of its peculiar magnetic properties. The ground state, measured at low temperatures, is non-magnetic. However, as the material is warmed, the magnetic susceptibility steadily increases, reaching a maximum at about 100 K. As the temperature is increased further,

the susceptibility gradually decreases following a Curie law type behavior. The behavior of the susceptibility then deviates from this above about 400 K, becoming slightly larger than expected from the Curie law alone. The magnetic susceptibility, as measured by English *et al*. [47, 60, 61] is shown in Fig. 1.7.

This behavior is somewhat surprising, because the Co^{3+} ions have the $3d^6$ configuration, for which Hund's rules predict a ground state with $S = 2$. It is therefore clear that this is a material in which the competition between the intra-atomic exchange and the crystal field determines the magnetic properties. The general principles to explain the unusual magnetism observed in $LaCoO_3$ are broadly agreed upon the Co^{3+} ions which have a ground state with $S = 0$, and there is an energy gap between this state and excited states that have $S = 0$. As the material is warmed the magnetic excited state(s) are thermally populated, so that increasing temperature leads to an increased number of magnetic ions. However there is a trade-off between the increase in susceptibility that results from this thermal population, and the thermally induced fluctuations of the ions in the magnetic state that act to reduce the susceptibility according to the Curie-Weiss law. It is this trade-off that results in the susceptibility rising to a maximum before decreasing again on warming.

The crystalline environment of the Co^{3+} ions is very close to being octahedral. An octahedral crystal field would split the $3d$ orbitals into t_{2g} and e_g states, with the former at a lower energy [62]. In the non-magnetic state the Co^{3+} is in the t^6 configuration, whereas in the magnetic state one or more electrons are excited into the e_g states.

The delicate balance of the various interactions in $LaCoO_3$ means that the nature of the magnetic excited state is not immediately obvious. A simple view is that there exists

competition between the crystal field and the *L*-*S* coupling (parameterized by Hund's rules), which would mean that the excited state has $S = 2$. Indeed this view prevailed for many years after the physical properties of $LaCoO_3$ were first measured. For example Raccah and Goodenough [63] were able to model successfully the behavior with temperature of the conductivity, magnetic susceptibility and structural parameters assuming a high-spin (HS, $S = 2$) model.

More recently, inelastic neutron scattering, which excited electrons directly from the low-spin (LS, $S = 0$), confirmed the existence of a HS or intermediate-spin (IS, $S = 1$) first excited state. Evidence for such a transition, from the LS to IS state at $T = 8$ K, was presented by Kobayashi *et al*. [64], who used unpolarized neutrons and therefore had to perform quite complicated corrections to their data in order to subtract the non-magnetic scattering from the signal. The energy gap between the LS and IS state determined by this method was found to give rise to a broad peak centered around 20 meV at the ferromagnetic wavevector $Q_{FM} = (1, 0, 0)$ in pseudo-cubic notation. Recently, however, measurements using polarized neutrons [65] have failed to confirm these results, indeed finding no magnetic signal at either ferromagnetic or antiferromagnetic wavevectors at low temperature. This has cast doubt on the background subtraction procedure used by Kobayashi *et al*., and it seems that a direct transition from the ground state is not observable, which would suggest either that the first excited state is high-spin, or that the LS-IS transition matrix element is too small to make the transition observable.

1.3.3 $La_{1-x}Sr_xCoO_3$

The materials with the general formula $La_{1-x}Sr_xCoO_3$ (LSCoO) are an interesting group of materials to study because they display many of the characteristics typical of

the colossal magnetoresistance (CMR) perovskites [66, 67], and also share some similarities with giant magnetoresistance (GMR) heterostructures [68]. The latter materials are artificial structures in which ferromagnetic metallic sections are placed in a matrix of non-magnetic material, and have been extremely important for the development of efficient hard disk drives. Similar so-called 'phase separation' of ferromagnetic and non-magnetic media, occurring naturally rather than being engineered, has been observed in CMR materials. An example of such het- erogeneity would be the formation of 'islands' of magnetically ordered ions surrounded by a region of the material that is non-magnetic. The most studied CMR perovskites to date have the general formula $La_{1-x}A_xMnO_3$, where A is a hole dopant such as Sr^{2+}, Ca^{2+}, Ba^{2+}, etc. The CMR effect is observed to be greatest near the critical temperature for the onset of bulk magnetic order [66].

Bulk measurements of the magnetic and transport properties of LSCoO show dramatic changes with doping [69, 70]. Susceptibility measurements, shown in Fig. 1.8, show that the $x = 0$ material is non-magnetic, but as doping is increased the size of the moment increases rapidly, with a transition into a true ferromagnetic state at $x = 0.18$. The Curie temperature at $x = 0.18$ is 150 K, and T_C increases with further increase in doping. These measurements have been interpreted as arising from the growth of ferromagnetic clusters, the number and size of which increase as doping is increased, until percolation to a bulk ferromagnetic state occurs at $x = 0.18$.

The behavior of the resistivity with temperature, shown in Fig. 1.9, is also found to vary as a function of doping [69, 70]. At $x = 0$ the material is a semiconductor, but the resistivity steadily decreases as holes are doped into the material. These

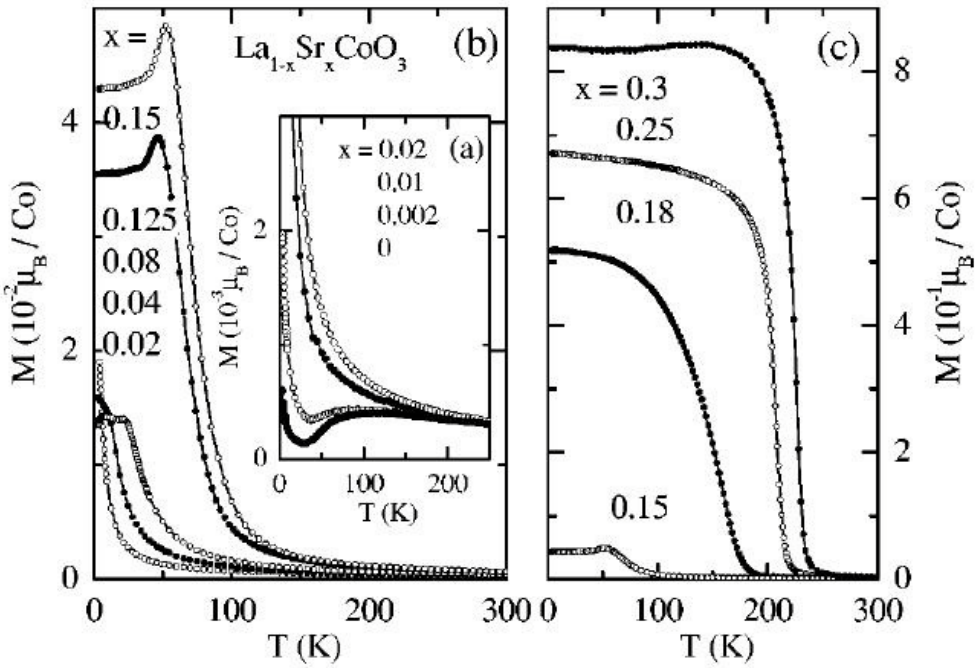

Figure 1.8 Magnetic susceptibility of $La_{1-x}Sr_xCoO_3$ as a function of temperature and doping x.

resistivity steadily decreases as holes are doped into the material. These measurements show that as the material tends towards ferromagnetism it also becomes increasingly metallic, i.e., the magnetism resides on itinerant rather than localized electrons. This aspect of LSCoO bears many similarities to the behavior of the CMR manganites.

Measurements of the magnetoresistance of LSCoO as a function of doping [71] show that for higher doping, when the material is in a ferromagnetic metallic phase, the magnetoresistance is just a few percent. However when the doping reaches the critical level of $x = 0.18$ the MR becomes around 30%, and as the doping is decreased further the MR increases such that for $x = 0.09$ the resistivity drops by as much as 90% at low temperatures.

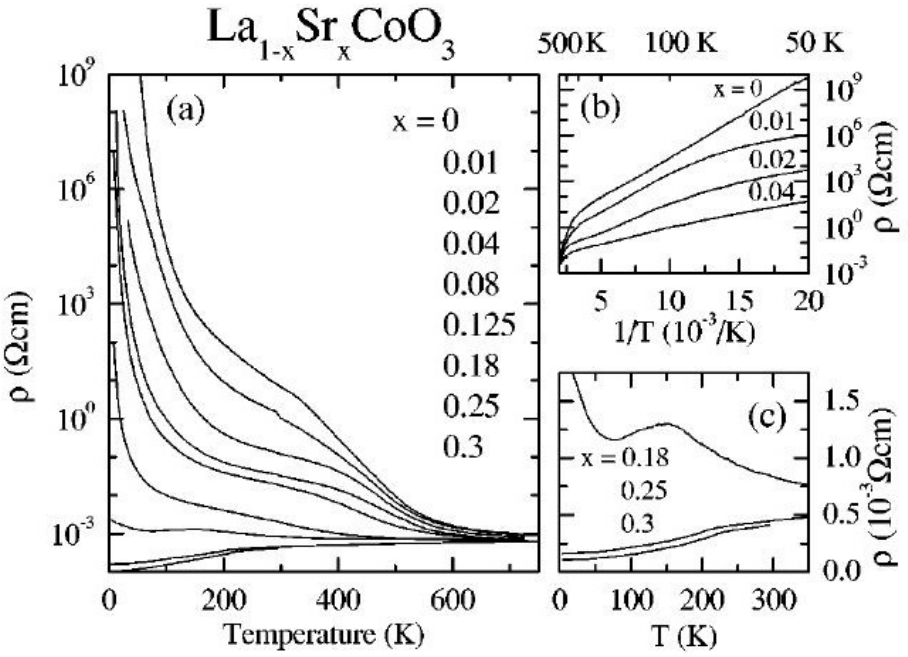

Figure 1.9 Resistivity of $La_{1-x}Sr_xCoO_3$ as a function of temperature and doping x.

In the region of doping $0 < x < 0.18$, the material displays behavior which is in some respects like that of a spin glass. In a true spin glass, dilute spins in a solid are randomly distributed. However, there exist interactions between spins that act to freeze them into a metastable state with short range magnetic order [62].

1.3.4 *$Ba_{2-x}Sr_xCoO_4$ in this Thesis*

Much less studied are the cobaltates with Co in a tetrahedral environment. In polycrystalline Ba_2CoO_4, it has been reported that the Co ions are in tetrahedral sites [72–74], but its single crystal preparation and physical properties are essentially unknown. On the other hand, Matsuno *et al*. and Wang *et al*. have reported that Sr_2CoO_4 is a ferromagnetic (FM) metal in forms of thin films [75] and bulk polycrystalline powder [76, 77], where Co is in octahedral environment. The abrupt

change in crystal structure stimulates us to systematically investigate the structural and possible magnetic transitions, as well as their correlations in this isovalent doping system.

1.4 Scope of this Thesis

The present Ph.D thesis is organized as follows: in Chapter 2 experimental techniques, including sample synthesis methods, physical property characterization techniques, the theory of neutron production and scattering, and lattice and magnetic structure refinements by using neutron scattering, are presented.

In Chapter 3, we briefly comment on the preparation conditions for the studied polycrystalline and single crystalline samples, which were synthesized at the Correlated Electron Materials Group at Oak Ridge National Laboratory (ORNL). We present the successful results of our own attempts to grow single crystals of $Ba_{2-x}Sr_xCoO_4$. Furthermore, the basic ideas of neutron scattering techniques and the experimental setup of the utilized neutron diffractometers are presented.

In Chapter 4 our experimental results on the evolution of the structural properties with Sr substitution in $Ba_{2-x}Sr_xCoO_4$ as observed by high-resolution x-ray diffraction are presented and discussed in detail.

In Chapter 5 the electronic and magnetic properties of $Ba_{2-x}Sr_xCoO_4$ are also discussed with the help of SQUID and the high-resolution neutron powder diffraction at NIST.

In Chapter 6 the magnetic structure and excitations of Ba_2CoO_4 are presented and discussed. Finally, the phase diagram of $Ba_{2-x}Sr_xCoO_4$ is summarized and an outlook to future research issues is given in Chapter 7.

CHAPTER 2

EXPERIMENTAL TECHNIQUES

This chapter gives a basic introduction to the experimental methods that were used for the measurements presented in the rest of this thesis. Section 2.1 presents the fundamentals of sample synthesis methods including conventional solid state chemical reactions and the floating-zone method. Section 2.2 gives some background to the overview of the physical property characterization techniques, such as the SQUID magnetometer and the Quantum Design PPMS heat capacity measurement system. Section 2.3 outlines some details specific to the theory of neutron production and scattering, as well as descriptions of neutron spectrometers. Finally section 2.4 provides the basics of lattice and magnetic structure refinements by using neutron scattering.

2.1 Synthesis Methods

2.1.1 *Solid-State Chemical Reaction*

Since the specimen of my research is a kind of oxide, the very first step of preparing samples is the conventional solid-state chemical reaction. This method is also known as a dry media reaction or solventless reaction, which is a chemical reaction system in the absence of a solvent [78].

The drive for the development of solid-state reactions in chemistry is

- Economics (save money on solvents).
- Ease of purification (not required to remove a solvent post-synthesis).
- High reaction rate (due to the high concentration of reactants).
- Environmentally friendly (solvent is not required).

Drawbacks to overcome:

- Difficulty in mixing reactants into a homogeneous system.
- High viscosity in reactant system.

2.1.2 *Floating-zone Single Crystal Growth*

Floating-zone (FZ) technique is widely used for obtaining high quality single crystals, especially oxides. The FZ process, which is also called zone melting or zone refining, is a group of similar methods of purifying crystals, in which a narrow region of a crystal is molten, and this molten zone is moved along the crystal (in practice, the crystal is pulled through the heater). The molten region melts impure solid at its forward edge and leaves a wake of purer material solidified behind it as it moves through the ingot. The impurities concentrate in the melt, and are moved to one end of the ingot. This technique was developed by William Gardner Pfann in the Bell Labs as a method to prepare high purity materials for manufacturing transistors. Its early use was on germanium for this purpose, but it can be extended to virtually any solute-solvent system having an appreciable concentration difference between solid and liquid phases at equilibrium.

The basic idea in FZ crystal growth is to move a liquid zone through the material. If properly seeded, a single crystal may result, as shown in Figure 2.1. The principle of this method is that since the segregation coefficient k (the ratio of an impurity in the solid phase to that in the liquid phase) is usually less than one. Therefore, at the solid/liquid boundary, the impurity atoms will diffuse to the liquid region. Thus, by passing a crystal boule through a thin section of furnace very slowly, such that only a small region of the boule is molten at any time, the impurities will be segregated at the end of the crystal. Because of the lack of impurities in the leftover regions which solidify, the boule can grow as a perfect single crystal if a seed crystal is placed at the base to initiate a chosen direction of crystal growth. When high purity is required, such as in semiconductor industry, the impure end of the boule is cut off, and the refining is repeated.

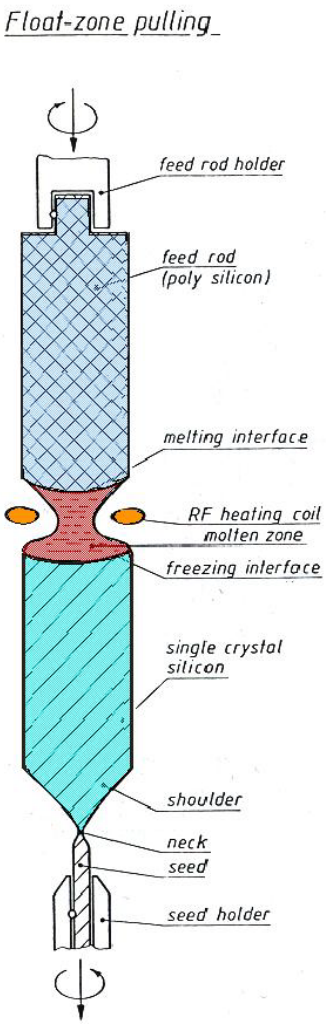

Figure 2.1 Illustration of floating-zone single crystal growth technique.

The problem of FZ crystal growth is also clear, however, if one looks at Fig. 2.1: How do we keep the liquid Si from just collapsing? If it would only be held in place by surface tension, the maximum diameter of crystals possible in this way would be about 20 mm - not very useful. There are, fortunately, other stabilizing mechanisms, and drawing the liquid zone through a 'hole' - as indicated - also helps. Still, for large diameter crystals the difficulties grow rapidly and FZ crystal growth is rarely (if at all) used for diameters larger than 150 mm.

2.2 Physical Property Measurement Techniques

2.2.1 *Magnetization Measurements Using a SQUID*

The magnetization measurements presented in this thesis were all taken using a Quantum Design MPMS XL magnetometer. This magnetometer works using a superconducting quantum interference device (SQUID) coil [79]. The sample environment is a Helium flow cryostat, which can be cooled to a base temperature of 1.6 K. A magnetic field is applied in the vertical direction by a superconducting magnet, which has a practical range of about ± 5 T. All of the measurements are computer controlled using software that was designed specifically for this magnetometer by Quantum Design Inc.

For a measurement of the magnetic susceptibility the sample is typically mounted inside a plastic straw with a diameter of ~ 5 mm, the diamagnetic moment of which is very small. The sample can be secured inside this straw in a variety of ways. The two that were most often used for the work presented here were, 1) to place the sample inside a plastic capsule, packed tight with cotton wool and sealed with kapton tape, itself inserted into the plastic straw; 2) to wedge the sample between two folded over straws inserted into the plastic straw. The method chosen depended on the particular geometry of the sample and the crystallographic direction in which the field needed to be applied. The principle of operation of the apparatus is shown schematically in Fig. 2.2. The plastic straw containing the sample is translated vertically between three superconducting coils, in which a current proportional to the sample magnetization is induced. These coils lead to two coupled inductors, which then leads to another pair of inductors, between which a SQUID is placed. Thus small changes in the sample magnetization are measured as small

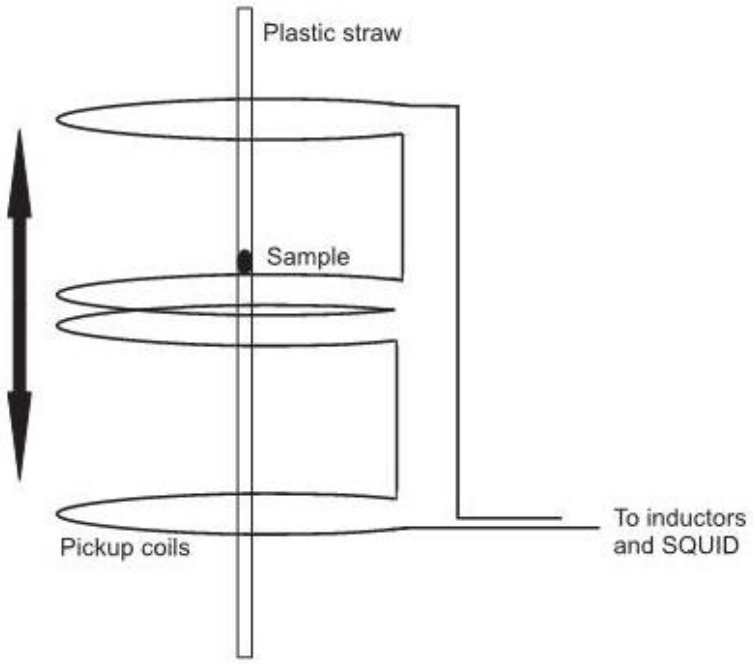

Figure 2.2 The pickup coils of the SQUID magnetometer.

current changes, which are converted into small changes in magnetic field near the SQUID.

2.2.2 *Heat Capacity Measurements Using a PPMS*

The heat capacity measurements presented in this thesis were all performed using a Quantum Design Physical Properties Measurement System (PPMS) [80]. The PPMS can measure a variety of physical properties (resistivity, AC susceptibility, etc.), however, the heat capacity option is the only one that was utilized for the work presented in this thesis.

A schematic of the sample mount, known as the puck, is shown in Fig. 2.3. The platform is connected to the support frame of the puck, which acts as a heat sink, by thin wires, which also serve as electrical contacts for the heater and resistance thermometer. A good thermal contact between the bottom surface of the sample and the

platform is ensured by using Apiezon grease. The whole apparatus is controlled by computer, using Bespoke software.

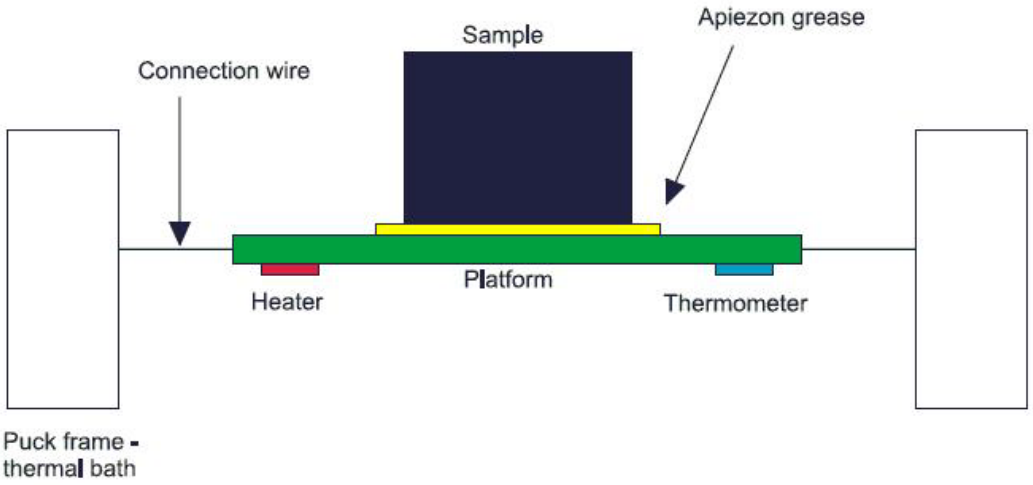

Figure 2.3 Side view of the sample mount for heat capacity measurements using the PPMS.

In order to make a measurement the heater supplies a fixed amount of power $P(t)$ for a length of time t, and is then turned off. The temperature of the sample/platform/grease assembly rises as the heat is applied, whereas the thermal bath remains at constant temperature, and then cools through radiation and conduction through the wires when the heater is turned off. The software monitors the temperature throughout this, and the heat transfer is modeled by the differential equation

$$C_{\text{total}}\frac{dT}{dt} = -K_W\{T(t) - T_b\} + P(t), \qquad (2.2.1)$$

where C_{total} is the heat capacity of the sample and platform together, K_W is the thermal conductivity of the wires, and T_b is the fixed temperature of the thermal bath. By solving this differential equation the heat capacity is calculated from the exponential decay constant of the sample temperature. In order to find the heat capacity of the

sample, the heat capacity of the puck and platform must be subtracted, so the behavior of this quantity vs. temperature is calibrated before the experiment takes place.

If the thermal contact between the platform and sample is not very good a more complicated model is used which accounts for the behavior of the two separately,

$$C_{\text{platform}}\frac{dT}{dt} = P(t) - K_W\{T_p(t) - T_b\} + K_g\{T_s(t) - T_p(t)\}, \quad (2.2.1)$$

$$C_{\text{sample}}\frac{dT_s}{dt} = -K_g\{T_s(t) - T_p(t)\}, \quad (2.2.1)$$

where K_g is the thermal conductivity of the grease, and the temperature of the sample and platform is given by T_s and T_p respectively.

2.3 Neutron Scattering

The neutron scattering technique is one of the most invaluable and versatile microscopic probes in the study of condensed matter. This is because of several unique fundamental properties of neutrons. First, the relatively large mass of a neutron (1.674928×10^{-24}g) allows thermal neutrons of energy range 5 to 100 meV to have a wavelength of 1 to 3 Å, which is comparable to interatomic distance in solids. The energy of thermal neutrons is of the same order as of the fundamental excitations in solids. Also, because a neutron carries no charge, it can penetrate deeply into the bulk and come close to the nuclei. Moreover, it has a magnetic moment. This means that neutrons interact with the unpaired electrons in magnetic ions. This property is perfect for the investigation of magnetic structure. Elastic scattering from this interaction gives information on the arrangement of electron spins and the density distribution of unpaired electrons. Inelastic magnetic scattering gives the energy and wave vector dependencies of magnetic excitations.

2.3.1 *Neutron Sources*

There are two methods currently employed to generate neutrons for use in scattering experiments, each with its pros and cons. The first method is nuclear fission, occurring in a traditional nuclear reactor with uranium as the fuel.

$$^{235}\mathrm{U} + \mathrm{n} \rightarrow 2.5\mathrm{n} + 200\mathrm{MeV} + \mathrm{nuclei}. \qquad (2.3.1)$$

A reactor at a neutron scattering facility would be designed to produce an excess of neutrons beyond that required maintaining the chain reaction, and it is these excess neutrons that are used for scattering. Before reaching the scattering instruments the neutrons pass through a moderator that modifies their energy spectrum. The precise choice of moderator material and temperature determines the resulting spectrum. After this the neutrons pass through wave guides to the instruments. In order to avoid 'fast' (i.e., high energy) neutrons irradiating the sample the waveguides are actually oriented tangentially to the reactor core. Neutrons which undergo several scattering processes in the moderator tend to be more likely to enter such waveguides than unscattered fast neutrons, which are radiated radially from the reactor core. The main advantage of a reactor source is that it produces a high flux of neutrons at a steady rate.

The other method of generating neutrons for scattering is with a spallation source. Accelerated protons strike a heavy metal target, and the impact of the proton beam triggers a nuclear reaction. The spallation process is the excitation and neutron emission of the target until it achieves a stable nuclear state. The spectrum of the neutrons is, as with a reactor source, modified by moderators. Such a source typically produces a much lower flux of neutrons than a reactor. However, if the proton beam is pulsed, the so-called 'time-of-flight' instruments can be used rather inefficiently at a reactor source.

2.3.2 *Neutron Scattering Instruments*

There are many types of neutron scattering instruments. For inelastic scattering the two main types of instrument used are the time-of-flight (ToF) chopper spectrometer and the triple-axis spectrometer (TAS). The former are used at pulsed spallation neutron sources, as well as at continuous spallation or reactor sources, whereas the latter are most often used at reactor sources. For the research presented in this thesis all of the neutron scattering measurements were performed on triple-axis spectrometers, so only the details of these will be presented.

Triple-axis Spectrometer

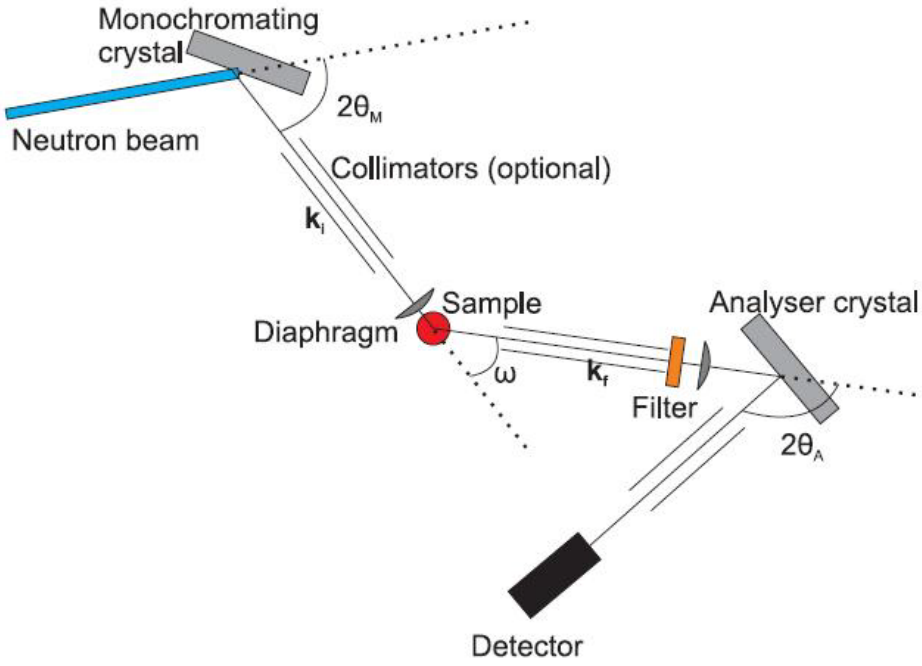

Figure 2.4 A schematic of a conventional triple-axis spectrometer.

The individual components of a TAS are as follows. The monochromator, typically made from pyrolytic graphite (PG), silicon or Heusler crystals, turns a polychromatic

beam of neutrons into a monochromatic one by Bragg reflection (usually the 002 reflection for PG). Only neutrons of a given wavelength (energy) fulfill the Bragg condition. Collimators can be used to ensure that the beam does not diverge too much, and they typically take the form of parallel plates which are coated with a neutron-absorbing material such as boron or gadolinium. Despite this the width of the neutron beam is likely to be larger than the width of the sample, so in order to improve the signal-to-noise ratio diaphragms are placed before and after the sample. Diaphragms are also placed in front of the analyzer and detector in order to allow full illumination whilst reducing spurious scatter entering the detector, thus further improving the signal-to-noise ratio. The sample may be mounted in a standard cryostat, in a dilution refrigerator, or in a cryomagnet depending on the sample environment needed. The analyzer crystals work in much the same way as the monochromator, e.g. one might use the (002) reflection from PG, or the (111) reflection from Si, depending on the choice of final neutron wavevector k_f.

More often than not the spectrometer is set up to use a fixed final wavevector k_f, meaning that in order to do inelastic scattering measurements it is only the magnitude of the incident wavevector that is varied. There are several reasons why this setup is chosen. One is that it offers a larger dynamic range that is available with fixed incident wavevector, in that a greater energy range and wavevector transfer is accessible within the geometric constraints of the spectrometer. The incident beam monitor efficiency is inversely proportional to k_i (discussed later), so the neutron count rate normalized to the number of monitor counts is directly proportional to the response function $S(Q, \omega)$ (defined in section 2.3.3). Moreover, by fixing the final wavevector it allows the use of a

filter, the purpose of which is to remove so-called '$\lambda/2$, $\lambda/3$'… noise, i.e., neutrons whose energy is such that their wavelength is an integer fraction of the desired wavelength so they also fulfill the Bragg condition at the analyzer. This noise would result in spurious detector counts if filters were not used. The filters may be made from a variety of materials, dependent on the desired scattered wavevector. Typical choices might be cooled Beryllium for $k_i < 1.55$ Å^{-1} or pyrolytic graphite for $k_i = 2.66$ Å^{-1} or 4.1 Å^{-1}. These final wavevectors are chosen because they are values where the transmission is close to unity, but the transmission of the second, third and higher harmonics is close to zero.

For all of the work presented in this thesis, thermal energy neutrons ($E_{\text{incident}} < 50$ meV) were used, for which the filters one uses are based on Bragg scattering. For any given material there is a maximum wavelength (minimum energy) for which Bragg scattering can occur, which is given by twice the smallest lattice constant. For wavelengths shorter (energies higher) than this there is a steep decrease in the transmission. For example in a cooled Be filter[4] this change in transmission is rather sharp and occurs at about 5.2 meV. In a PG filter, one can choose a neutron wavelength where the transmission of the beam is very high, and in addition the $\lambda/2$ and $\lambda/3$ neutrons are at wavelengths that are strongly Bragg scattered by the PG crystal[5], and hence have a very low probability of transmission through the filter.

[4] The Be is cooled so that the population of phonons is very small, which means that the probability of phonon creation is very small, so neutrons with energies higher than 5.2 meV are less likely to lose energy through phonon scattering processes and pass through the filter.

[5] Note that the PG crystal has to be correctly oriented with respect to the beam scattered by the sample for this to work.

One of the main advantages of neutrons is that they interact rather weakly with matter, and that their interaction with magnetic moments is not immeasurably weak. This does, however, present a problem when it comes to detecting scattered neutrons. Neutrons are not charged so they cannot be detected using radiation detectors which rely on direct ionization. Instead the neutrons need to cause some other atom to emit charged particles which will ionize material in the detector and therefore be electronically detectable. The standard way of doing this is to use a chamber filled with ^{3}He gas, which then undergoes the following reaction:

$$\mathrm{n} + {}^3\mathrm{He} \rightarrow \mathrm{p} + {}^3\mathrm{H} + 0.77\ \mathrm{MeV}, \tag{2.3.2}$$

so that the charged decay products ionize the gas and give rise to a signal proportional to 0.77 MeV, which can be distinguished from signals at different energies arising from gamma rays entering the detector, for example. The ^{3}He nucleus eventually decays to form another ^{3}H nucleus and an electron, so the supply of helium in the detector does not need to be replenished.

It is important to know the flux of neutrons incident on the sample, especially given that this will vary depending on the value of the incident energy. The incident flux is measured using a monitor, which is simply a rather incident neutron detector. The monitor's efficiency is inversely proportional to the incident neutron wavevector, k_i, so that when detector counts are normalized to the monitor count rate and the final wavevector, k_f, is fixed, no correction for the k_f / k_i term in equation 2.3.37 is required. There are two main types of neutron monitors. The most common ones work on the same principle as the ^{3}H detector, but with a much lower gas pressure, which dramatically reduces the efficiency. Another kind of monitor is based on ^{235}U-doped

sol-gel thin films. A small number of ^{235}U nuclei undergo fission when neutrons pass through the film, and the charged decay products are detected using scintillation detectors.

Polarized Neutron Scattering Instrument Components

A variation on the basic TAS is the polarized neutron TAS, which works on the same principles as the basic TAS but has a few modifications. The basic idea behind these is to produce an incident beam of neutrons whose spins all point in the same direction. This reduces the flux incident on the sample, however by analyzing the change in polarization state of the neutrons after scattering it is possible to measure scattering which is solely magnetic in origin.

The first modification is to include a polarizing monochromator. An example of such a monochromator would be an array of large single crystals of Heusler (Cu_2MnAl) alloy, arranged so that neutrons scatter off the (111) Bragg planes. The analyzer would be made from the same material and works the same way. A magnetic field is applied parallel to the surface of the monochromator/analyzer and the spins in the crystal align parallel to this. Because Heusler is a centrosymmetric crystal (i.e., the values for both the nuclear and magnetic structure factors are real) and the nuclear and magnetic structure factors are similar in value, the two kinds of scattering can either constructively or destructively interfere, depending on the orientation of the applied field, resulting in very good (but not perfect) polarization. The precise details of this will be discussed later.

The next modification is the presence of guide fields around the neutron beam between the monochromator and the sample, and the sample and the analyzer. These are

basically shielded pipes inside which there is a uniform field of a few mT which serves to maintain the polarization state of the neutron beam. If the guide field was not there then electromagnetic noise would, over the course of the neutrons' path, destroy the polarization state.

The final modification is the insertion of 'flippers' upstream, or more usually downstream, of the sample. A flipper is a device which flips the neutron spin state from one eigenvalue to another, i.e., from spin up to spin down. The flippers often used in a thermal neutron TAS are radio-frequency (RF) coil flippers. In an RF flipper a constant magnitude radio frequency magnetic field is applied parallel to the neutron beam while a static field applied perpendicular to the neutron beam varies in magnitude along the beam. For all neutron energies there will be some point in the flipper such that their Larmor frequency is equal to the radio frequency of the coil, thus resonance will occur and there will be a transition between the Zeeman split up and down states, i.e., a spin flip.

A spin-flip magnetic scattering event would work as follows: the monochromator polarizes the beam so that the spins are up, then the spins are flipped in the sample by interaction with a spin-1/2 magnetic moment/excitation (parallel to the neutron spin) so that the neutrons are now spin down. The flipper then changes the spin state of the scattered beam so that the magnetically scattered neutrons are spin up again. The analyzer is then set to Bragg-reflect only spin up, so almost all of the non-magnetically scattered neutrons are not reflected into the detector, while the scattering from magnetic moments/excitations makes up the vast majority of the neutrons to be arriving at the detector.

2.3.3 *Neutron Scattering Cross Sections*

The derivation of the following results can be found in more detail in, for example, the book by Squires [81].

When neutrons are scattered, the number of scattered neutrons that enter a given solid angle at a known energy and momentum is measured. The laws of momentum and energy conservation that govern all scattering and diffraction experiments are:

$$\boldsymbol{Q} = \boldsymbol{k}_f - \boldsymbol{k}_i, \tag{2.3.3}$$

$$|\boldsymbol{Q}| = \boldsymbol{k}_f^2 + \boldsymbol{k}_i^2 - 2\boldsymbol{k}_i\boldsymbol{k}_f \cos\theta_s, \tag{2.3.4}$$

$$\hbar\omega = E_i - E_f = \frac{\hbar^2}{2m_n}\left(\boldsymbol{k}_f^2 - \boldsymbol{k}_i^2\right). \tag{2.3.5}$$

In these equations, the wave vector magnitude $k = 2\pi/\lambda$, where λ is the wave- length of the neutron beam, m_n is the mass of neutron, and the momentum transferred to the crystal is $\hbar\boldsymbol{Q}$. The subscripts *i* and *f* refer to the beam incident on the sample and the diffracted (final) beam.

Figure 2.5 shows a Ewald circle in two dimensions. In this diagram, $\boldsymbol{k}_i$ is the direction of the incident beam relative to the crystal and $\boldsymbol{k}_f$ is the direction of the diffracted beam. If a circle with radius $\boldsymbol{k}$ passes through two points on the circle, one of which is the origin of reciprocal space, the condition for Bragg scattering from the crystal is satisfied. We then have:

$$\boldsymbol{Q} = \boldsymbol{G} = \boldsymbol{k}_f - \boldsymbol{k}_i, \tag{2.3.6}$$

where $\boldsymbol{G}$ is a reciprocal-lattice vector. By Bragg's law $\lambda = 2d\sin\theta$, we know

$$|\boldsymbol{Q}| = |\boldsymbol{G}| = 2|\boldsymbol{k}_i|\sin\theta. \tag{2.3.7}$$

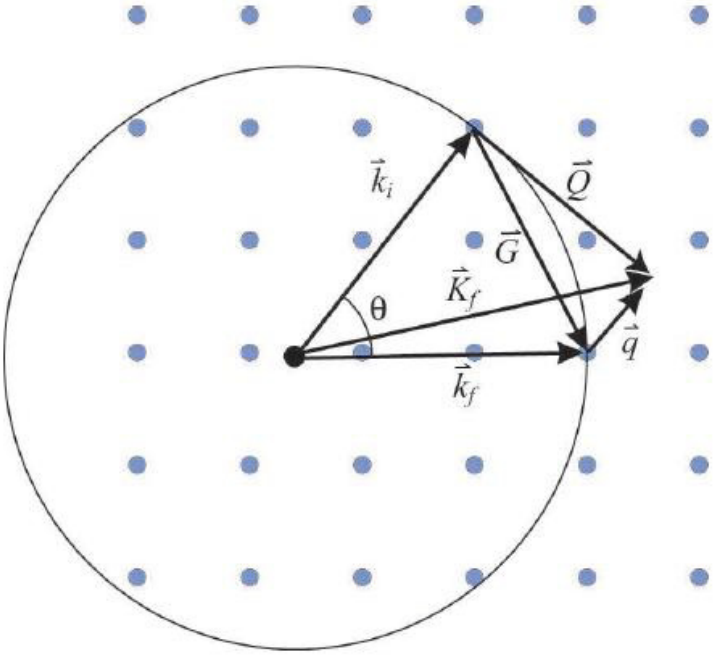

Figure 2.5 Two dimensional representation of reciprocal space showing the Ewald circle and the vector representation for elastic and inelastic scattering**.**

In a diffraction experiment, the magnitude of $\boldsymbol{Q}$ is controlled by adjusting the angle 2θ between $\boldsymbol{k}_f$ and $\boldsymbol{k}_i$. The orientation of $\boldsymbol{Q}$ within the reciprocal lattice is set by rotating the sample. Thus, any point in reciprocal space can be measured by an appropriate choice of $\boldsymbol{k}_i$, 2θ and the orientation φ of the sample relative to $\boldsymbol{k}_i$.

For inelastic neutron scattering, $|\boldsymbol{k}_i| \neq |\boldsymbol{k}_f|$ since a difference is needed for neutrons to gain or lose energy from the sample. For a single crystal sample, energies depend on the relative momentum defined within a Brillouin zone. It is therefore convenient to reference the momentum transfer to the nearest reciprocal lattice vector, i.e.,

$$\boldsymbol{Q} = \boldsymbol{G} + \boldsymbol{q}. \tag{2.3.8}$$

During the experiment energy transfer is varied while $\boldsymbol{Q}$ is held constant. In neutron scattering, we measure the number of neutron scattered per second into a given solid

angle $d\omega_f$, in the direction of the wave vector $\boldsymbol{k}_i$ with a final energy between E_f and $E_f + dE_f$. This is given by the partial differential cross section, $d^2\sigma / d\omega_f\, dE_f$. It is expressed as a sum of coherent and incoherent parts. The coherent scattering depends on the correlation between the positions of the same nucleus at different times, and on the correlation between the positions of different nuclei at different times. It therefore gives interference effects and contains information about the cooperative effects among different atoms, such as elastic Bragg scattering or inelastic scattering by phonons or magnons. While the incoherent scattering depends only on the correlation between the positions of the same nucleus at different times and does not give interference effects. It is proportional to the time correlation of an atom with itself and provides information about individual particle motion.

The partial differential cross section due to magnetic interaction V_m for unpolarized neutrons is given by

$$\frac{d^2\sigma}{d\Omega_f dE_f} = \frac{\boldsymbol{k}_f}{\boldsymbol{k}_i}\left(\frac{m_n}{2\pi\hbar^2}\right)^2 \left|\langle \boldsymbol{k}_f\sigma_f | V_m | \boldsymbol{k}_i\sigma_i\rangle\right|^2 \delta\left(\hbar\omega + E_i + E_f\right). \tag{2.3.9}$$

The interaction between the neutron and an unpaired electron is written as

$$V_m(\boldsymbol{r}) = -\boldsymbol{\mu}_n \cdot \boldsymbol{B}(\boldsymbol{r}). \tag{2.3.10}$$

In this equation $\boldsymbol{\mu}_n$ is the magnetic dipole moment of the neutron and $\boldsymbol{B}(\boldsymbol{r})$ is the magnetic field due to the magnetic dipole moment of an unpaired electron. The magnetic field due to the magnetic dipole moment of an electron is

$$\boldsymbol{B}(\boldsymbol{r}) = \nabla \times \boldsymbol{A} = \nabla \times \frac{\boldsymbol{\mu}_e \times \boldsymbol{r}}{r^2}, \tag{2.3.11}$$

where $\boldsymbol{\mu}_e$ is the magnetic dipole moment of an electron. By using these expressions, the partial differential cross section of localized spins can be expressed as

$$\frac{d^2\sigma}{d\Omega_f dE_f} = \frac{\boldsymbol{k}_f}{\boldsymbol{k}_i}\left(\frac{m_n}{2\pi\hbar^2}\right)p^2 f^2(\boldsymbol{Q})e^{-2W}\sum_{\alpha,\beta}\left(\delta_{\alpha\beta} - \boldsymbol{Q}_\alpha \boldsymbol{Q}_\beta\right)S^{\alpha\beta}(\boldsymbol{Q},\omega), \quad (2.3.12)$$

where

$$p = \frac{\gamma e^2}{2m_e c^2}, \quad (2.3.13)$$

and $\alpha, \beta = x, y, z$, and f2(Q) is the magnetic form factor, which is the Fourier transform of the spin density.

The scattering function $S^{\alpha\beta}(\boldsymbol{Q}, \omega)$ is defined as

$$S^{\alpha\beta}(\boldsymbol{Q},\omega) = \frac{1}{2\pi}\sum_{\boldsymbol{r}}\int_0^\infty dt e^{i\boldsymbol{Q}\cdot\boldsymbol{r}-\omega t}\langle S_0^\alpha(0)S_{\boldsymbol{r}}^\beta(t)\rangle, \quad (2.3.14)$$

Where $\langle S_0^\alpha(0)S_{\boldsymbol{r}}^\beta(t)\rangle$ is the time-dependent spin-spin correlation function describing how the α component at position 0 correlates with the β component of another spin at position $\boldsymbol{r}$ after time t.

Since the scattering function is the Fourier transform in space and time of the spin-spin correlation function, the evolution of the system of spins in space and time can be directly measured in a neutron scattering. In a magnetically ordered system, the differential cross section for coherent elastic scattering can be written as

$$\frac{d\sigma}{d\Omega} = N_M \frac{(2\pi)^3}{V_M}\sum_{G_M}\delta(\boldsymbol{Q} - \boldsymbol{G}_M)|\boldsymbol{F}_M(\boldsymbol{G}_M)|^2, \quad (2.3.15)$$

where N_M, V_M and G_M are the volume of the magnetic unit cell, the number of such cells in the sample, and the reciprocal lattice vector of the magnetic unit cell, respectively. The term $F_M(G_M)$ is the magnetic structure factor and it is defined a

$$\boldsymbol{F}_M(\boldsymbol{G}_M) = p\sum_j f_j \boldsymbol{G}_M \times (\langle \boldsymbol{M}_j\rangle \times \boldsymbol{G}_M)e^{i\boldsymbol{G}_M\cdot\boldsymbol{r}_e - W_j}, \quad (2.3.16)$$

where f_j and $\boldsymbol{M}_j$ are the magnetic form factor and the thermal-averaged magnetic moment of j-th ion, respectively. The sum in the above equation is over all sites within the magnetic unit cell. The integrated intensity of a magnetic Bragg peak for unpolarized neutrons is given by

$$I = C\frac{|\boldsymbol{F}_M(\boldsymbol{G}_M)|^2}{\sin 2\theta}, \tag{2.3.17}$$

where C is a constant depending on the incident neutron flux, sample volume, and counting time, and θ is the scattering angle. Therefore, the magnetic spin structure can be determined from the elastic magnetic peak intensity measurement.

There are two main types of neutron sources: reactor and spallation neutron sources. For this doctoral research, the cobaltates have been studied with reactor-based triple axis spectrometers, while the phonon or maganon excitations have been studied with either TAS or spallation-based time-of-flight spectrometers.

As shown in Fig. 2.6(a), the three axes correspond to the axes of rotation of the monochromator, the sample and the analyzer. The monochromator defines the direction and magnitude of the momentum of the incident beam and the analyzer performs a similar function for the scattered or final beam. In an elastic scattering event, the neutron is deflected but loses or gains no energy. In an inelastic event, neutron loses or gain energy during the interaction. In both cases, the neutron is scattered through the 2θ angle.

For time-of-flight spectrometer, a single incoming energy is selected, and the final energy and momentum transfer is analyzed by time-of-flight and detector angle φ. The neutrons arrive at the sample in monochromatic pulses of known energy. After scattering from the sample they are detected in fixed arrays of detectors as a function of their total

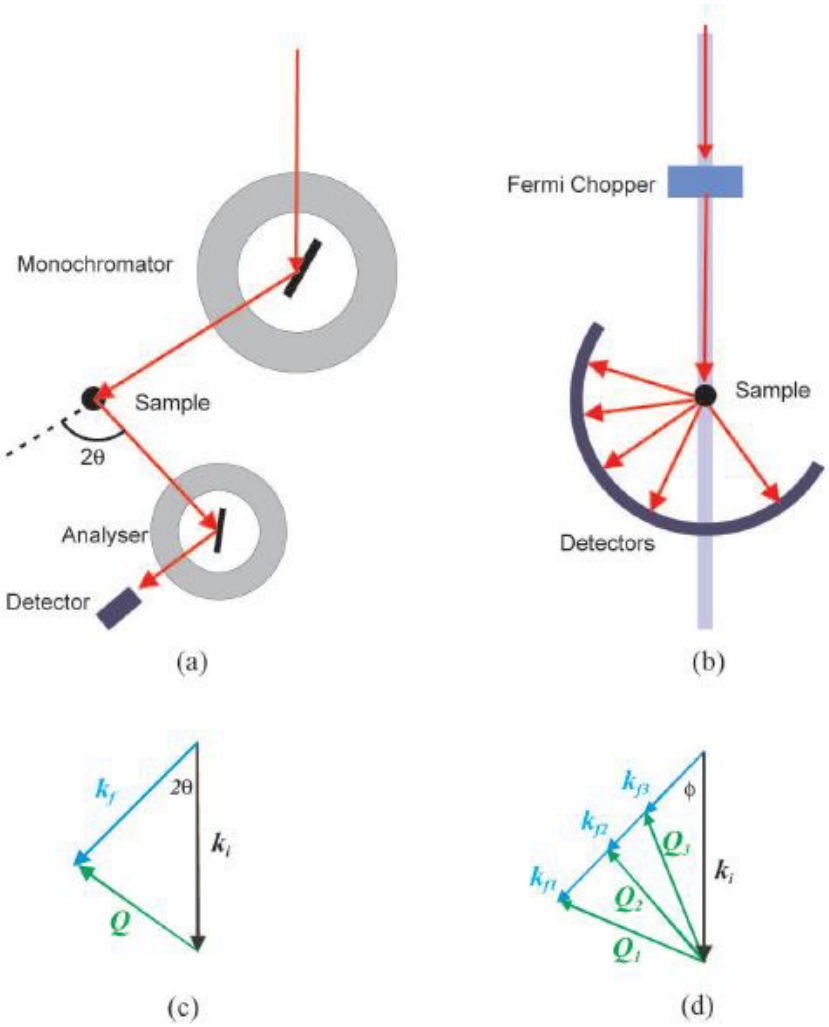

Figure 2.6 (a) The schematic of the fundamental components of a triple axis spectrometer. (b) Schematic for the time ordered processed in a time-of- flight spectrometer. (c) The scattering triangle shows that neutron is scattered through angle 2θ. The elastic neutron scattering event occurs when neutrons do not gain or lose momentum. Otherwise, it is elastic neutron scattering. (d) With time-of-flight spectrometer, energy spectrum over a wide range of wave vector can be measured simultaneously**.**

time-of-flight. With the knowledge of the sample detector distances and the incident beam energy, the final energy can be calculated. For all energies the final wave vector will lay along the same direction, however, the magnitude will decrease with the velocity of the incident energy neutrons. The scattering triangle is thus altered in time.

The main disadvantage of triple axis spectrometer is that it can only examine one position at a time in the (Q, E) space. Time-of-flight spectrometers are capable of collecting energy spectra for a wide range of wave vectors simultaneously, as shown in Fig. 2.6(d).

Nuclear Elastic Scattering

The coherent nuclear elastic scattering cross section is given by

$$\frac{d\sigma}{d\Omega} = N\frac{(2\pi)^3}{V_0}|F_N(\boldsymbol{Q})|^2, \tag{2.3.18}$$

whene N is the number of unit cells in the crystal, V_0 is the volume of the unit cell and F_N is the nuclear structure factor.

$$F_N(\boldsymbol{Q}) = \sum_j \bar{b}_j e^{i\boldsymbol{Q}\cdot\boldsymbol{r}_j} e^{-W_j(\boldsymbol{Q},T)}, \tag{2.3.19}$$

where the sum runs over all atoms j, r_j is the position of the j^{th} atom, $\bar{b}_j$ is the nuclear scattering length of the j^{th} atom and W_j is the Debye-Waller factor for the j^{th} atom, which takes account of the fluctuations of the atom due to finite temperature. Note that the cross section stated in Eq. 2.3.18 is that for coherent nuclear scattering. There is also an incoherent cross section which gives rise to an isotropic background scatter, which must be subtracted from any data before analysis is performed.

The Debye-Waller factor is included in Eq. 2.3.19 because the atoms are not frozen to their lattice sites, but rather they undergo a certain amount of thermal motion about an equilibrium position. As temperature increases this thermal motion also increases, and the result is that the intensity of the Bragg peaks decreases, this decrease being parameterised by the Debye-Waller factor. For a Bravais crystal the Debye-Waller factor is defined as

$$W_j(\boldsymbol{Q},T) = \frac{1}{2}\langle\left(\boldsymbol{Q}\cdot\boldsymbol{u}_j(T)\right)^2\rangle, \tag{2.3.20}$$

where $\boldsymbol{u}_j(T)$ is the thermal displacement of atom j from its equilibrium position.

Magnetic Elastic Scattering

Let us now consider the scattering of neutrons by magnetic interactions. Neutrons have a magnetic moment given by

$$\boldsymbol{\mu}_n = -\gamma\mu_N\boldsymbol{\sigma}, \tag{2.3.21}$$

where μ_N is the nuclear magneton, γ is the gyromagnetic ratio (≈1.91) and σ is the Pauli spin operator with values ±1. The magnetic interaction potential operator $\hat{V}_M(\boldsymbol{r})$ between neutrons and the local magnetic field $\boldsymbol{B}(\boldsymbol{r})$ in a material (e.g., due to an unpaired electron) is given by

$$\hat{V}_M(\boldsymbol{r}) = -\boldsymbol{\mu}_n\cdot\boldsymbol{B}(\boldsymbol{r}). \tag{2.3.22}$$

The cross section must contain terms which are functions of wavevector $\boldsymbol{Q}$ rather than spatial coordinate $\boldsymbol{r}$, so the Fourier transform of this, $\hat{V}_M(\boldsymbol{r})$, is used. The local magnetic field can be related to the local magnetization, so that

$$\hat{V}_M(\boldsymbol{Q}) = -\boldsymbol{\mu}_n\cdot\boldsymbol{B}(\boldsymbol{Q}). \tag{2.3.23}$$

Now $\boldsymbol{B}(\boldsymbol{r}) = \nabla\times\boldsymbol{A}$, where $\boldsymbol{A}$ is the magnetic vector potential, given by

$$\boldsymbol{A}(\boldsymbol{r}) = \frac{\mu_0}{4\pi}\frac{\boldsymbol{\mu}_e\times\hat{\boldsymbol{r}}}{r^2}, \tag{2.3.24}$$

where $\hat{\boldsymbol{r}}$ is a unit vector in the direction of r, the distance from the magnetic moment $\boldsymbol{\mu}_e$ which gives rise to the magnetic field and in this case is the result of a single unpaired electron. Now

$$\nabla \times \left(\frac{\boldsymbol{\mu}_e \times \hat{\boldsymbol{r}}}{r^2}\right) = \frac{1}{2\pi}\int \hat{\boldsymbol{q}} \times (\boldsymbol{\mu}_e \times \hat{\boldsymbol{q}}) e^{i\boldsymbol{q}\cdot\boldsymbol{r}} d\boldsymbol{q} \tag{2.3.25}$$

arises as a consequence of vector algebra[6] so we can rewrite Eq. 2.3.23 as

$$\hat{V}_M(\boldsymbol{Q}) = -\mu_0 \boldsymbol{\mu}_n \cdot \boldsymbol{M}_\perp(\boldsymbol{Q}), \tag{2.3.26}$$

where $\boldsymbol{M}_\perp(\boldsymbol{Q})$ is the component of the electron's magnetic moment (because of spin and orbital contributions) perpendicular to the scattering wavevector, such that

$$\boldsymbol{M}_\perp(\boldsymbol{Q}) = \hat{\boldsymbol{Q}} \times \left[\boldsymbol{\mu}_e(\boldsymbol{Q}) \times \hat{\boldsymbol{Q}}\right], \tag{2.3.27}$$

where $\hat{\boldsymbol{Q}}$ is a unit vector pointing in the direction of the scattering wavevector $\boldsymbol{Q}$.

We must now consider the implications of the fact that the neutrons magnetically scattered by electrons will not necessarily consist of a spherical wave, so to formulate scattering cross sections that assume that the incident and scattered beams are plane-waves a correction factor must be applied. We make the dipole approximation so that rather than using the complicated form for the magnetization in $\boldsymbol{M}(\boldsymbol{Q})$ in Eq. 2.3.26 we are able to use the dipole moment of the scattering electrons μ. For a $3d$ ion the total angular momentum J is often not a good quantum number because the orbital angular momentum L is quenched. Under such circumstances the magnetization can be written as

$$\boldsymbol{M}(\boldsymbol{Q}) = -g\mu_B f(\boldsymbol{Q})\boldsymbol{S} = f(\boldsymbol{Q})\boldsymbol{\mu}, \tag{2.3.28}$$

where $\boldsymbol{S}$ is the spin quantum number, and $f(\boldsymbol{Q})$ is the magnetic form factor. If we denote the normalized spin density by $\boldsymbol{S}$, then the form factor is defined, for the spin-only case, as the Fourier transform of S, i.e.,

$$f(\boldsymbol{Q}) = \int d^3\boldsymbol{r} e^{i\boldsymbol{Q}\cdot\boldsymbol{r}} S(\boldsymbol{r}). \tag{2.3.29}$$

[6] See appendix B of the book by Squires [81].

The derivation of the explicit form of the form factor $f(\boldsymbol{Q})$ is rather complicated and is omitted here for brevity. For a full derivation see the work of Freeman [82].

In fact $f(\boldsymbol{Q})$ can be approximated analytically using Bessel functions, which can themselves be approximated in terms of sums of exponentials with suitable coefficients. These coefficients have been found by experiment. If we define s as

$$s = \frac{\sin\theta_s}{\lambda} = \frac{|\boldsymbol{Q}|}{4\pi}, \tag{2.3.30}$$

where θ_s is the Bragg angle at the sample, and λ is the wavelength of the incident neutrons, then the analytic approximations for the expectation values of the Bessel functions are

$$\langle j_0(s)\rangle = Ae^{-as^2} + Be^{-bs^2} + Ce^{-cs^2} + D, \tag{2.3.31}$$

$$\langle j_{n>0}(s)\rangle = \left(Ae^{-as^2} + Be^{-bs^2} + Ce^{-cs^2} + D\right)s^2. \tag{2.3.32}$$

As an illustration the coefficients for Cu^{2+} are given in table 2.1

n	A	a	B	b	C	c	D
0	0.0232	34.969	0.4023	11.564	0.5882	3.843	-0.0137
2	1.5189	10.478	1.1512	3.813	0.2981	1.389	0.0017
4	-0.3914	14.740	0.1257	3.384	0.2548	1.255	0.0103

Table 2.1 The Bessel function coefficients for the Cu^{2+} form factor.

Finally, we end up with an expression for the magnetic form factor for a pure $(x^2 - y^2)$ orbital[7]:

[7] See reference [83] for a derivation of this.

$$f(\boldsymbol{Q}) = \langle j_0(\boldsymbol{Q})\rangle - \frac{5}{7}(1 - 3\cos^2\beta)\langle j_2(\boldsymbol{Q})\rangle$$

$$+ \frac{9}{56}\left(1 - 10\cos^2\beta + \frac{35}{3}\cos^4\beta\right)\langle j_4(\boldsymbol{Q})\rangle, \quad (2.3.33)$$

where β is the angle between the scattering wavevector and the axis perpendicular to the $x^2 - y^2$ orbital plane. Note that for a spherical charge density (i.e. $L = 0$, so spin-only) this simplifies considerably to

$$f(\boldsymbol{Q})_{\text{spherical}} = \langle j_0(\boldsymbol{Q})\rangle. \quad (2.3.34)$$

For magnetic elastic scattering:

$$\frac{d\sigma}{d\Omega} = N\frac{(2\pi)^3}{V_{\text{mag}}}\left(\frac{\gamma r_0}{2}\right)^2 \sum_{\alpha\beta}\left(\delta_{\alpha\beta} - \hat{Q}_\alpha\hat{Q}_\beta\right)\langle F^{(\alpha)}(-\boldsymbol{Q})\rangle\langle F^{(\beta)}(\boldsymbol{Q})\rangle, \quad (2.3.35)$$

where N is the number of magnetic unit cells, V_{mag} is the volume of the magnetic unit cell, γ is the gyromagnetic ratio, $r_0 = 2.8 \times 10^{-15}$ m is the classical electron radius and the sum over α and β is a sum over all combinations of two Cartesian axes (i.e. *xx*, *xy*, *xz*, …). $\hat{Q}_\alpha$ is a unit vector parallel to the α component of the scattering wavevector, and $\delta_{\alpha\beta}$ is the Kronecker delta. $F^{(\alpha)}(\boldsymbol{Q})$ is the α component of the magnetic unit cell structure factor. It is given by

$$F^{(\alpha)}(\boldsymbol{Q}) = \sum_j \mu_j^{(\alpha)} f_j^{(\alpha)}\, e^{i\boldsymbol{Q}\cdot\boldsymbol{r}_j} e^{-W_j(\boldsymbol{Q},T)}, \quad (2.3.36)$$

where the sum runs over all atoms, $\mu_j^{(\alpha)}$ is the α component of the magnetic moment of the j^{th} atom, and $f_j^{(\alpha)}$ is the α component of the magnetic form factor of the j^{th} atom, respectively.

Magnetic Inelastic Scattering

Let us consider now the case of an inelastic scattering process, i.e., one in which the neutron gains or losses energy during the scattering process. The cross section for magnetic inelastic scattering, in the dipole approximation for the case of spin-only scattering, is given by

$$\frac{d^2\sigma}{d\Omega dE} = \left(\frac{\gamma r_0}{2}\right)^2 f^2(\boldsymbol{Q}) e^{-2W(\boldsymbol{Q},T)} \frac{k_f}{k_i} S(\boldsymbol{Q},\omega), \tag{2.3.37}$$

where $S(\boldsymbol{Q},\omega)$ is the response function which is given by

$$S(\boldsymbol{Q},\omega) = \sum_{\alpha\beta} \left(\delta_{\alpha\beta} - \hat{Q}_\alpha \hat{Q}_\beta\right) S^{\alpha\beta}(\boldsymbol{Q},\omega), \tag{2.3.38}$$

and the $S^{\alpha\beta}$ are the space and time Fourier transforms of the time dependent spin-spin correlation functions, given by

$$S^{\alpha\beta}(\boldsymbol{Q},\omega) = \frac{1}{2\pi\hbar} \int_{-\infty}^{+\infty} \sum_{jj'} e^{i\boldsymbol{Q}\cdot(\boldsymbol{r}_j - \boldsymbol{r}_{j'})} e^{-i\omega t} \langle S_{j'}^{\alpha}(0) S_j^{\beta}(t)\rangle \, dt, \tag{2.3.39}$$

where $S_j^{\beta}(t)$ is the β-component of the spin at site j at time t, and $\langle \ldots \rangle$ denotes an average over the initial states of the system. This expression can be considerably simplified if we consider a system where the excitations are out of the ground state only[8]. The ground state has wavefunction $|0\rangle$ and energy E_0, and the spin-spin correlation function is given by

$$S^{\alpha\beta}(\boldsymbol{Q},\omega) = \sum_{\lambda} |\langle\lambda|S^{\alpha}(\boldsymbol{Q})|0\rangle|^2 \delta(\hbar\omega - E_0 - E_\lambda), \tag{2.3.40}$$

where the where the sum is over all eigenstates $|\lambda\rangle$ of the final state of the system with

[8] Strictly speaking this means a system at zero temperature, however for non-zero temperatures the simplification described is still a good approximation provided that the excited state lies at an energy greater than $k_B T$ above the ground state.

energy E_λ. $S^\alpha(\boldsymbol{Q})$ is the Fourier transform of the α-component of the spin is the Fourier transform of the spin S_j^α.

Principle of Detailed Balance

The principle of detailed balance relates the response function for neutron energy loss and neutron energy gain processes with equal and opposite wavevectors. It accounts for the fact that at any given temperature there will be a fraction $e^{-\hbar\omega/k_BT}$ fewer excitations already extant for neutrons to scatter from, compared to the number of excitations that can be created by the neutron. Mathematically this is given by

$$S(\boldsymbol{Q},\omega) = e^{\frac{\hbar\omega}{k_BT}} S(-\boldsymbol{Q},-\omega), \tag{2.3.41}$$

Fluctuation Dissipation Theorem

The fluctuation dissipation theorem relates the imaginary part of the dynamic susceptibility $\chi''(\boldsymbol{Q},\omega)$ to the response function $S(\boldsymbol{Q},\omega)$. Mathematically this relationship is given by

$$S(\boldsymbol{Q},\omega) = [1+n(\omega)]\frac{1}{\pi}\chi''(\boldsymbol{Q},\omega), \tag{2.3.42}$$

where $n(\omega)$ is the Bose population factor

$$n(\omega) = \frac{1}{e^{-\hbar\omega/k_BT}-1}. \tag{2.3.43}$$

Also note the sum rule that relates the imaginary part of the dynamic susceptibility to the bulk susceptibility:

$$\chi_{\text{Bulk}} = \lim_{Q\to 0}\int_{-\infty}^{+\infty}\frac{\chi''(\boldsymbol{Q},\omega)}{\pi\omega}d\omega. \tag{2.3.44}$$

2.4 Structure Determination

2.4.1 *Introduction*

The analysis of crystal structures and magnetic ordering is usually based on diffraction phenomena caused by the interaction of matter with X-rays, neutrons, or electrons. Even though electron microscopy can achieve atomic resolution, more detailed information on the 3-dimensional atomic arrangement of crystals with its symmetry and chemical bonding, as well as 3-dimensional magnetic structures and spin densities, requires diffraction methods. The basic theory of diffraction is the same for all types of radiation. Complementary information is achieved due to the different character of X-rays, neutrons and electrons, and hence their different interactions with matter and further practical aspects.

Considering only X-rays and thermal neutrons, one finds that their wavelengths are similar (0.5Å $< \lambda <$ 2.4Å). While the electromagnetic X-ray radiation yields the total electron density distribution, the nuclear scattering of neutrons probes the density of distribution of the nuclei and the magnetic neutron scattering determines the spin density of unpaired electrons. In the following sections, we will introduce briefly X-ray and neutron diffraction which are required to solve structural problems. X-ray diffraction using conventional laboratory equipment and/or synchrotron installations is the most important method for structure analysis. Even though the huge intensity of modern synchrotron sources allows in principle the study of magnetic X-ray scattering, the investigation of magnetic structures is still one of the most important applications of neutron diffraction.

2.4.2 *X-ray/Neutron Powder Diffraction*

X-ray/neutron powder diffraction is a non-destructive technique widely applied for the characterization of crystalline materials [84]. This method has been traditionally used for phase identification, quantitative analysis and the determination of structure imperfections. Important advances in structural studies of materials ranging from high temperature superconductors and high pressure research have relied heavily on the powder diffraction technique [84]. More detailed information on recent developments can be obtained from references [85–90]. In this section we took the liberty to drop out the term X-ray as we completely concentrated on the techniques that are applicable to instruments using X-rays. Neutron powder diffraction follows the same principle as X-ray diffraction.

Overview

Some solids can be prepared only as micro crystalline powders and hence their structure cannot be determined using single crystal diffraction techniques. Also the structures of some materials which are in the form of hydrocarbons and resins cannot be determined by single crystal diffraction methods. In such cases we can determine the structure of the material using powder diffraction data. The ability to determine crystal structures using powder diffraction promises to open up many avenues in structural sciences. Powder diffractometry projects the three-dimensional lattice into a one-dimensional lattice. We can determine the orientation, unit cell dimensions, stress/strain, crystal structure, etc., from the information obtained in the powder diffraction pattern.

The steps involved in this process are [84]

- Unit cell determination.
- Decomposition of powder pattern into integrated intensities.
- Assignment of space group from systematic absences.
- Forming an approximate solution using direct or traditional techniques.
- Refinement of the structure, typically by the Rietveld method.

However the determination of structures using powder diffraction data is much more difficult than from single crystal data. This problem arises as a result of the collapse of the three dimensional crystallographic information into a single dimensional one of which is the powder diffraction pattern. This ambiguity creates problems in the determination of the unit cell. However with the improvements in the instrument and algorithmic developments it is now possible to solve different structures from powder diffraction data alone. Now powder diffraction has become the promising technology in the characterization of crystalline materials. [91]

Bragg's Condition

Consider a beam of wavelength λ striking a line of atoms spaced at equal distances. The radiated beam that is in the form of spherical wavefronts will be of maximum intensity when the path difference between the incident and the reflected beam is equal to an integer number of wavelengths [84]. Taking a picture where each atom is giving off a spherical wave front, the directions of scattering thus constitute a series of cones. If we take a 2-D net, in which there is another line of atoms independent from the first line of atoms, another series of cones is generated. Thus a 2-D net produces two families of intersecting cones. Thus a constructive interference in seen only in some specific well

defined directions in space. Also when the axes of the cones are non-linear, the intersections of the cones give a series of lines.

Extending this idea to three dimensions, strong constructive interference will occur only for some specific conditions of interference and specific directions. But it is difficult to picture this in three dimensions. However, Bragg proposed that the condition for constructive interference is equivalent to that of a simple plane, which can be described by the Miller indices. Now the plane is (*hkl*) and the spacings between the planes are considered but not the spacings between the atoms or lattice points as was considered previously.

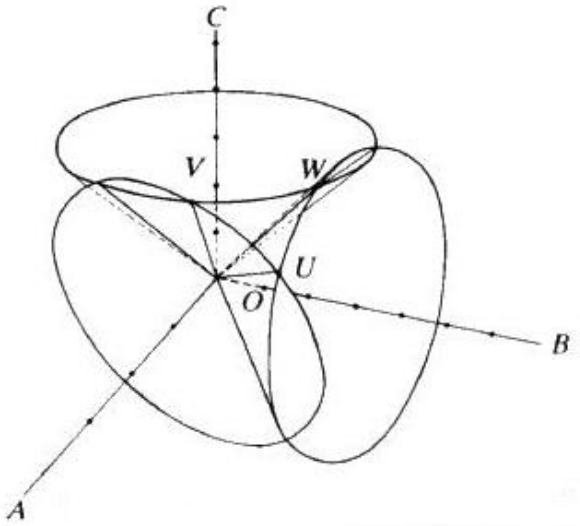

Figure 2.7 The general case for the intersection of diffraction cones coaxial with three noncoplanar rows.

A 3-D scattering of x-rays can be seen in Fig. 2.7. Consider a crystal lattice whose interplanar spacing is *d*. Also the incident radiation strikes the planes (*hkl*) at an angle θ as shown in Fig. 2.8. The condition for constructive interference is now:

$$n\lambda = 2d \sin\theta, \tag{2.4.1}$$

where λ is the incident wavelength, $n = 0, 1, 2, 3, \ldots$

From the Eq. 2.4.1, we can see that $\sin\theta$ is a measure of $1/d$. We can choose the incident angle by rotating the crystal relative to the beam and the wavelength is fixed. Thus we obtain the interplanar spacing d, as shown in Fig. 2.8. We can now conclude that any set of planes in a crystal will reflect an x-ray beam if the set of planes is at right angle ($\theta = 90°$) to the incident beam. But there arises another question whether the planes will reflect the beam strongly or not. The intensity of the reflected beam is proportional to the product of the intensity of the incident beam and the concentration of electrons in the reflecting plane. Thus if we know the unit cell dimensions and the atomic number of each of the atoms, we can calculate the concentration of electrons and hence the intensity of the reflected beam.

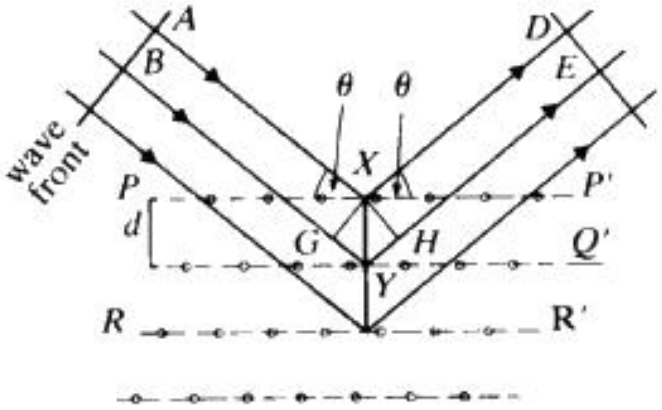

Figure 2.8 Geometrical illustration of the Bragg's law.

Now considering the reverse situation, if we know the size of the unit cell and the intensities of the reflections we can calculate the positions of atoms and also the relative number of electrons per atom. It is obvious that all compounds with different

formulae or unit cells have different collections of *d*-spacings and different intensities of reflections. The observed patterns of spacings and intensities can thus be used to identify an unknown compound in a specific crystalline phase.

Powder Diffraction

If monochromatic X-ray radiation is taken instead of white light and the crystal is placed in front of the beam, there will be only one reflected beam for one particular angle of incidence. If the crystal is now rotated around the incident ray direction without changing the incident angle, the reflected beam will describe a cone with the crystal at

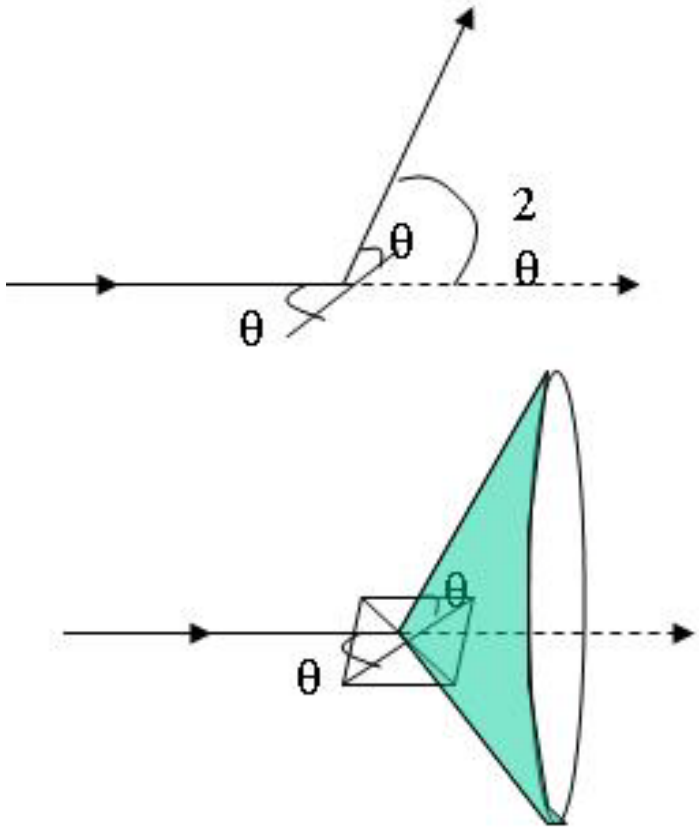

Figure 2.9 The origin of the powder diffraction cone as the result of the infinite number of the completely randomly oriented identical reciprocal lattice vectors.

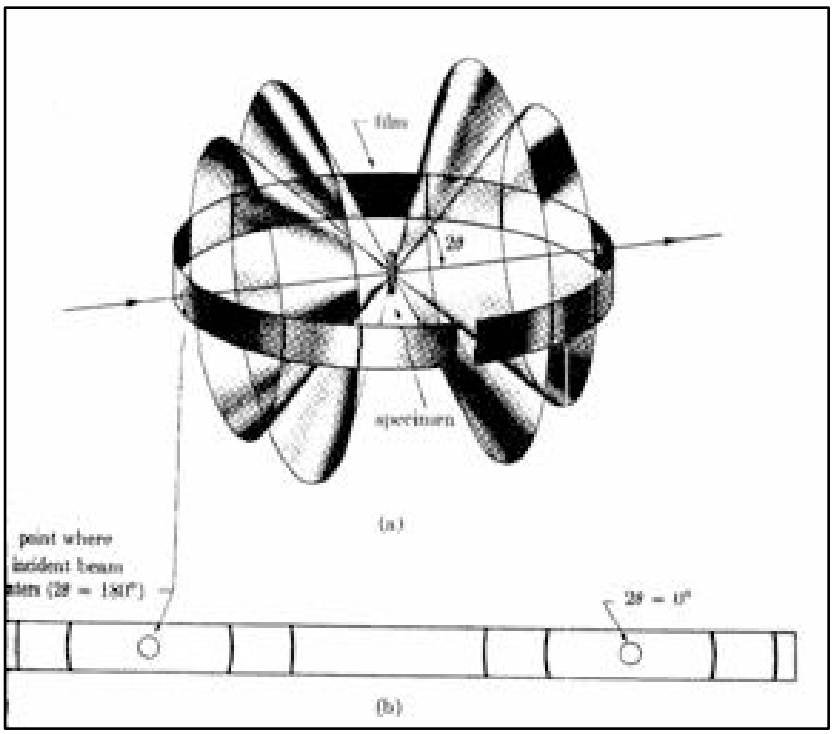

Figure 2.10 The schematic of the powder diffraction cones produced by a poly-crystalline sample**.**

the apex of the cone as shown in Fig. 2.9. When there are hundreds of crystals, there are many reflected beams and when the crystals are rotated about their axes of incident x-ray beam, a series of cones are formed as shown in Fig. 2.10. If a powdered sample is placed in the path of x-rays there will be a continuous series of point reflections lying along the arc of the cone [84]. This is the basis of powder method that is used in X-ray crystallography to determine the unknown samples. For every set of crystal planes, one or more crystals will satisfy Bragg's condition.

Methods of Powder Diffraction Pattern The main methods of studying powders have led to the investigation of the atomic arrangements. The methods employed are the Debye Scherrer method and Diffractometry.

Debye Scherrer Camera One of the simplest ways of determining unit cell parameters is the Debye Scherrer method. To understand the principles involved, consider a particular (*hkl*) reflection. One or more particles will be oriented so that their (*hkl*) planes obey Bragg reflection condition. Figure 2.9 shows one plane in the set.

If the plane is now rotated such that the angle of incidence is kept constant, the reflected beam travels over the surface of the cone with the axis coinciding with the transmitted beam. Though this rotation does not occur in powder method, the combined effects of some reflections from the (*hkl*) planes make the correct Bragg angle with the incident beam and thus have the form of a cone of diffracted radiation. Thus the (*hkl*) reflection from a powder produces many cones.

In the Debye Scherrer method, a narrow strip of film is curved in a short cylinder with the specimen placed on the axis and the incident beam is directed at right angles to the axis. The cones of diffracted radiation intersect the cylindrical strip in lines and when the strip is laid straight the resulting pattern is as shown in the Fig. 2.10. Each pattern is made up of small spots each from one particle and the spots are so close to each other that they appear as a continuous line. These lines are generally curved and when $2\theta = 90°$, they form a straight line. From the measured position of a given diffraction line, θ can be determined and if we know the wavelength λ we can calculate the *d*-spacings of the lattice planes.

If the shape and size of the unit cell are known, the position of all the possible diffraction lines can be predicted. The Debye Scherrer method is widely used especially in metallurgy.

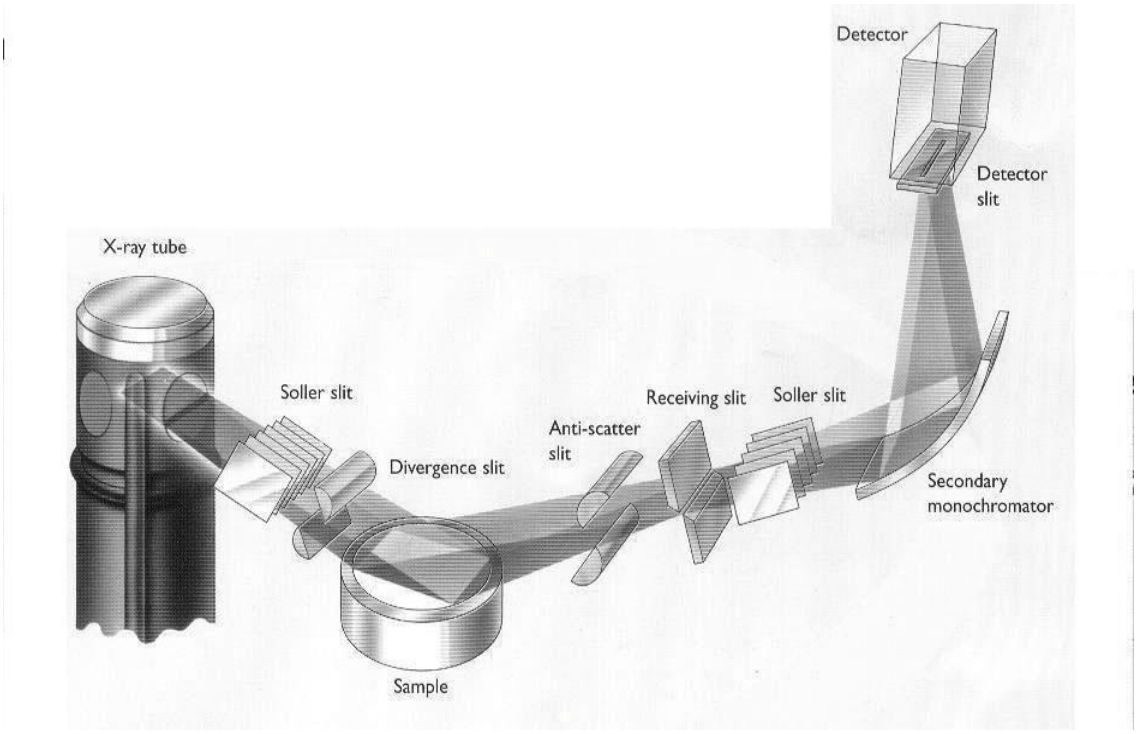

Figure 2.11 Schematic diagram of an X-ray powder diffractometers.

The Powder Diffractometer Modern X-ray techniques give a series of peaks instead of diffraction intensities as in Debye Scherrer method. In this method a detector is used instead of film. A convergent incident ray is used to give good peak resolution. The powder is filled in the hole of a sample holder. The set up requires that if reflection is obtained when the beam is incident at an angle θ with the lattice plane, the reflected beam is recorded at an angle of 2θ in what is referred to as $\theta - 2\theta$ scan. A $\theta - 2\theta$ scan is shown in Fig. 2.11. The peak positions and the intensities are readily obtained. The powder diffractometer uses an x-ray detector like a proportional or scintillation counter to measure the positions of the diffracted beams. Diffractometry is a widely used method because it measures the intensities directly. A typical powder diffraction pattern is as follows for synthetic maghemites with different zinc isomorphic substitution samples in Fig. 2.12.

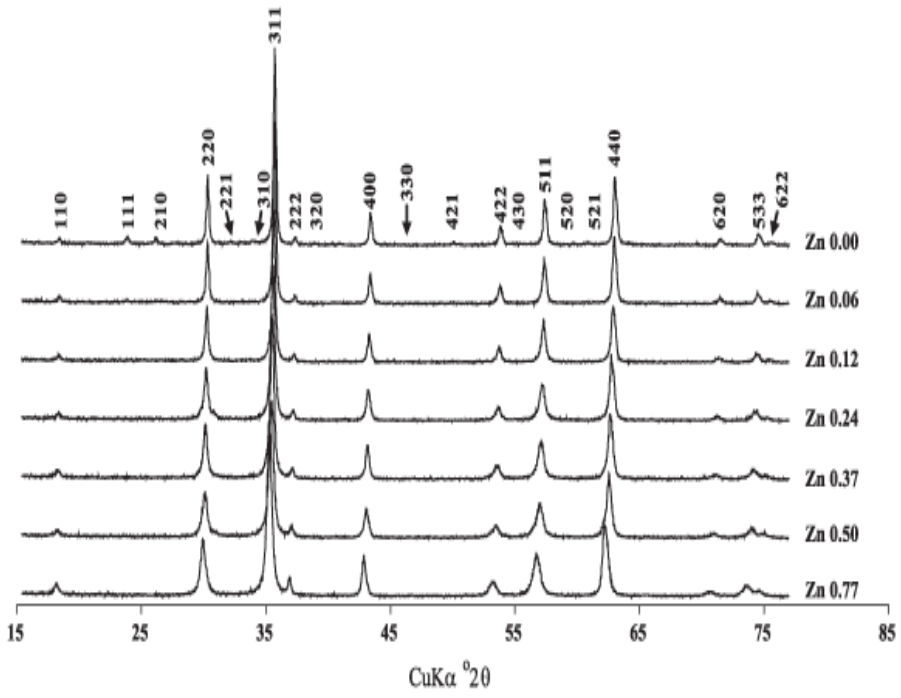

Figure 2.12 An example of powder diffraction patterns of synthetic maghemites with different zinc isomorphic substitution levels.

The positions of the peaks are directly related to the dimensions of the unit cell. The intensities are related to the contents of the unit cell. The *d*-spacings are determined because they are independent of the wavelength of the light used. Normally relative intensities are used in order to normalize the intensities. The normalization of intensities is done by taking a reference for the strongest peak and other intensities are scaled accordingly.

The x-ray powder diffraction pattern of a mixture containing two or more compounds is the weighted sum of the individual patterns. Although a powder diffraction pattern is used as a finger print for identifying a material, other important information is obtained in it, which is shown in Table 2.2.

Feature	Information obtained
Peak positions (2θ values)	Unit cell dimensions and symmetry
Non-indexable lines	Presence of a crystalline impurity
Width of peaks	Particle size/strain
Peak intensities	Unit cell contents (basis vectors) and thermal vibrations
Peak shpes (other than widths)	Stacking faults, layer defects

Table 2.2 Information obtained from a powder diffraction pattern.

Structure Determination of Powder Diffraction Patterns

Crystal structures, which cannot be determined by single crystal approaches because of inappropriate size and quality, can be easily determined using powder diffraction method. Such a structure determination can be divided into three stages:

1. Unit cell determination
2. Structure solution
3. Structure refinement

Unit cell determination The size and shape of the unit cell is determined from the positions of the lines. This is called indexing the pattern. Consider that the sample is known to have cubic structure, but that we do not know which cubic structure it has. After exposure of the sample to x-ray beam in the Debye Scherrer method, the strip is removed and the positions are measured as follows:

The distance along the film from a diffraction line to the center of the hole for the transmitted direct beam is measured. This is taken as $S1$ and shown in Fig. 2.13.

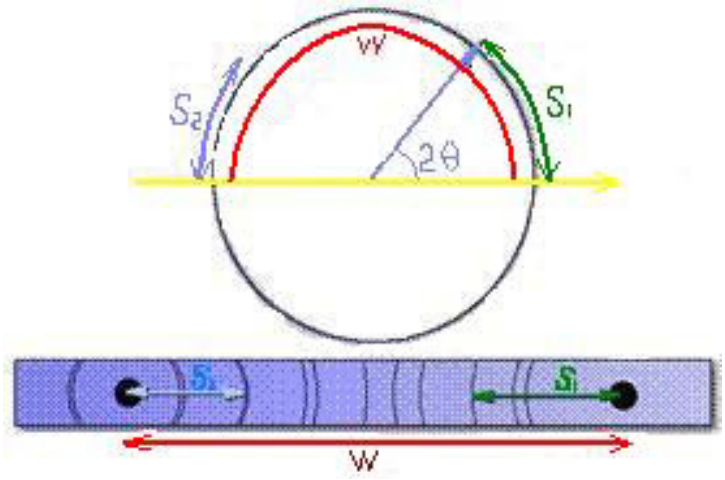

Figure 2.13 An illustration of Debye Scherrer method.

When $2\theta > 90°$, there is back reflection and *S*2 is measured. This is the distance from the beam entry point. Now we know that *S*1 corresponds to an angle 2θ. Also the distance between the holes, W, is obtained when $\theta = 180°$. Using this information we find that

$$\theta = \frac{\pi S1}{2W}, \tag{2.4.2}$$

$$\frac{\theta}{2} = \frac{\pi}{2}\left(1 - \frac{S2}{W}\right). \tag{2.4.3}$$

Bragg's law states that $n\lambda = 2d \sin\theta$. The interplanar spacing is given by

$$d_{hkl} = \frac{a}{\sqrt{h^2 + k^2 + l^2}}, \tag{2.4.4}$$

where *a* is the lattice parameter. This gives

$$\sin^2\theta = \frac{\lambda^2}{4a^2}(h^2 + k^2 + l^2). \tag{2.4.5}$$

Now from the arcs obtained in the powder method and the diffraction method we have the values of *S*1, θ and $\sin 2\theta$. If we take all the diffraction lines into

consideration, then the values of $\sin 2\theta$ should form a pattern related to the values of (*hkl*). Multiplying the values of $\sin 2\theta$ by a constant gives nearly an integer value for each of the $h^2 + k^2 + l^2$ values. This can be interpreted from the table 2.3 in which the measurements are taken for a sample.

$\lambda = 1.54\text{Å}$ $W = 180\text{mm}$						
S_1 (mm)	θ	$\sin^2\theta$	$K\sin^2\theta$	$h^2 + k^2 + l^2$	*hkl*	$a(\text{Å})$
38	19.0	0.11	3.0	3	111	4.05
45	22.5	0.15	4.1	4	200	4.02
66	33.0	0.30	8.2	8	220	4.02
78	39.0	0.40	10.9	11	311	4.04
83	41.5	0.45	12.3	12	222	4.02
97	49.5	0.58	15.8	16	400	4.04
113	56.5	0.70	19.1	19	331	4.03
118	59.0	0.73	19.9	20	420	4.04
139	69.5	0.88	24.0	24	422	4.01
168	84.0	0.99	27.0	27	511	4.03

Table 2.3 Step by step calculations for the lattice parameter.

Now the integer values of $h^2 + k^2 + l^2$ are equated with the integer values of *hkl* and are obtained. This is shown in the Table 2.4.

Sometimes for some structures, some of the arcs may be missing as in the case of body-centered (BCC) and face-centered (FCC) structures. Then it becomes easy to identify the structure. The value of the lattice parameter can also be calculated from the 2θ positions of the *hkl* lines and may be refined for systematic errors.

$h^2 + k^2 + l^2$	*hkl*
1	100
2	110
3	111
4	200
5	210
6	211
8	220
9	221
10	310
11	311
12	222
13	320
14	321
16	400

Table 2.4 Values of $h^2 + k^2 + l^2$ calculated from possible *hkl* planes in any structure.

Structure Solution In structure solution an initial approximate structure is obtained from experimental data without having any prior knowledge of the arrangement of the atoms and molecules. This is a very important phase in the determination of structure.

There are two techniques for structure solution: [84]

- Traditional approach
- Direct space approach

In the traditional approach, the intensities are taken from the powder pattern and they are used in the calculation that is used for single crystal diffraction data. But this may not be a reliable approach as there are many overlapping peaks and hence the intensity values obtained are not exact. This problem can be overcome by using improved

techniques for extracting intensities or new strategies in which the pattern is obtained without extracting intensities. The experimental pattern generates trial structures. This comparison is done using an appropriate *R*-factor. Most of the direct space approaches use the weighted *R*- factor which is R_{wp}. This is given by [84]

$$R_{wp} = 100 \times \frac{\sum W_i(y_i(\text{obs}) - y_i(\text{calc}))^2}{W_i\left(y_i(\text{obs})\right)^2}, \tag{2.4.6}$$

where $y_i(\text{obs})$ is the intensity of the i^{th} data point in the experimental powder pattern. $y_i(\text{calc})$ is the intensity of the i^{th} data point in the calculated powder diffraction profile. W_i is the weighting factor for the i^{th} data point. R_{wp} thus considers the intensities point by point instead of the integrated intensities. This reduces the peak overlap and uses the powder diffraction data as measured.

The basis of Direct Space Strategy is to find a hyper surface $R(\Gamma)$ to find the global minimum. Here Γ represents the set of variables that define the surface. These variables define the position, orientation and the intra molecular geometry of each molecule. The position is defined by $\{x, y, z\}$, orientation by $\{\theta, \varphi, \psi\}$ and the intra molecular geometry is represented by the set of variables $\{\tau_1, \tau_2, \tau_3, \dots, \tau_n\}$. The intensities, peak positions and the peak shapes can be determined prior to the structure solution method by using a fitting procedure. There are many techniques for determining the lowest value on the $R(\Gamma)$ surface. They are:

- Monte Carlo Method

  This method can be explained in a series of steps:

  1. Starting from structure τ_j, another structure τ_{j+1} is obtained by making small random displacements to each of the structural variables $\{x, y, z,$

θ, φ, ψ, τ_1, τ_2, τ_3, … , $\tau_n\}$. The weighted R-factor is used to assess the experimental data and the calculated pattern.

2. The trial structure is then accepted or rejected according to the difference $Z = R_{wp}(\Gamma_j \text{ trial}) - R_{wp}(\Gamma_j)$. if $Z = 0$, the trial structure is accepted with probability $e^{-Z/S}$ and rejected with the probability $1 - e^{-Z/S}$, where S is a scaling factor. If the trial structure is accepted Γ_{j+1} is taken the same as Γ_j trial. If it is rejected then structure Γ_{j+1} is taken as the same as Γ_j.

This procedure is repeated to generate a large number of structures and the structure that has the lowest value of R_{wp} is considered the starting structure for structure refinement.

In the Monte Carlo method the value of S is either a fixed value or changes manually. But in the case of Simulation technique the value of S is decreased systematically according to an annealing schedule. This is the essential difference between the Monte Carlo method and the Simulation Annealing technique.

- Genetic Alogrithm

This technique involves simultaneous investigation of the different regions on $R(\Gamma)$ hyper surface. In this method an initial population of structures P_0 is evolved. This population of structures is then evolved into another population with the same number of structures by the operations: *mating*, *mutation* and *natural selection*. Thus a given generation P_j is evolved into a new generation P_{j+1}.

In mating procedure a given number of pairs of structures are selected from the given population. For each pair of parents, offsprings are generated. Consider an example of two structures as parents described by $\{x_a, y_a, z_a, \theta_a, \varphi_a, \psi_a\}$ and $\{x_b, y_b, z_b, \theta_b, \varphi_b, \psi_b\}$. The two offsprings can be generated as $\{x_a, y_a, z_a, \theta_b, \varphi_b, \psi_b\}$ and $\{x_b, y_b, z_b, \theta_a, \varphi_a, \psi_a\}$. Thus the mating procedure does not create any new values of genetic variables but only distributes the variables of the parent structures.

In mutation, new values of variables are generated. This is done by taking a set of structures and making random changes to the parts of the genetic code to generate new mutant structures. This can be done either by taking new random values (static mutation) or making random displacements to the existing values (dynamic mutation).

In natural selection procedure only the best structures (i.e. closest value of R_{wp}) are passed on from one generation to another. When the population has evolved that contains the better structures, the one with the lowest values is again taken from these set of structures and taken to be the starting one for refinement.

- Simulated Annealing

Structure Refinement The structure refinement is a method to get the exact structure from the data obtained in the structure solution method. Thus, if the structure solution is a good approximation to the original structure, a good quality structure may be obtained by Structure Refinement. Structure refinement is generally carried out by the Rietveld method.

Rietveld method is considered the best method to obtain an exact structure even if there are peak overlaps [92]. It is nothing but the least squares method to obtain the most feasible solution. The procedure used in practice is to minimize the chi-square function, as shown in the Eq. 2.4.7 [92]

$$\chi_p^2 = \sum_i W_i(y_i(\text{obs}) - y_i(\text{calc}))^2, \qquad (2.4.7)$$

where W_i is the inverse of the variance associated to the observation "i"$\left(\sigma^2\left(y_i(\text{obs})\right)\right)$. The weighted sum of squared difference between $y_i(\text{obs})$ and $y_i(\text{calc})$ is minimized.

This equation looks very similar to Eq. 2.4.6, solved in the Monte-Carlo method. The difference in both these lies in considering the data points. In the Monte Carlo method all readable peak points are considered and a solution is obtained using this data. But the data obtained from low values of 2θ have a high probability that it could be erroneous. In proceeding to the Rietveld method, these assumed erroneous data are safely removed and only a set of primary data are used to proceed further.

We have to adopt iterative techniques for this, as the problem to be solved is non-linear. If there is a feasible solution, it can be assured that it would be the actual solution. The initial approximate solution is dependent upon the nature of distribution of the counts. The mean of the distribution set is taken as the initial solution of the least square method.

In the above explained structure estimation techniques we did not include the complex math involved as we just wanted to lay out how the structure is determined. In fact, in actual Industry, the above problem is solved by various available software tools like FULLPROF, SHELX, GSAS, XRS-82, DLS-76 etc.

Applications

X-ray powder diffraction has opened up new avenues in the studies of structures. It has a number of applications.

- Qualitative analysis: From the pattern, the *d*-spacings are recorded and the relative intensities of the 10 strongest lines are measured and are compared with the patterns of the known compounds. This comparison is done with the help of a powder diffraction file that contains the patterns of some standard compounds divided into subdivisions-Minerals, Inorganic, Organic.
- Quantitative analysis: For a two-component mixture the relative concentration of each of the components can be obtained by measuring the relative intensities of the strong non overlapping lines each belonging to the two components.
- Structure of alloys: An alloy is a mixture of two or more elements. If the composition is uniform it produces a typical powder diffraction pattern. If one of the components precipitates, it produces separate lines on the powder pattern corresponding to the component.
- Stress determination in metals: If there is a stress in a metal, then the angle of the diffraction cone changes because of a change in the d-spacing. By measuring the changes in the cone angle, accurate measurements of stress can be made. In addition, stress invariably broadens diffraction peaks unless it is absolutely uniform on an atomic scale.
- Determination of particle size: As the size of the crystallite decreases, the angular spread of the reflection increases. The half height width can be used a measure of the mean particle size of the sample.

- Identification and raw material evaluation: For some complex materials, it is difficult to analyze the pattern. But since similar materials exhibit similar patterns, we can for example determine the structure of different clays as a cement material by comparing with acceptable clay and thus relate structure to properties.

Limitations

- Single crystal methods depend upon mathematical algorithms and accurate peak intensities to solve structures. Such accuracy is sometimes difficult to obtain.
- The individual peak intensities are difficult to obtain because in powder diffraction, a 3-D pattern is reduced to a 1-D pattern and analysis is done. This leads to both accidental and exact peak overlap.
- The symmetry of crystals cannot be obtained accurately in powder diffraction pattern.
- Preferred orientation can lead to inaccurate peak intensities. But both rotating the sample about its normal and rocking it about each data point can overcome this.

2.4.3 *Single-crystal X-ray Diffraction*

Overview: What is Single-crystal X-ray Diffraction

Single-crystal X-ray Diffraction is a non-destructive analytical technique that provides detailed information about the internal lattice of crystalline substances, including unit cell dimensions, bond-lengths, bond-angles, and details of site-ordering. Directly related is single-crystal refinement, where the data generated from the X-ray analysis is interpreted and refined to obtain the crystal structure.

Fundamental Principles of Single-crystal X-ray Diffraction

Max von Laue, in 1912, discovered that crystalline substances act as three-

dimensional diffraction gratings for X-ray wavelengths similar to the spacing of planes in a crystal lattice. X-ray diffraction is now a common technique for the study of crystal structures and atomic spacing. X-ray diffraction is based on constructive interference of monochromatic X-rays on a crystalline sample. These X-rays are generated by a cathode ray tube, filtered to produce monochromatic radiation, collimated to concentrate, and directed toward the sample. The interaction of the incident rays with the sample produces constructive interference (and a diffracted ray) when conditions satisfy Bragg's Law (see Eq. 2.4.1). This law relates the wavelength of electromagnetic radiation to the diffraction angle and the lattice spacing in a crystalline sample. These diffracted X-rays are then detected, processed and counted. By changing the geometry of the incident rays, the orientation of the centered crystal and the detector, all possible diffraction directions of the lattice should be attained.

All diffraction methods are based on generation of X-rays in an X-ray tube. These X-rays are directed at the sample, and the diffracted rays are collected. A key component of all diffraction is the angle between the incident and diffracted rays. Powder and single-crystal diffraction vary in instrumentation beyond this.

Interpretation of data Typical mineral structures contain several thousand unique reflections whose spatial arrangement is referred to as a diffraction pattern. Indices (*hkl*) may be assigned to each reflection, indicating its position within the diffraction pattern. This pattern has a reciprocal Fourier transform relationship to the crystalline lattice and the unit cell in real space. This step is referred to as the solution of the crystal structure. After the structure is solved, it is further refined using least-squares techniques. This procedure is described fully on the single-crystal structure refinement (SREF) page.

Single-crystal X-ray Diffraction Instrumentation - How Does It Work?

X-ray diffractometers consist of three basic elements, an X-ray tube, a sample holder, and an X-ray detector. X-rays are generated in a cathode ray tube by heating a filament to produce electrons, accelerating the electrons toward a target by applying a voltage, and the impact of the electrons with the target material. When electrons have sufficient energy to dislodge inner shell electrons of the target material, characteristic X-ray spectra are produced. These spectra consist of several components, the most common being K_α and K_β. K_α consists, in part, of $K_{\alpha 1}$ and $K_{\alpha 2}$. $K_{\alpha 1}$ has a slightly shorter wavelength and twice the intensity as $K_{\alpha 2}$. The specific wavelengths are characteristic of the target material. Filtering, by foils or crystal monochrometers is required to produce monochromatic X-rays needed for diffraction. $K_{\alpha 1}$ and $K_{\alpha 2}$ are sufficiently close in wavelength such that a weighted average of the two is used. Molybdenum is the most common target material for single-crystal diffraction, with Mo K_α radiation = 0.7107Å. These X-rays are collimated and directed onto the sample. When the geometry of the incident X-rays impinging the sample satisfies the Bragg Equation, constructive interference occurs. A detector records and processes this X-ray signal and converts the signal to a count rate which is then output to a device such as a printer or computer monitor. X-rays may also be produced using a synchrotron, which emits a beam with more intensity.

Single-crystal diffractometers use either 3- or 4-circle goniometers, see Fig. 2.14. These circles refer to the four angles (2θ, χ, φ, and Ω) that define the relationship between the crystal lattice, the incident ray and detector. Samples are mounted on thin glass fibers that are attached to brass pins and mounted onto goniometer heads. Adjustment of the X, Y and Z orthogonal directions allows centering of the crystal within the X-ray beam.

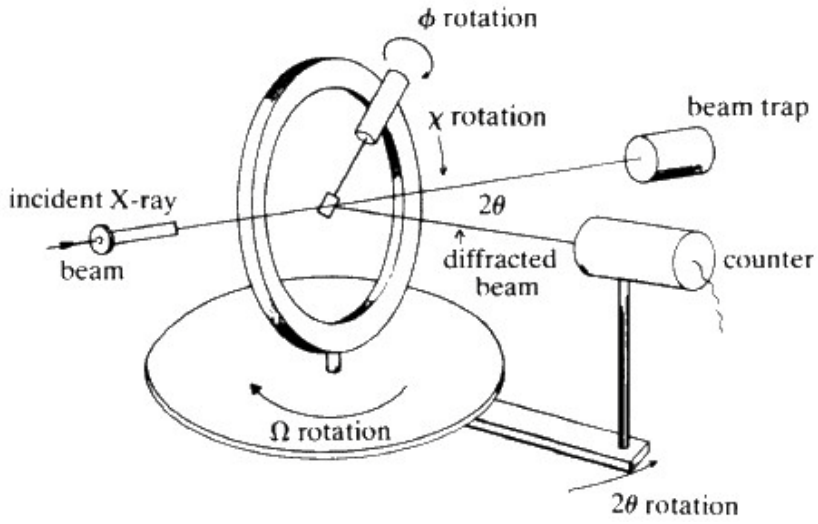

Figure 2.14 Schematic of 4-circle diffractometer; the angles between the incident ray, the detector and the sample. Image courtesy of the International Union of Crystallography.

X-rays leave the collimator and are directed at the crystal. Rays are either transmitted through the crystal, reflected off the surface, or diffracted by the crystal lattice. A beam stop is located directly opposite the collimator to block transmitted rays and prevent burn-out of the detector. Reflected rays are not picked up by the detector due to the angles involved. Diffracted rays at the correct orientation for the configuration are then collected by the detector.

Modern single-crystal diffractometers use CCD (charge-coupled device) technology to transform the X-ray photons into an electrical signal which are then sent to a computer for processing.

Applications

Single-crystal X-ray diffraction is most commonly used for precise determination of a unit cell, including cell dimensions and positions of atoms within the lattice. Bond-lengths and angles are directly related to the atomic positions. The crystal structure of a

mineral is a characteristic property that is the basis for understanding many of the properties of each mineral. Specific applications of single-crystal diffraction include:

- New mineral identification, crystal solution and refinement.
- Determination of unit cell, bond-lengths, bond-angles and site-ordering.
- Characterization of cation-anion coordination.
- Variations in crystal lattice with chemistry.
- With specialized chambers, structures of high pressure and/or temperature phases can be determined.
- Determination of crystal-chemical vs. environmental control on mineral chemistry.
- Powder patterns can also be derived from single-crystals by use of specialized cameras (Gandolfi).

Strengths and Limitations of Single-crystal X-ray Diffraction

Strengths

- No separate standards required.
- Non-destructive.
- Detailed crystal structure, including unit cell dimensions, bond-lengths, bond-angles and site-ordering information.
- Determination of crystal-chemical controls on mineral chemistry.
- With specialized chambers, structures of high pressure and/or temperature phases can be determined.
- Powder patterns can also be derived from single-crystals by use of specialized cameras (Gandolfi).

Limitations

- Must have a single, robust (stable) sample, generally between 50-250 microns in size.
- Optically clear sample.
- Twinned samples can be handled with difficulty.
- Data collection generally requires between 24 and 72 hours.

CHAPTER 3

SYNTHESIS OF $Ba_{2-x}Sr_xCoO_4$

3.1 Preparation of Polycrystalline $Ba_{2-x}Sr_xCoO_4$

Polycrystalline Ba_2CoO_4 was first studied nearly 40 years ago by Mattausch [72] and Co ions were reported to be in tetrahedral sites. But its physical properties are essentially unknown. In order to systematically investigate this novel 214- structure compound, we have to start with polycrystalline samples again, not only the pure Ba_2CoO_4, but the series of $Ba_{2-x}Sr_xCoO_4$.

Polycrystalline samples were prepared at Correlated Electron Materials Group (CEMG) at Oak Ridge National Laboratory (ORNL) as shown in Fig. 3.1.

Figure 3.1 The place where polycrystalline sample of $Ba_{2-x}Sr_xCoO_4$ was made.

The starting materials for making $Ba_{2-x}Sr_xCoO_4$ were $BaCO_3$, $SrCO_3$ and Co_3O_4 commercially produced by Alfa Aesar, based on the chemical reaction formula, Eq. 3.1.1. The purities of the samples were 99.997%, 99.994% and 99.9985%, respectively. In order to make the desired compound, stoichiometric powders were manually mixed and ground thoroughly using mortar with pestle as shown in Fig. 3.2. The time for this procedure was about 30 min. The powder was further ground using a ball mill (see Fig.

3.3) for about 45 min to be sure of fine grain size (<10 μm). Conventional furnace (see Fig. 3.4) was then used for pre-heating the powder in air which had been put into a crucible. The temperature can be pre-set with this programmable furnace and the temperature of the powder was set to gradually rise from room temperature to 1050 ˚C within 2 h and kept at this temperature for 72 h. Then the powder was taken out of the furnace and quenched to room temperature again.

$$(2-x)\mathrm{BaCO_3} + x\mathrm{SrCO_3} + \frac{1}{3}\mathrm{Co_3O_4} \rightarrow \mathrm{Ba_{2-x}Sr_xCoO_4} + 2\mathrm{CO_2}, \qquad (3.1.1)$$

Figure 3.2 Stoichiometric powder mixture.

Figure 3.3 Planetary ball mill used for grinding materials into a fine powder.

Figure 3.4 The conventional furnace for pre-heating powders.

3.2 Preparation of Single Crystalline $Ba_{2-x}Sr_xCoO_4$

As mentioned in Sec. 3.1, a conventional furnace has been used for pre-heating polycrystalline samples of $Ba_{2-x}Sr_xCoO_4$. Such a conventional furnace is also applicable for making single crystalline samples before the final step in which a floating-zone optical furnace will be accessed. But additional steps should be added in the procedure.

After the powder was carefully mixed and grinded, it was then squeezed into a balloon with the help of a glass funnel. This "sausage"-like powder rod was 12 cm long and 0.8 cm in diameter. One end of the balloon was tied tightly (see Fig. 3.5).

Figure 3.5 Powder in a balloon.

Figure 3.6 Hydraulic pressure machine.

The balloon was later pressed with the use of a hydraulic pressure machine (see Fig. 3.6) in order to make the rod solidified. Then the balloon was cut and removed and carefully transferred to a crucible. The same pre-heating process as described in Sec. 3.1 in the conventional furnace was done for 3 days. The rods after their pre-heated treatment are shown in Fig. 3.7.

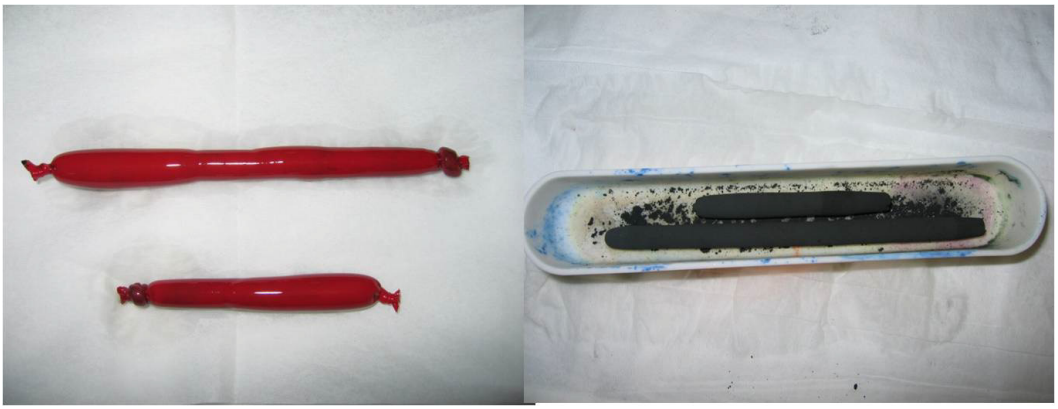

Figure 3.7 Polycrystalline rods before and after pre-heating.

Figure 3.8 NEC SC-M15HD optical furnace.

Finally, the floating-zone optical furnace was involved in synthesizing the single crystal. We used an NEC SC-M15HD image furnace for the growth, which is shown in Fig. 3.8. Two rods, one served as a feeding rod and the other served as a seeding rod,

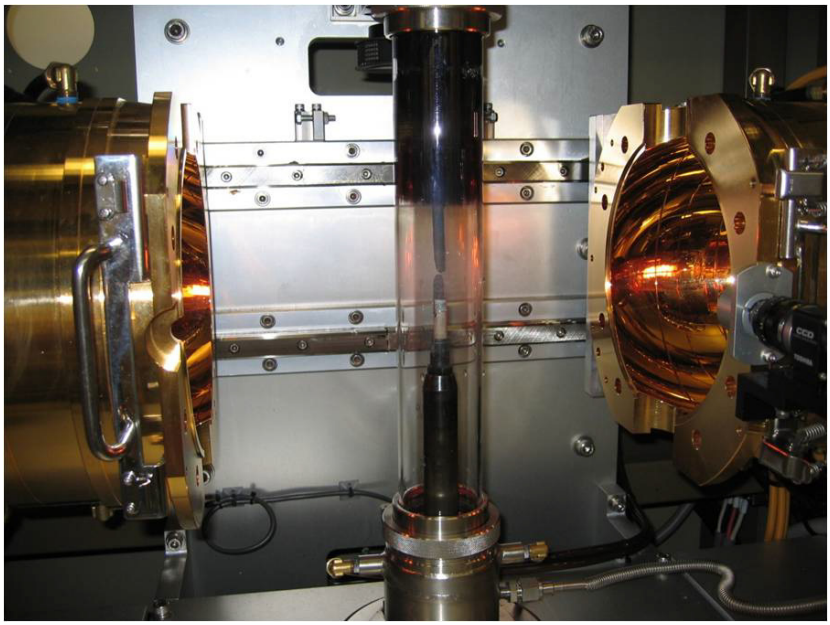

Figure 3.9 Aligned rods in the optical furnace.

Figure 3.10 Molten zone monitored on a TV screen.

were attached to the upper and lower shaft, respectively. Then they were aligned and sealed in a quartz tube (see Fig. 3.9). An oxygen atmosphere was maintained flowing during the growth of single crystals. The flow speed was set to 2.0 liter/min and the pressure in the quartz tube was kept at 1.0 MPa in order to have an oxidation environment according to the Eq. 3.1.1. It is worth noting that the oxygen pressure has to be increased as the Sr doping level increases. The electrical power was then gradually increased for the two heating Halogen lamps and the molten zone was formed as the temperature increased. The whole growth process can be monitored by a CCD camera and an external TV monitor (see Fig. 3.10). As an example, when growing Ba_2CoO_4, the current of the lamps were set to 10.21 A, the voltage was 52.37 V and the power was 534.69 W. The growth speed, e.g., the moving speed of the seed rod, was 3.0 mm/h. The rotating speed of the rods was set to 20 rpm. It is worth noting that the two rods had to be spinning in opposite direction to make the molten zone more homogeneous.

Figure 3.11 shows the single crystals Ba_2CoO_4 and $Ba_{1.5}Sr_{0.5}CoO_4$ with lengths of 6 cm and 4 cm, respectively and with a diameter of 0.5 cm. The color is dark purple. As noted previously [73], the compound had to be handled carefully, because it decomposes slowly by reacting with CO_2 and/or moisture when exposed in air for a couple of days. Therefore we have to keep the reactants in a vacuum. The growth was a trial and error process and sometimes the molten zone was not very stable. Thus the outcome was not always well-looked and actually not a single crystal as we expected (see Fig. 3.12).

Figure 3.11 Single crystals Ba_2CoO_4 and $Ba_{1.5}Sr_{0.5}CoO_4$.

Figure 3.12 Failed "crystals" after floating-zone growth.

3.3 Preparation of Polycrystalline Sr_2CoO_4

We emphasize the particular synthesis of polycrystalline Sr2CoO4 samples because it requires a high pressure and high temperature technique and we could not successfully grow single crystals in the optical furnace. Wang *et al*. [77] prepared polycrystalline samples of $Sr_{2-y}Y_yCoO_4$ (y = 0, 0.1, 0.3, 0.5, 0.67, 0.83, 1) with the help of 6 GPa in a high pressure apparatus, which is not applicable in our Floating-zone optical furnace. Approximately 0.2 g of the mixture of SrO_2, Co, and Y_2O_3 fine and pure powders was placed in a gold capsule and compressed. Then they were heated at 1000°C - 1350°C for 1-3 hours and quenched to room temperature followed by a release of pressure.

Indeed, by increasing the concentration of Sr (x) in $Ba_{2-x}Sr_xCoO_4$, higher pressure should be applied during the polycrystalline or single crystal growth. The phases in each doping concentration sample were identified using powder and single crystal X-ray diffractometers. With our current optical furnace, we could only achieve single crystals with the Sr doping concentration up to $x = 0.7$. The lattice structures and electronic or magnetic properties of $Ba_{2-x}Sr_xCoO_4$ will be discussed in the following chapters.

CHAPTER 4

LATTICE STRUCTURE OF $Ba_{2-x}Sr_xCoO_4$

4.1 Introduction

The structure of Ba_2CoO_4 was originally determined to be orthorhombic from X-ray refinement on flux-grown single crystals [72]. Later, refinement results obtained from polycrystalline samples indicated that the stoichiometric Ba_2CoO_4 crystallizes in a monoclinic structure [74, 93]. According to Negas and Roth [93], the orthorhombic phase may be stabilized at room temperature when synthesized with excess $BaCO_3$. However, we have found that single crystals grown by using rods with 10% extra $BaCO_3$ were indistinguishable from those grown using the stoichiometric composition. Therefore, stoichiometric single crystals will be used for the discussion in this chapter. Fundamentals of single crystal structure refinement will be introduced first.

4.1.1 *Motivations*

Despite the experimental and theoretical studies, there remains much controversy surrounding the lattice structure of Ba_2CoO_4 and especially, the structures of $Ba_{2-x}Sr_xCoO_4$ as the function of doping x are still unknown. The knowledge of systematic evolution of $Ba_{2-x}Sr_xCoO_4$ will be crucial to the understanding of the physical properties, as well as structural and magnetic correlations. Until now it has been possible to use conventional chemical reactions and floating-zone single crystal growth methods to obtain powder and single crystals of $Ba_{2-x}Sr_xCoO_4$. This offers the possibility of probing the lattice structure of this system.

4.2 Single Crystal Structure Refinement (SREF)

The electron density map generated by solution of the phase problem can be seen as a basic structure map. However, the assignment of atoms to different intensity centers is the key to understand the structure. The step of atom assignment is referred to as

solving the crystal structure. The procedure can be mystifying to the beginner, but is reasonably straightforward. There are two basic procedures for structure solutions, which will be discussed below.

- Known Mineral

  If the sample is a known mineral species, a template of a solved structure of that species may be used for initial atom assignment. This speeds solution, as the major sites can be assigned quickly. Once these have been assigned, the solution can be further manipulated to extract a better agreement between observed (F(obs)) and calculated (F(calc)) data. Typical steps include changing the site occupancy, splitting the site occupancy between two elements, allowing the sites to become anisotropic, and locating hydrogen. As hydrogen is the lightest element, it can be difficult to locate in minerals with significant "heavy" element content. Small changes are made at each step and then run through least-squares cycles, which recalculate the structure using Fourier transformations. Practiced refiners tend to follow the same steps each time.

- Unknown Mineral

  More challenging is when the mineral is unknown or a new species. Here, a template may not be able to be used and elements must instead be assigned based on the geometry of the intensity centers and the chemistry of the material. This procedure can be much more difficult, as it is often through "trial and error" that the correct assignment is found. Once it has, the structure will be further refined as described above.

- Results

  The results of the structure refinement yield a list of atom X-Y-Z assignments in the unit cell, shape of the anisotropic intensity center for each atom (thermal parameters), and the distance of the nearest atomic neighbors. Additionally, the angle between nearest neighbors is also given. The quality of a solution is assessed by the values of *R*1, *wR*2, and GooF.

  - ***R*1**, often called the ***R*-value**, is the agreement between the calculated and observed models. Ideal solutions would have *R*-values of 0, however, due to random errors, this is never achieved. *R*-values (listed as percent) of less than 5% are considered good solutions; high quality samples will often result in *R*-values lower than 2.5%.
  - ***wR*2** is similar to *R*1, but refers to squared *F*-values. These results in *wR*2 always having a higher value than *R*1.
  - The final value, **GooF**, refers to the "goodness of fit" of the solution. In addition to the difference in *F* values, the GooF also takes into account the number of observed reflections and the parameters used. At the end of refinement, the GooF should approach 1.

- Software

  Structure refinement is greatly aided by software packages. Probably the most widely used package of software is the SHELXTL program suite. The different programs in this suite, including XPREP, XP and SHELXL, allow for the initial solution of the phase problem, imaging of the crystal and refinement of the structure.

4.3 Experimental Description

A selected crystal of Ba_2CoO_4 with dimensions of 0.30 × 0.23 × 0.21 mm^3 was mounted on a nylon CryoLoop. The crystal was aligned on a Bruker SMART APEX CCD X-ray diffractometer (see Fig. 4.1) with a digital camera, operated at 50 KV and 30 mA. Intensity measurements were performed using graphite monochromated fine focus Mo $K\alpha$ radiation (λ = 0.7107 Å) from a sealed X-ray tube with a monocapillary collimator. A full sphere of reflections was collected by a combination of three sets of exposure frames. Each set had a different φ angle for the crystal and each exposure covered a range of 0.3° in ω. A total of 1800 frames were collected with an exposure time of 15 s per frame.

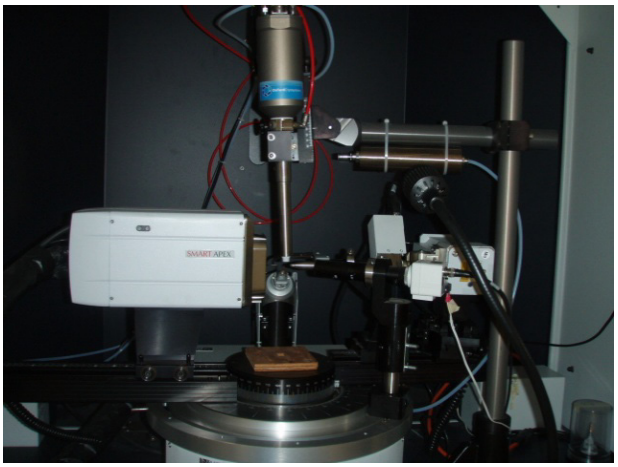

Figure 4.1 Bruker SMART APEX CCD diffractometer.

4.4 Lattice Structure Refinement Results

4.4.1 *Refinement Software*

Determination of integrated intensities and a global cell refinement were performed with the Bruker SAINT (v. 6.02) software package [94] using a narrow-frame integration alogorithm. Using XPREP [95], an analytical face-indexed absorption correction was

applied to the unmerged sets of data. Subsequently, a semiempirical absorption correction was applied using SADABS [96], part of SHELXTL package. The program suite SHELXTL (v. 5.1) was used for space group determination (XPREP), structural solution (XS), and least-squares refinement (XL) [95]. All of the crystals of Ba_2CoO_4 that were examined were found to be twinned along the crystallographic *c* axis. GEMINI was used to separate the twinned components [97]. The final refinement included anisotropic displacement parameters for all atoms and a secondary extinction parameter.

4.4.2 *Lattice Structure of Ba_2CoO_4 and $Ba_{1.5}Sr_{0.5}CoO_4$*

An accurate crystal structure is crucial for discussing the magnetic interactions in solid state compounds. Although the crystal structure of this monoclinic form of Ba_2CoO_4 has been previously reported [74, 93], the refinement was based on powder x-ray data, which often have errors of ± 0.1 Å in metal-oxygen bond lengths because it is difficult to locate oxygen in a heavy-atom background. Furthermore, the published atomic parameters are internally inconsistent with the reported Co- O bond distances [74].

The refined crystallographic cell constants of Ba_2CoO_4 and Sr doped Ba_2CoO_4 ($Ba_{1.5}Sr_{0.5}CoO_4$) from our data set are given in Tables 4.1 for comparison. The atomic positions of each compound are reported in Table 4.2 and Table 4.3, respectively, while the relevant bond distances are shown in Table 4.4 and Table 4.5.

The building blocks of Ba_2CoO_4 are isolated CoO_4 tetrahedra (see Fig. 4.2 and Fig. 4.3). Since the Ba atoms have a closed shell and are not expected to significantly contribute to the electronic and magnetic behavior of this compound, we will not discuss their role in the structure. There is only one crystallographic site for Co atoms in Ba_2CoO_4. As a result, all of the CoO_4 tetrahedra have identical Co-O bond lengths and

angles. There is very little variation in the four Co-O bond lengths (1.79 ± 0.02 Å), although the O-Co-O angles (105° - 113°) deviate somewhat from the ideal tetrahedral value (109.5°). All of the CoO_4 tetrahedral have one face lying flat in the *ac* plane and the opposing vertex pointing along the ±*b* direction. As may be seen in Fig. 4.2 and Fig. 4.3, each Co atom has six nearest Co neighbors, three above in a triangle in the +*b* direction and three below in a triangle in the −*b* direction, with each neighboring Co at a different distance of 4.76 - 5.45 Å. Taken alone, the Co atoms within the structure form an interpenetrating network of trigonal prisms. Each layer of Co atoms in the ac plane has pseudotrigonal symmetry, with very regular Co-Co distances of 5.92 - 6.07 Å.

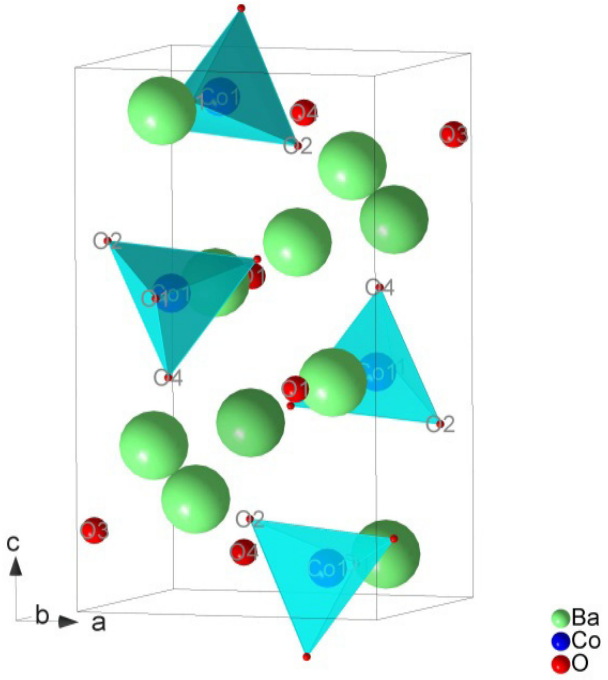

Figure 4.2 The Unit Cell of Ba_2CoO_4.

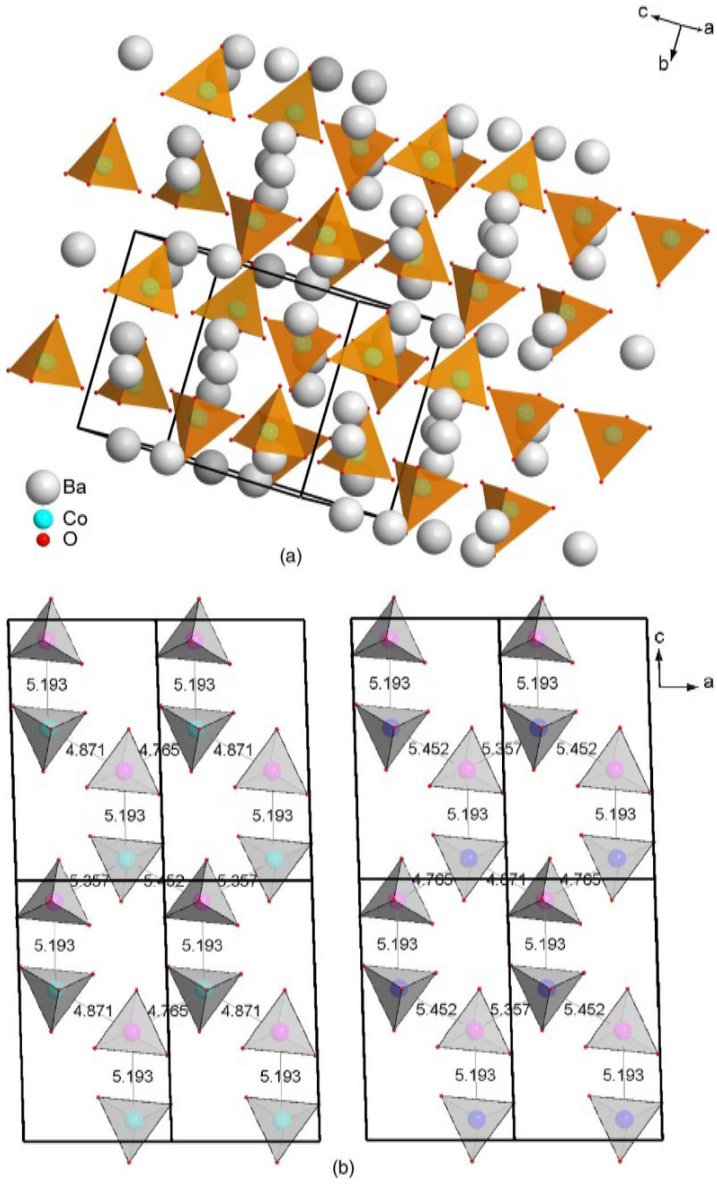

Figure 4.3 Top: crystal structure of Ba_2CoO_4. Bottom: nearest-neighbor network of CoO_4 tetrahedra. Left panel shows distances to the upper plane of neighbors. Right panel shows distances to the lower plane of neighbors. The upper tetrahedron of each vertical pair of tetrahedra (purple) is the same in both panels.

Chemical formula	Ba_2CoO_4	$Ba_{1.5}Sr_{0.5}CoO_4$
Formula weight (g/mol)	397.611	CoO_4
Structure	monoclinic	orthorhombic
Space group	$P2_1/n$ (no. 14)	*Pnma* (no. 62)
a (Å)	5.9176(13)	5.9027(10)
b (Å)	7.6192(16)	7.5334(12)
c (Å)	10.3970(22)	10.2368(16)
α (°)	90	90
β (°)	91.734(4)	90
γ (°)	90	90
Volume ($Å^3$)	468.56(18)	455.20(13)
Th. Density (g/cm^3)	5.636	5.439
*R*1	0.0422	0.0187
*wR*2	0.1193	0.0822

Table 4.1 Crystallographic parameters of Ba_2CoO_4 and $Ba_{1.5}Sr_{0.5}CoO_4$ at room temperature.

Atom	*x*	*y*	*z*	U_{11}	U_{22}	U_{33}	U_{12}	U_{13}	U_{23}
Ba1	0.75661	0.85095	0.08169	0.01483	0.00288	0.01121	-0.00035	-0.00016	-0.00061
Ba2	0.23865	0.49246	0.19004	0.01426	0.00226	0.00599	-0.00033	-0.00073	0.00014
Co	0.74698	0.27584	0.08027	0.01187	0.00052	0.00633	0.00001	-0.00032	0.00006
O1	0.76891	0.50820	0.07991	0.02631	0.00332	0.01554	-0.00040	-0.00041	-0.00007
O2	0.51234	0.20483	0.16954	0.01377	0.01555	0.02541	0.00121	0.00661	0.01284
O3	0.00211	0.17530	0.14193	0.01376	0.00800	0.02017	-0.00252	-0.00181	0.00346
O4	0.70673	0.18445	0.92018	0.02208	0.00465	0.01248	0.00307	0.00071	-0.00113

Table 4.2 Atomic coordinates and anisotropic displacement parameters ($Å^2$) of Ba_2CoO_4.

Atom	Occ	*x*	*y*	*z*	U_{11}	U_{22}	U_{33}	U_{12}	U_{13}	U_{23}
Ba1/Sr1(4c)	0.55(1)	0.75661	0.85095	0.08169	0.01483	0.00288	0.01121	-0.00035	-0.00016	-0.00061
Ba2/Sr2(4c)	0.97(1)	0.3495(1)	0.25	0.5830(1)	0.009(1)	0.019(1)	0.023(1)	0	0	0
Co (4c)	1.0	0.7775(1)	0.25	0.5817(1)	0.008(1)	0.011(1)	0.015(1)	0	-0.001(1)	0
O1 (4c)	1.0	0.0108(8)	0.25	0.5737(6)	0.006(3)	0.094(4)	0.037(3)	0	-0.006(2)	0
O2 (8d)	1.0	0.6966(6)	0.0047(4)	0.6620(3)	0.039(2)	0.015(2)	0.051(2)	0.001(1)	0.016(1)	0.011(1)
O3 (4c)	1.0	0.3214(6)	0.75	0.5799(3)	0.016(3)	0.057(3)	0.021(2)	0	-0.006(1)	0

Table 4.3 Atomic coordinates and anisotropic displacement parameters ($Å^2$) of $Ba_{1.5}Sr_{0.5}CoO_4$.

Table 4.4 Interatomic distances (Å) and angles (°) of Ba_2CoO_4

Bond	Distances (Å)	Bond	Angle (°)
Co-O1	1.775	O1-Co-O2	111.28
Co-O2	1.778	O2-Co-O3	111.46
Co-O3	1.794	O1-Co-O4	112.87
Co-O4	1.813	O2-Co-O3	110.22
		O2-Co-O4	106.23
		O3-Co-O4	104.47

Shortest Co-Co distances (Å)

Co-Co	4.765	Co-Co	5.916
Co-Co	4.871	Co-Co	5.916
Co-Co	5.193	Co-Co	5.918
Co-Co	5.193	Co-Co	5.918
Co-Co	5.357	Co-Co	6.072
Co-Co	5.452	Co-Co	6.072

Table 4.5 Interatomic distances (Å) and angles (°) of Ba_2CoO_4.

Bond	Distances (Å)	Bond	Angle (°)
Co-O1	1.759(6)	O1-Co-O2	111.41(18)
2 × Co-O2	1.773(3)	O2-Co-O2	109.5(2)
Co-O3	1.814(4)	O1-Co-O3	111.6(3)
		O2-Co-O3	106.34(17)

Co-Co distances (nearest neighbors and next nearest neighbor) (Å)

Co-Co (NN)	2 × 4.768(1)	2 × 5.105(1)	2 × 5.384(1)
Co-Co (NNN)	2 × 5.902(1)	2 × 5.923(1)	

The effect of Sr doping on the crystal structure of Ba_2CoO_4 has been also studied by means of X-ray single crystal diffraction. Our measurements indicate that for Sr concentrations up to $x = 0.4$, the structure remains monoclinic with the $P2_1/n$ space group. The unit cell shrinks in all three dimensions as shown in Fig. 4.4, however, no significant change was found in the monoclinic angle β, which remains close to 91.3°. The refinements of fractional occupancies of the Ba/Sr atoms show that there is a strong tendency for Sr atoms to occupy only one of the two unequivalent Ba positions, namely Ba1. It is worth noting that in the parent compound, Ba_2CoO_4, the two distinct Ba sites have the same local symmetry but their oxygen bond distribution is quite different (e.g. Ba1: 2.66 - 2.97 Å and Ba2: 2.61 - 3.18 Å).

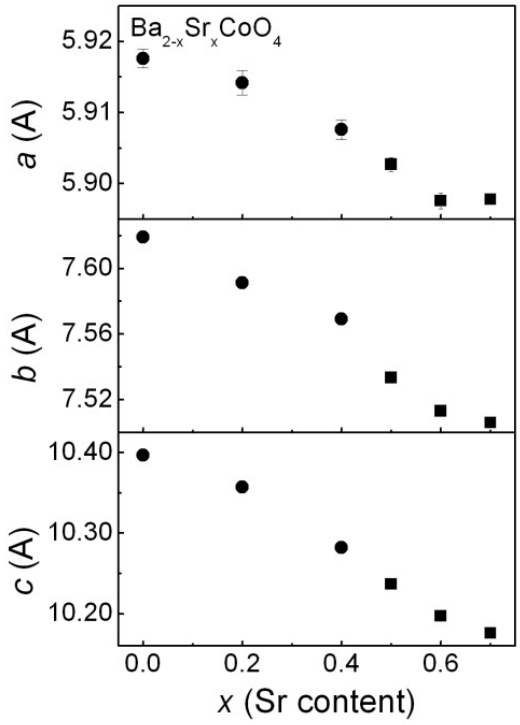

Figure 4.4 The evolution of the lattice parameters as a function of doping level (x) in $Ba_{2-x}Sr_xCoO_4$ ($0 \leq x \leq 0.7$). The circle and square symbols denote the monoclinic and orthorhombic phases, respectively.

Upon increasing the Sr doping level to 0.5, the crystal structure becomes orthorhombic (see Table 4.1). The volume of the unit cell continues to decrease as the system is pushed from monoclinic to orthorhombic. Figure 4.4 displays the dependence of the lattice parameters with the Sr concentration. For $x \geq 0.5$, the space group has been assigned as Pnma (no. 62) based on the inspection of systematic absences. The crystal structure was solved by direct methods using SIR2004 program [98] and the refinements were carried out using SHELXTL software [99].

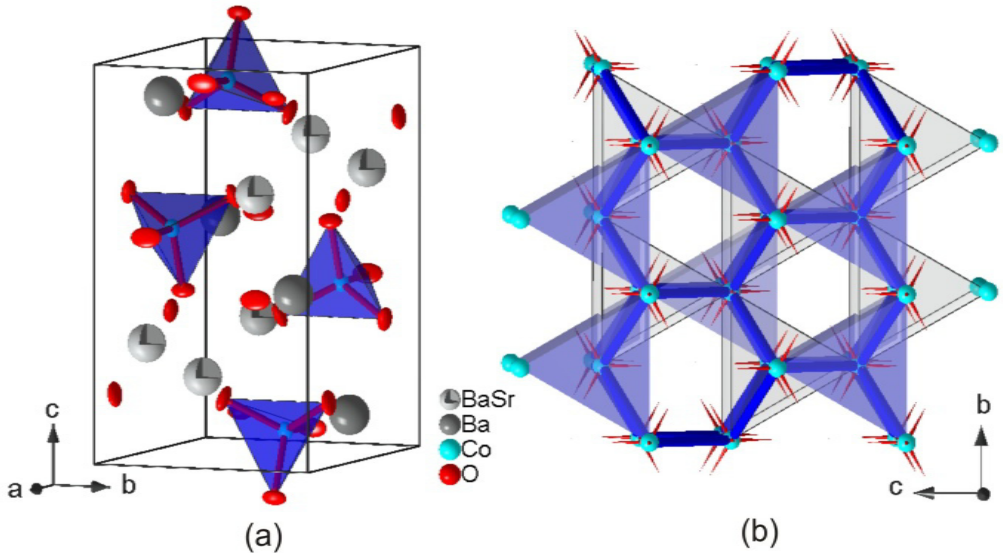

Figure 4.5 (a) The crystal structure of $Ba_{1.5}Sr_{0.5}CoO_4$ with Co ions in a tetrahedral coordination. (b) Magnetic network consisting of interpenetrating trigonal prisms of Co ions ($S = 5/2$).

As a prototype, we illustrate the unit cell structure and interpenetrating trigonal prisms of Co ions network of $Ba_{1.5}Sr_{0.5}CoO_4$ in Fig. 4.5. The refinement results show that, similar to the monoclinic phase, the structure consists of CoO_4 tetrahedra linked by Ba or Sr ions. The four Co-O bond distances in $Ba_{1.5}Sr_{0.5}CoO_4$ have very little variation (1.78 ± 0.03 Å), while the O-Co-O angles (106.3° - 111.6°) slightly deviate from the ideal tetrahedral value (109.5°). The Co ions occupy a single crystallographic site on the

Wyckoff position 4c. Each Co atom is surrounded by six nearest neighbors (NN) located outside the *ac* plane, to form interpenetrating network of trigonal prisms, as depicted in Fig. 4.5(b). In the *ac* plane, each Co ion is screened by six additional next nearest neighbors (NNN) ions. As visible in Table 4.3, the Sr ions continue to preferentially occupy only one of the two available Ba sites.

4.5 Lattice Structure of Pure Sr_2CoO_4

In the chemical formula point of view, Sr_2CoO_4 is isovalent to Ba_2CoO_4. However, their structure and magnetic properties significantly differ from each other, although both Co ions stay in the highest oxidation state. Two forms of Sr_2CoO_4 have been reported recently. Matsuno *et al*. [75, 100] synthesized a single-crystalline film of Sr_2CoO_4 with K_2NiF_4-type tetragonal structure with square-lattice CoO_2 sheets. Polycrystalline samples were prepared by Wang *et al*. at 6 GPa in a high pressure apparatus and heated to 1000 - 1500°C. Structure refinement reveals that Ba_2CoO_4 crystallize in layered 2D tetragonal structure with $a = b = 3.75$ Å, and c = = 12.33 Å [76, 77]. In this section, we will only show the lattice structure of polycrystalline compound from Wang's group.

4.5.1 *Motivation from the study on $La_{1-x}Sr_xCoO_3$*

The Sr doped system of $La_{1-x}Sr_xCoO_3$ has been extensively studied and it is well known that the hole doping affects the spin state of Co^{3+} in a similar way to temperature [101]. Upon the Sr doping, the system changes from non-magnetic insulator to to ferromagnetic metal. For the $x = 0.5$ phase, Goodenough proposed an intermediate-spin model with t_{2g}^5 localized electrons and σ^* itinerant electrons at a density of 0.5 per Co atom [102]. Later, his group proposed a revised model and a detailed temperature-composition (x) phase diagram of the system [101]. The hole doped system may become

further complicated because Co^{4+} ions can also exist in several spin-state configurations like Co^{3+} [103-105].

It is well known that the dimensionality of a system is a key factor governing its electronic structure, and thus, two-dimensional (2D) layered cobalt oxides are quite interesting to compare with the three-dimensional (3D) perovskites. Thus far, various studies have been carried out on K_2NiF_4-type cobalt oxides [53, 106-112], although the number of reports is relatively small compared with the 3D perovskite system. A K_2NiF_4-type oxide consists of CoO_2 planes separated by rock-salt-type planes, and its 2D nature reduces the bandwidth of e_g electrons as compared to the 3D network. This seems a key difference between the two systems. Moritomo *et al*. investigated the K_2NiF_4-type system of $La_{2-x}Sr_xCoO_4$ with a mixed valence of Co^{2+} and Co^{3+} and found steep decreases in the effective magnetic moment, Weiss temperature, and electrical resistivity with x increasing beyond ~ 0.7 [53]. In accordance with these results, they proposed a spin state transition of the Co^{3+} ion from HS to IS. However, Wang *et al*. have reported that the IS state never becomes the ground state of $LaSrCoO_4$ according to their theoretical studies using the unrestricted Hartree-Fock approximation and the real-space recursion method [111, 112].

4.5.2 *Structure Refinement Results*

Figure 4.7 shows the results of Rietveld refinement of the XRD pattern of Sr_2CoO_4 measured at room temperature. The pattern could be indexed when based on a tetragonal unit cell similar to that of Sr_2TiO_4 [113]. Close examination of the diffraction profile revealed the presence of a small amount of SrO_2 in this sample, which was included in the refinement as a second phase. The initial structural model for the

refinement was taken from that of Sr_2TiO_4 [46]. The refined structure of Sr_2TiO_4 was found to be of the K_2NiF_4-type with space group I4/mmm. A schematic representation of the structure of Sr_2CoO_4 is shown in Fig. 4.6. The weight percentage of the impurity phase of SrO_2 in the sample was refined to be 1.2(1) %. As can be seen from Fig. 4.7, the calculated pattern is in excellent agreement with the observed one.

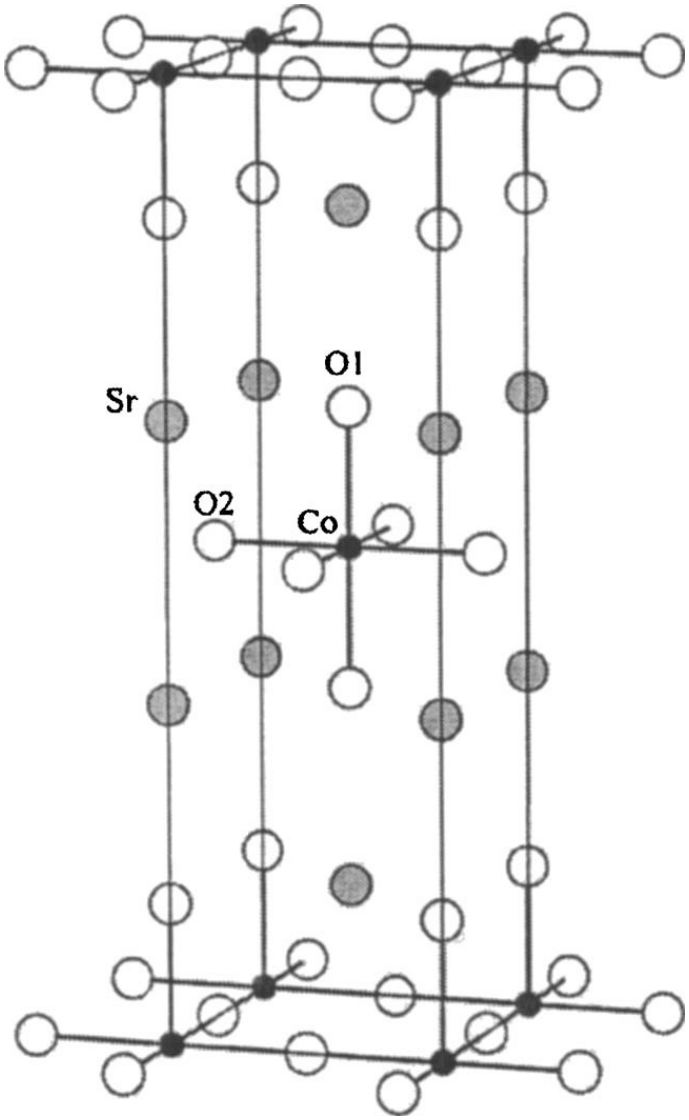

Figure 4.6 Crystal structure of Sr_2CoO_4.

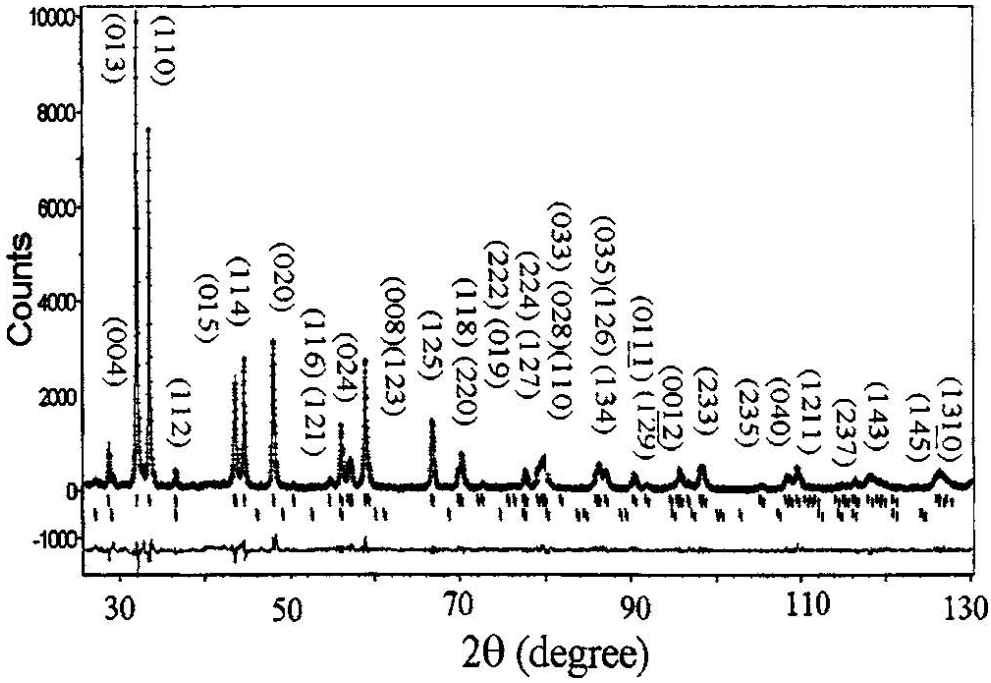

Figure 4.7 The observed (crosses), calculated (solid line), and difference diffraction (bottom solid line) profiles at 300 K for Sr_2CoO_4. The top peak markers relate to Sr_2CoO_4 while the lower peak markers pertain to the impurity SrO_2. All the indexed peaks belong to the Sr_2CoO_4 phase.

4.6 Conclusions

In conclusion, the structures of $Ba_{2-x}Sr_xCoO_4$ have been investigated using X-ray powder and single crystal diffraction at room temperature. Though based on our experimental experiences, not every doping level of $Ba_{2-x}Sr_xCoO_4$ could be reached, and the doping x was able to be pushed as far as $x = 0.7$, we illustrated the typical example refinement results of pure Ba_2CoO_4, $Ba_{1.5}Sr_{0.5}CoO_4$ and Sr_2CoO_4. We can clearly see the structure evolution, which started from monoclinic, to orthorhombic and ended at tetragonal structure.

The nature of the somewhat abrupt structure change from monoclinic to tetrag- onal of the two ending compound Ba_2CoO_4 and Sr_2CoO_4, though the substitution of Sr in place of

Ba only causes the ion size difference, is still unclear. It is hoped that these will stimulate further theoretical work that may solve this riddle.

There are several doping levels of this system ($x > 0.7$) that could not be synthesized. The experiments could be extended further with higher oxygen pressure conventional and optical furnaces.

CHAPTER 5

ELECTRONIC AND MAGNETIC PROPERTIES OF $Ba_{2-x}Sr_xCoO_4$

5.1 Introduction and Motivation

Prior to this thesis, the only reported physical property of Ba_2CoO_4 was magnetic susceptibility χ obtained from polycrystalline [73]. Candela *et al*. [73] found that χ follows a Curie-Weiss law, with no indication of magnetic ordering.

Since we have, for the first time, successfully synthesized a single crystal of Ba_2CoO_4, the measurement of the single crystals become applicable. We measured the magnetic susceptibility of Ba_2CoO_4. Other physical properties, such as specific heat, electrical resistivity and thermal conductivity, will also be shown. Then the doping dependence to the magnetic susceptibility of $Ba_{2-x}Sr_xCoO_4$ will be given.

5.2 Physical Properties of Ba_2CoO_4

5.2.1 *Magnetic Susceptibility*

We measured the magnetic susceptibility of Ba_2CoO_4 single crystals using a commercial superconducting quantum interference device (SQUID) magnetometer from Quantum Design. Because of the geometric limitations imposed by the crystals, the magnetic susceptibility measurement was carried out by applying a magnetic field H either parallel ($H \parallel a$) or perpendicular ($H \perp a$) to the a axis. There are no structural reasons to expect greatly divergent behaviors in the b and c directions. Shown in Fig. 5.1 is χ versus T between 2 and 350 K measured by applying $H = 0.1$ T parallel (unfilled circles) and perpendicular (filled circles) to the a axis. In either direction, the susceptibility measured in both zero-field and field cooling shows no hysteresis. In addition to the Curie-Weiss-like behavior at high temperatures, both $\chi(H \parallel a)$ and $\chi(H \perp a)$ decrease with decreasing temperature after reaching a maximum at $T_N = 25$ K. While they are almost identical above T_N, a large anisotropy develops below T_N as

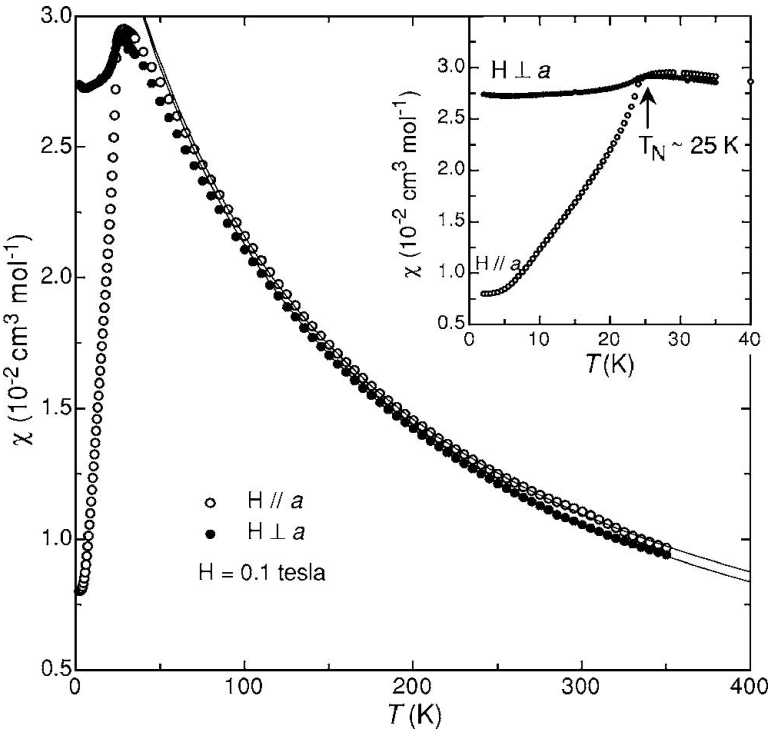

Figure 5.1 Temperature dependence of the magnetic susceptibility χ obtained by applying H = 0.1 T either parallel (unfilled circles) or perpendicular (filled circles) to the a direction. The solid lines are the fit of experimental data between 150 and 350 K to Eq. 5.2.1. The magnetic susceptibility reaches a maximum at T_N = 25 K as shown in the inset.

clearly seen in the inset. The change in χ below T_N is almost exactly what is expected from a mean-field calculation for an antiferromagnetic system with the spins along the a axis [19]. In this case, the Curie-Weiss temperature θ should be negative if $\chi(H \parallel a)$ and $\chi(H \perp a)$ are described using

$$\chi = \chi_0 + \frac{N_A \mu_B^2 g^2 S(S+1)}{3k_B} \frac{1}{T-\theta} \qquad T > T_N. \tag{5.2.1}$$

Here χ_0 is a constant describing temperature-independent paramagnetism, N_A is Avogadro's number, k_B is the Boltzmann constant, μ_B is the Bohr magneton, S is the total spin, and g = 2 assuming that the orbital angular momentum is quenched [114].

Our fits to the magnetic susceptibility curves for the range $150 \leq T \leq 350$ K (solid lines in Fig. 5.1) give $\chi_0 = -2.3 \times 10^{-4}$ cm^3/mol, $S = 2.56$, and $\theta = -109$ K from $\chi(H \parallel a)$, and $\chi_0 = -7.7 \times 10^{-4}$ cm^3/mol, $S = 2.60$, and $\theta = -112$ K from $\chi(H \perp a)$. The high spin value confirms that Ba_2CoO_4 has the stoichiometric Co^{4+} (d^5) ion at a tetrahedral site, where the small crystal-field splitting results in degenerate d orbitals thus giving a total spin of $S = 5/2$. The negative θ value confirms antiferromagnetic spin interactions along both the a and b - c directions. It is worth noting that this value of θ is significantly larger than T_N, suggesting either a reduced-dimensional magnetic interaction [115] and/or the existence of magnetic frustration [116].

From a structural point of view, it is not obvious that there exists geometric frustration. On the other hand, we note that $\chi(H \parallel a) \neq 0$ when $T \rightarrow 0$ K (see Fig. 5.1), that suggests that a small portion of spins are not aligned in an ideal AFM configuration. This could be the result of spin canting and/or defects in the single crystal. With a direct determination of the magnetic structure by neutron powder diffraction, it should be clear whether the spins are canted or not, although the magnetization varies linearly with H up to at least 7 T at temperatures below T_N (not shown). We will discuss the magnetic structure later in Chapter 6. However, the defect scenario is supported by the specific heat and transport data presented later. In an AFM system, a defect can lead to a single frustrated bond [116]. Associated with this configuration, there are multiple equal-energy configurations that grow with the number of defects [116]. To gain insight into the nature of the magnetic transition, we further measured the specific heat, electrical, resistivity, and thermal conductivity of Ba_2CoO_4 using a physical property measurement system (PPMS) from Quantum Design.

5.2.2 *Specific Heat*

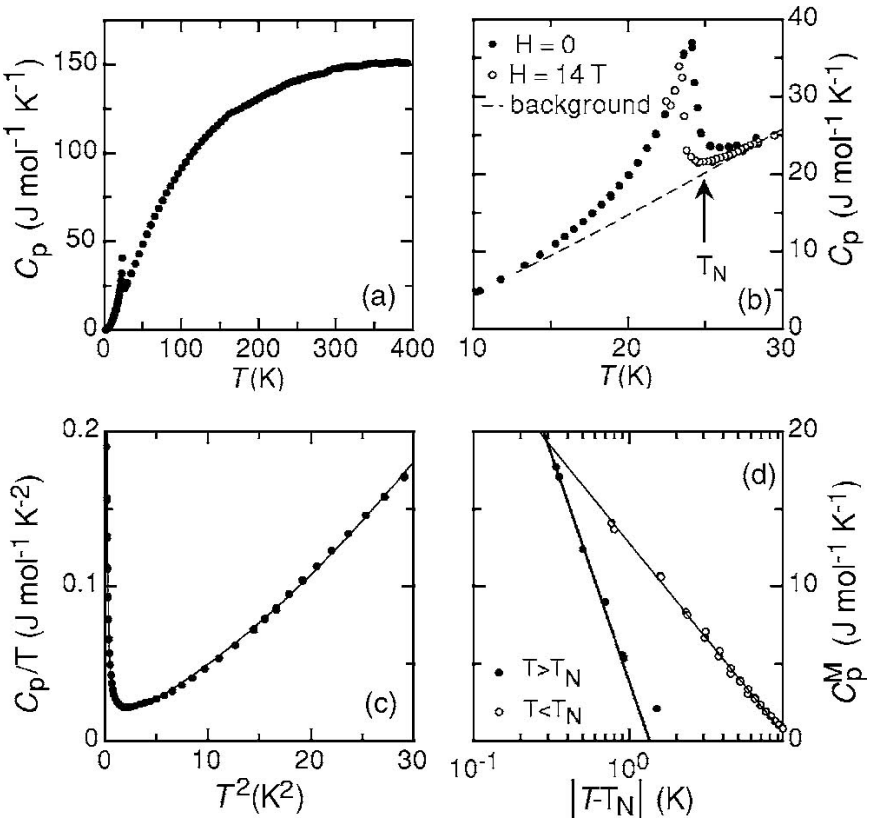

Figure 5.2 (a) Temperature dependence of the specific heat C_p between 0.4 and 400 K. Note that there is a specific heat jump at T_N that has little field dependence as emphasized in (b). The broken line represents the polynomial fit of specific heat data away from the transition regime (see the text). Shown in (c) are the low-temperature specific heat data plotted as C_p/T versus T^2. The solid line is the fit of data to Eq. 5.2.2. The temperature dependence of the magnetic specific heat C_p^M near T_N is plotted in (d) in a semilogarithmic scale. The solid lines are the fit of experimental data to Eq. 5.2.3.

Shown in Fig. 5.2(a) is the temperature dependence of the specific heat C_p between 0.4 K and 400 K. Note that it reveals a sharp peak at T_N. The term C_p, measured by both cooling and warming, reveals no hysteresis, so the phase transition is likely of second order. Remarkably, there is little change under the application of a 14 T magnetic field as demonstrated in Fig. 5.2(b). This indicates that the transition at T_N is unlikely the result of spin-density-wave formation, but is consistent with long-range AFM ordering. In this

case, the magnetic entropy removed upon ordering is expected to be $S_M = R\ln(2S + 1) = 14.9$ J/mol K, where $R = 8.314$ J/mol K. To estimate the entropy change associated with the magnetic phase transition at T_N, the electronic and phonon background has to be subtracted. At low temperatures ($T \ll \theta_D$, the Debye temperature), the specific heat from itinerant electrons and acoustic phonons can be described by $C_p = \gamma T + N(12/5)\pi^4\theta^{-3}T^3$, where γ is the Sommerfeld coefficient and $N = 7$ for Ba_2CoO_4. The T term describes the electronic contribution and the T^3 term arises from the phonon contribution. Shown in Fig. 5.2(c) is our specific heat data below ~ 5 K plotted as C_p/T vs T^2. Note that C_p/T varies nonlinearly with T^2 and reveals an upturn at very low temperatures. This indicates that, in addition to the above-mentioned terms, the specific heat consists of magnetic contributions from spin waves and the nuclear Schottky effect [117], i.e.,

$$C_p/T = \gamma + \frac{12N\pi^4R}{5\theta_D^3}T^2 + C_M T^2 e^{-\Delta_M/T} + \alpha\frac{e^{\Delta_{sch}/T}}{T^3(1+e^{\Delta_{sch}/T})^2}. \qquad (5.2.2)$$

The third term describes the spin-wave contribution with Δ_M being a magnon gap and C_M a constant. The fourth term describes the nuclear Schottky effect with α being a constant proportional to the number of two-level systems and Δ_{sch} the energy separation between the two levels. The solid curve shown in Fig. 5.2(c) is the fit of experimental data between 0.4 and 5 K to Eq. 5.2.2. This yields $\gamma = 11.4$ mJ/mol K^2, $\theta_D = 176.5$ K, $C_M = 11.8$ mJ/mol K4, $\Delta_M = 7.2$ K, $\alpha = 58.0$ mJ K/mol, and $\Delta_{sch} = 0.01$ K. The successful fitting of low-temperature specific heat data to Eq. 5.2.2 usually suggests that the phonon contribution can be described by the Debye model. Surprisingly, there is a great discrepancy between our data and the model calculation at high temperatures, when using the θ_D value given above. This implies that either the phonon specific heat

of Ba_2CoO_4 does not simply increase in a Debye-model-like fashion or the θ_D value obtained from the above fitting procedure is not very reliable due to the large number of fitting parameters. If we use the room-temperature anisotropic displacement parameters given in Table 4.2, $\theta_D \sim 327$ K is obtained [118]. It seems inappropriate to treat θ_D as a temperature-independent constant when using the Debye expression to describe the phonon specific heat of Ba_2CoO_4 in a wide temperature range.

Given the situation described above, we subtract the background by fitting the experimental data at $5 \leq T \leq 10$ K and $30 \leq T \leq 50$ K using a polynomial [see the dashed line in Fig. 5.2(b)]. This yields the magnetic entropy change $\Delta S = 3.38$ J/mol K near T_N, much smaller than $S_M = 14.9$ J/mol K. This implies that most of the entropy is removed above T_N. As may be noted in Fig. 5.1, the magnetic susceptibility deviates from its high-temperature behavior below ~ 150 K, indicating the development of short-range magnetic correlations. Nevertheless, the excess magnetic specific heat C_p^M near T_N is presented in Fig. 5.2(d) above (filled circles) and below (unfilled circles) T_N. Interestingly, C_p^M, for either $T > T_N$ or $T < T_N$, falls more or less on a straight line when plotted as a function of $| T - T_N |$ in a semilogarithmic scale. This indicates that the magnetic specific heat diverges logarithmically as for a λ-type transition, i.e.,

$$C_p^M = \begin{cases} A_1 \ln(T - T_N) + A_2, \\ B_1 \ln(T_N - T) + B_2, \end{cases} \tag{5.2.3}$$

where A_1, A_2, B_1, and B_2 are constants. The solid lines in Fig. 5.2(d) represent Eq. 5.2.3.

5.2.3 *Electrical Resistivity*

Considering the nonzero γ value, one may naively expect the system to be electrically conductive. Shown in Fig. 5.3(a) is the temperature dependence of the electrical

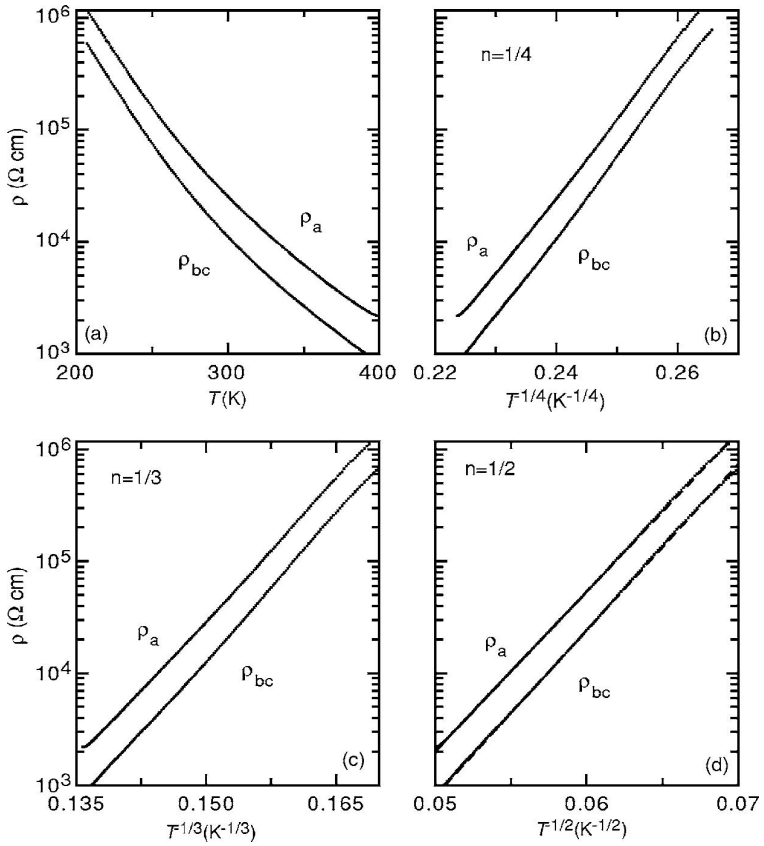

Figure 5.3 Temperature dependence of the electrical resistivities ρ_a and ρ_{bc} between 200 and 400 K (a). The data are replotted as $\rho_{a,bc}$ versus T^{-n} with n = 1/4 (b), 1/3 (c), and 1/2 (d). The broken lines in (d) are the fit of experimental data to Eq. 5.2.4 using n = 1/2.

resistivity along both the *a* (ρ_a) and the *bc* (ρ_{bc}) directions. It is surprising that both ρ_a and ρ_{bc} are large and increase with decreasing temperature. Below about 170 K, the system becomes too resistive to measure with our apparatus. In the temperature range between 200 and 400 K, little magnetoresistance is seen when applying a magnetic field up to 14 T (data not shown). On the other hand, both ρ_a and ρ_{bc} reflect characteristics of a localized electronic state. In this case, the electrical resistivity is expected to follow Mott's variable-range-hopping formula [119]

$$\rho = \rho_0 \exp\left(\frac{T_0}{T}\right)^n, \tag{5.2.4}$$

where ρ_0 and T_0 are constants, and n = 1/2, 1/3, 1/4, depending on the dimensionality D and temperature range. This means that logρ varies linearly with T^{n}. For comparison, we replot resistivity data as log $\rho_{a,bc}$ vs T^{n} with n = 1/4 for D = 3 without a Coulomb gap [Fig. 5.3(b)], 1/3 for D = 2 [Fig. 5.3(c)], and 1/2 for D = 1 or 3 with a Coulomb gap [119] [Fig. 5.3(d)]. Note that the data have better agreement with Eq. 5.2.4 when n = 1/2, (errors as determined by χ^2 are 0.10 for n = 1/2, 0.44 for n = 1/3, 0.81 for n = 1/4). By fitting data between 200 and 400 K to Eq. 5.2.4 using n = 1/2, we obtain $\rho_0 = 1.5 \times 10^{-4}\Omega\,\mathrm{cm}$ and $T_0 = 1.1 \times 10^5\mathrm{K}$ from ρ_a and $\rho_0 = 3.1 \times 10^{-5}\Omega\,\mathrm{cm}$ and $T_0 = 1.2 \times 10^5\mathrm{K}$ from ρ_{bc}. The broken lines in Fig. 5.3(d) are the fitting results-that completely overlap with the experimental data. This suggests that the electrical conduction is either one- or three-dimensional-like with strong Coulomb repulsion between carriers [119]. Given the fact that both ρ_a and ρ_{bc} behave similarly, the latter may be more plausible.

5.2.4 *Thermal Conductivity*

The fact that the electrical resistivity can be described by the variable-range-hopping model confirms the presence of disorder in our crystal samples, which is likely introduced by defects and/or twinning. Microscopically, the defects can be viewed as interstitial or substitutional impurity atoms that can move (tunnel) in a multi-minima potential provided by the neighbors. In this case, the nonzero γ value no longer reflects the finite density of states at the Fermi level as in a metal, but rather the density of tunneling states [120]. In this scenario, the thermal conductivity is expected to be proportional to T^2 at low temperatures [120]. Shown in Fig. 5.4(a) is the temperature dependence of the thermal conductivity κ_{bc} measured by applying the temperature gradient (heat flow) along the bc direction. Qualitatively, κ_{bc}, above T_N, behaves as expected for a typical

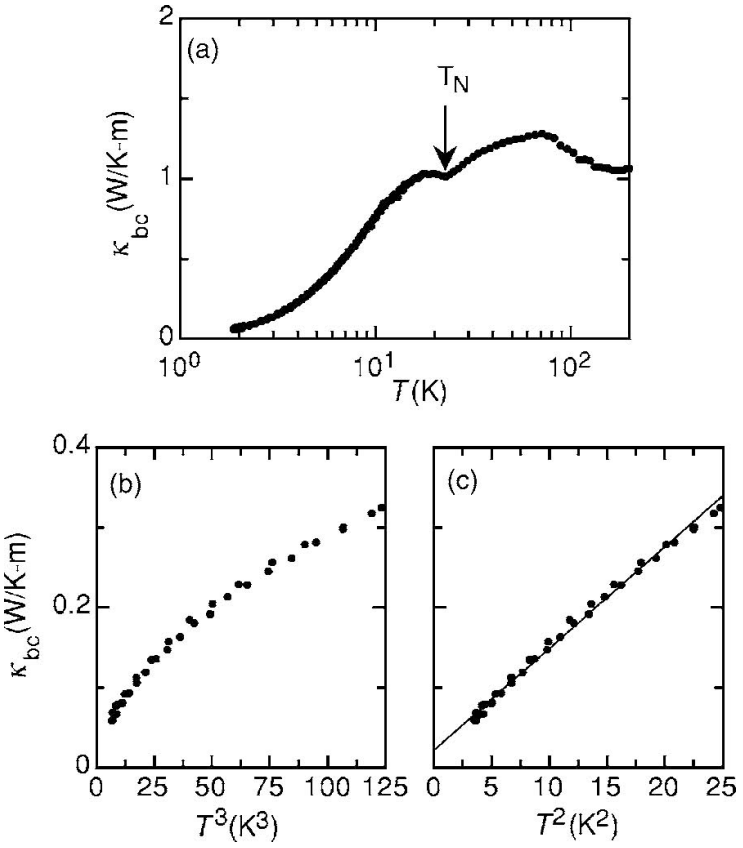

Figure 5.4 (a) Temperature dependence of the thermal conductivity between 1.8 and 200 K obtained by applying heat current along the *bc* direction and plotted in semilogarithmic scale. Data below 5 K are replotted as κ_{bc} vs T^3 (b) and κ_{bc} vs T^2 (c), respectively. The solid line in (c) is a guide to the eyes.

insulating crystal-with decreasing temperature, it initially increases then decreases after the phonon mean free path reaches a maximum. Remarkably, κ_{bc} increases as the system is cooled below T_N, indicating that the thermal scattering due to spins is reduced. As less than 1/3 of magnetic entropy is removed near T_N, the scattering reduction is not dramatic. When the temperature is further lowered, κ_{bc} decreases again with decreasing temperature due to dominant nonmagnetic contributions. In a perfect insulating crystal, the thermal conductivity varies with T in the same manner as the phonon specific heat at low temperatures, i.e., both proportional to T^3. As may be seen in Fig. 5.4(b), κ_{bc} vs T^3 is

not linear, even over a small temperature range. However, this set of data falls more or less on a straight line when plotted as κ_{bc} vs T^2 as shown in Fig. 5.4(c), confirming that the thermal conductivity is mainly governed by phonon-defect scattering below ~ 5 K.

5.3 Doping Dependence of $Ba_{2-x}Sr_xCoO_4$ ($0 \leq x \leq 0.7$) including Phase Diagram

Since the parent compound Ba_2CoO_4 behaves as an insulator at all temperature regime, we will only discuss the doping dependence of magnetic susceptibilities.

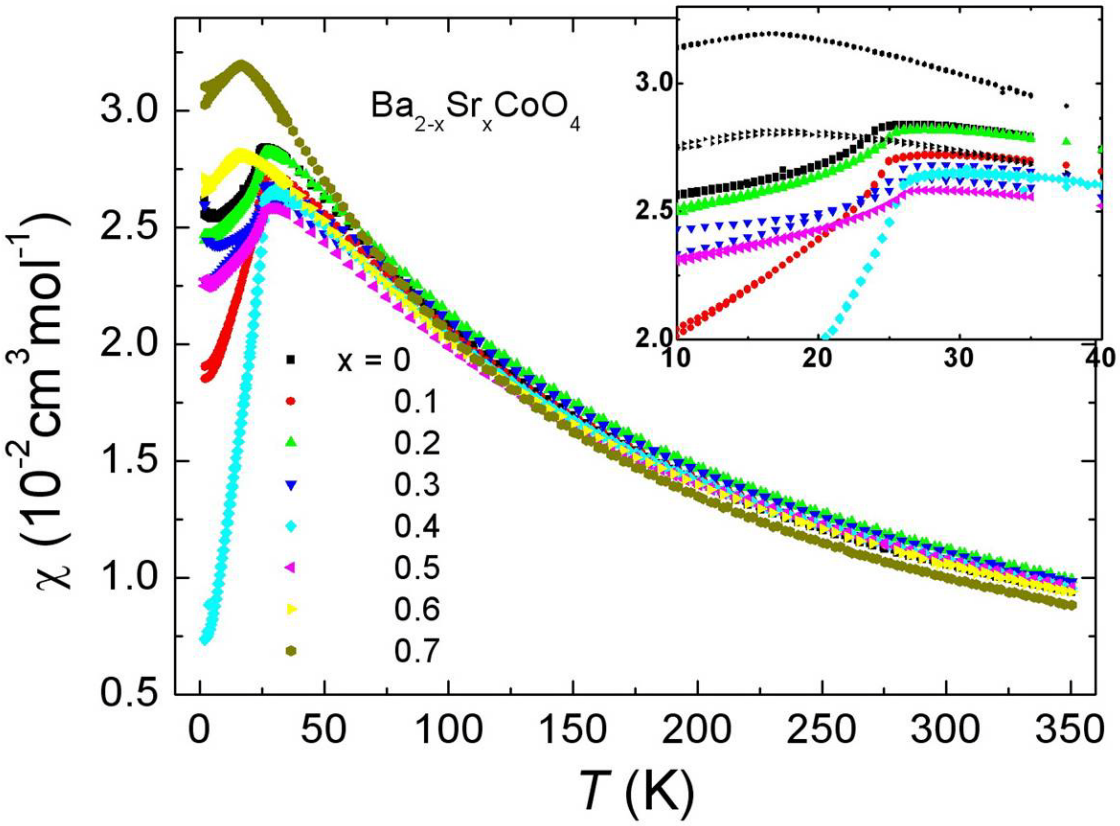

Figure 5.5 Temperature dependence of magnetic susceptibility χ obtained by applying H = 0.1 T on $Ba_{2-x}Sr_xCoO_4$ ($0 \leq x \leq 0.7$). The solid line is the fit of experimental data of $Ba_{1.3}Sr_{0.7}CoO_4$ between 150 and 350 K according to Eq. 5.2.1.

The magnetic susceptibilities of $Ba_{2-x}Sr_xCoO_4$ were measured with powders crushed from selected single crystals. Figure 5.5 demonstrates the susceptibility χ versus T

between 2 K and 350 K measured by applying $H = 0.1$ T. The data collected in both zero-field and field cooling show no hysteresis. The value χ for each sample decreases with decreasing the temperature after reaching a maximum at T_N, which indicates an antiferromagnetic transition for all doping concentrations. The doping dependence of T_N is shown in Fig. 5.6. Note that the Néel temperature T_N slightly increases in the monoclinic regime from $T_N = 25$ K up to $x = 0.5$, then it decreases while the structure becomes orthorhombic. It is also worth noting that each sample exhibits more or less residue magnetic moment when approaching the base temperature.

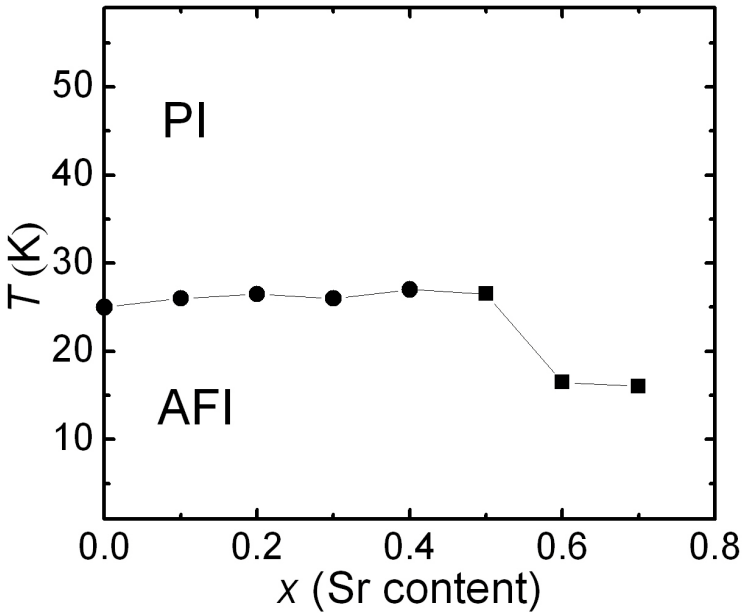

Figure 5.6 Phase diagram of $Ba_{2-x}Sr_xCoO_4$ ($0 \leq x \leq 0.7$). The circles and squares represent the monoclinic and orthorhombic structures, respectively.

On the other hand, the behaviors of χ vs T for all the samples are similar when $T > T_N$, which is also well defined by Curie-Weiss law at high temperatures, according to Eq.

5.2.1. Our fitting range is fixed as $150 \leq T \leq 350$ K. The solid line in Fig. 5.5 shows an example of Curie-Weiss fitting for $Ba_{1.3}Sr_{0.7}CoO_4$ sample. As shown in Fig. 5.7(a), the Curie-Weiss temperatures of all doing concentrations are negative, which confirms the antiferromagnetic spin interactions. The values of $|\theta|$ are all significantly larger than T_N, which is similar to the undoped case. As can be seen from Fig. 5.7(b), the effective spins S_{eff} of Co atoms of all the samples are around 2.5, implying the highest oxidation states of Co^{4+} (d^5) ions at a tetrahedral site.

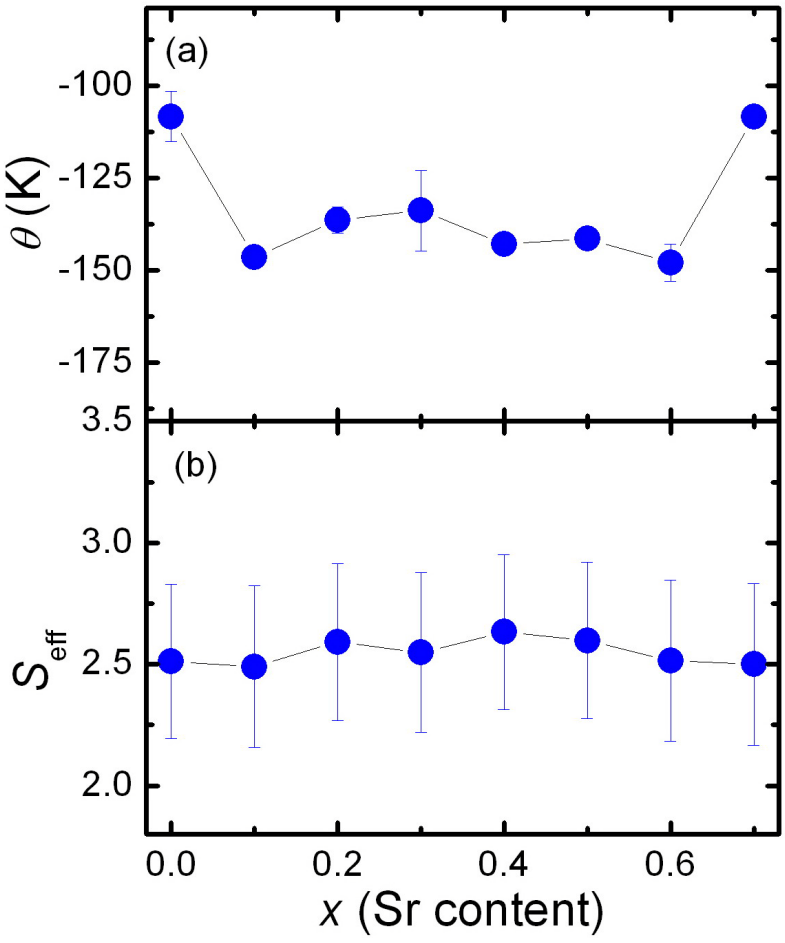

Figure 5.7 The fitting results of (a) Curie-Weiss temperatures, and (b) effective spin values of all doping concentration samples of $Ba_{2-x}Sr_xCoO_4$ ($0 \leq x \leq 0.7$).

5.4 Conclusions

The physical properties of Ba_2CoO_4 have been thoroughly investigated. The compound becomes magnetically ordered at T_N = 25 K as shown in the temperature dependence of both magnetic susceptibility and specific heat. The magnetic susceptibilities of $Ba_{2-x}Sr_xCoO_4$ show AF interaction for all doping concentrations above T_N. T_N shows little doping dependence when the system remains monoclinic and it decreases when the system enters orthorhombic regime.

CHAPTER 6

MAGNETIC STRUCTURE AND EXCITATIONS OF Ba_2CoO_4

6.1 Introduction and Motivation

The compound of Ba_2CoO_4 is isostructural to Ba_2TiO_4 [121], a distorted form of the orthorhombic K_2SO_4 structure type, shows cobalt ions only in the tetrahedral environment whereas they are octahedrally coordinated in the 2H structure. The Co^{4+} cation also confers remarkable properties to another (214) material recently studied: Sr_2CoO_4. This oxide, isostructural to the K_2NiF_4 type with corner-sharing CoO_6 octahedra, exhibits a ferromagnetic transition with a rather high Curie temperature as well as metallic behavior [75] and large negative magnetoresistance [76]. It must be pointed out that there are few materials with all cobalt atoms in the Co^{4+} state at a tetrahedral site. One of the few reported oxides (together with Li_4CoO_4) [122] is Ba_2CoO_4. In both cases, despite such a particular feature, its magnetic structures have not been widely studied. This chapter is focused on the determination of the magnetic structures of Ba_2CoO_4 using neutron diffraction at different temperatures.

6.1.1 *Experimental Description*

Neutron single crystal diffraction data of magnetic excitations were collected at the NIST Center for Neutron Research on the triple-axis spectrometer (BT7) with monochromatic neutrons of wavelength 2.3589 Å produced by a PG(002) monochromator. The temperature was changed sequentially from 9 K to 300 K. Neutron powder diffraction data were collected on the high resolution powder neutron diffractometer (BT1) with monochromatic neutrons of wavelength 1.5403 Å produced by a Cu(311) monochromator for the measurements of magnetic structure. Collimators with horizontal divergences of 15', 20' and 7' of arc were used before and after the monochromator and after the sample, respectively. Data were collected in the 2θ range of $3 - 168°$ with a step

size of 0.05° at 4 K, 33 K and room temperature. The magnetic structural parameters were refined using the program GSAS.

6.2 Magnetic Structure

6.2.1 *Neutron Powder Diffraction Results*

The good agreement between the observed and calculated neutron powder diffraction (NPD) patterns of Ba_2CoO_4 at $T = 4$ K is presented in Fig. 6.1. The patterns obtained below the Néel temperature show the presence of low-angle additional peaks of magnetic origin. As the temperature decreases, the intensities of the magnetic peaks increase until nearly achieving saturation.

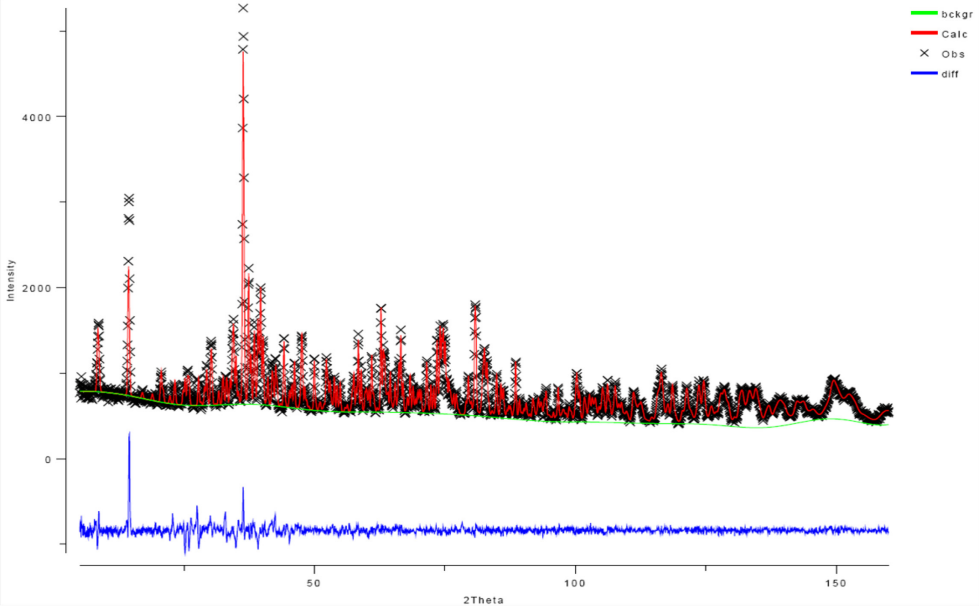

Figure 6.1 Neutron powder diffraction pattern including fitting result for Ba_2CoO_4 measured at 4 K (below T_N).

6.2.2 *Magnetic Structure*

The magnetic reflections in NPD can be indexed by using the propagation vector **k** = (0.5, 0, 0.5), so the magnetic cell is doubled along the *a* and *c* axes with respect to the crystallographic cell.

To determine the magnetic structure, symmetry analysis for the space group $P2_1/n$ with the propagation vector **k** = (0.5, 0, 0.5) has been performed for the 4e position, occupied by the Co atoms in tetrahedral coordination. The output of the analysis is the complete set of basis functions of the irreducible representations classifying the possible magnetic ordering models, which is summarized in Table 6.1[9]. Four one-dimensional real representations have been obtained. The notation for the atomic positions of the Co atoms are: Co(1) (x, y, z), Co(2) (-x + 1/2, y + 1/2, -z + 1/2), Co(3) (-x, -y, -z), and Co(4) (x + 1/2, -y + 1/2, z + 1/2).

Irreducible representation		basis function vectors			
		Co(1)	Co(2)	Co(3)	Co(4)
Γ_1(++++)	$A_xC_yA_z$	(1 0 0)	(-1 0 0)	(-1 0 0)	(1 0 0)
		(0 1 0)	(0 1 0)	(0 -1 0)	(0 -1 0)
		(0 0 1)	(0 0 -1)	(0 0 -1)	(0 0 1)
Γ_2(++++)	$G_xF_yG_z$	(1 0 0)	(-1 0 0)	(1 0 0)	(-1 0 0)
		(0 1 0)	(0 1 0)	(0 1 0)	(0 1 0)
		(0 0 1)	(0 0 -1)	(0 0 1)	(0 0 -1)
Γ_3(++++)	$C_xA_yC_z$	(1 0 0)	(1 0 0)	(-1 0 0)	(-1 0 0)
		(0 1 0)	(0 -1 0)	(0 -1 0)	(0 1 0)
		(0 0 1)	(0 0 1)	(0 0 -1)	(0 0 -1)
Γ_4(++++)	$F_xG_yF_z$	(1 0 0)	(1 0 0)	(1 0 0)	(1 0 0)
		(0 1 0)	(0 -1 0)	(0 1 0)	(0 -1 0)
		(0 0 1)	(0 0 1)	(0 0 1)	(0 0 1)

Table 6.1 Irreducible representations and basis functions of the space group $P2_1/n$ for the Wickoff position 4e and propagation vector **k** = (0.5, 0, 0.5).

[9] The characters (+ for 1, - for -1) of each symmetry operator are given in parentheses. The list corresponds to the following ordering of the symmetry operators, in Seitz notation: {1|000}, {2_0y0|PPP}, {-1|000}, {m_x0z|ppp}, with p = 1/2.

After checking all of the possible magnetic modes obtained, the best agreement with the experimental data was obtained for the magnetic structure given by the basis vectors of the irreducible representation. This means that the magnetic moments become ordered with a spin arrangement. The A_x basis vector implies that the coupling among the magnetic moments is $m_{1x} - m_{2x} - m_{3x} + m_{4x}$ (similarly for A_z), and the C_y basis vector implies that the y components are related by $m_{1y} + m_{2y} - m_{3y} - m_{4y}$.

The magnetic structure of Ba_2CoO_4 determined from the neutron diffraction data has been represented in Fig. 6.2 and Fig 6.3 (in 3D). We clearly see a relatively straightforward AF structure in the *ac*-plane in this compound. This interaction is lacking along the *c* axis.

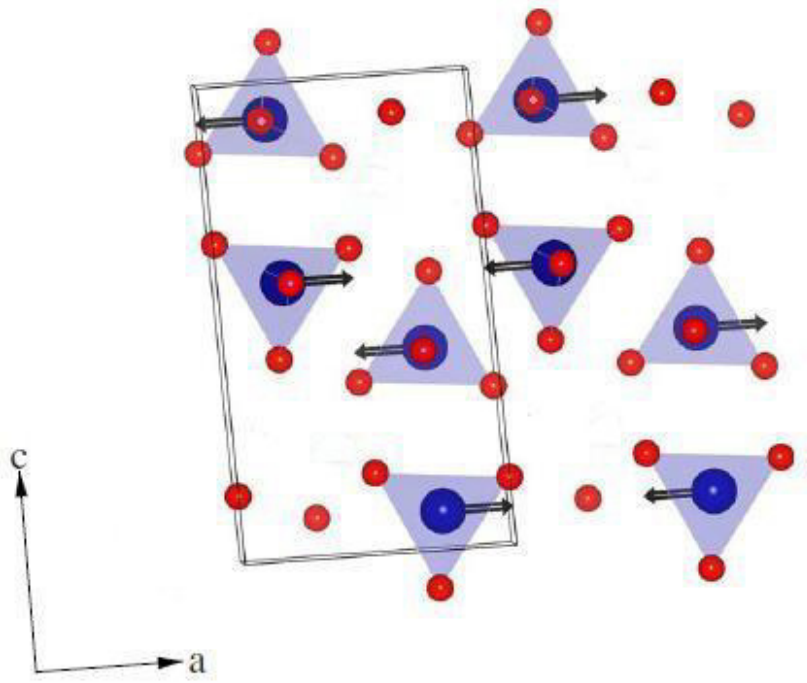

Figure 6.2 Magnetic structure of Ba_2CoO_4 at 4 K along *b* axis. Though the magnetic cell is twice the length of the unit cell in both the *a* and *c* directions, only the lower half of the magnetic unit cell is shown, so that the spins can be clearly seen. The CoO_4 tetrahedra are displayed with the Co atoms in blue and the O atoms in red. Each tetrahedron is shaded to help show the crystal structure.

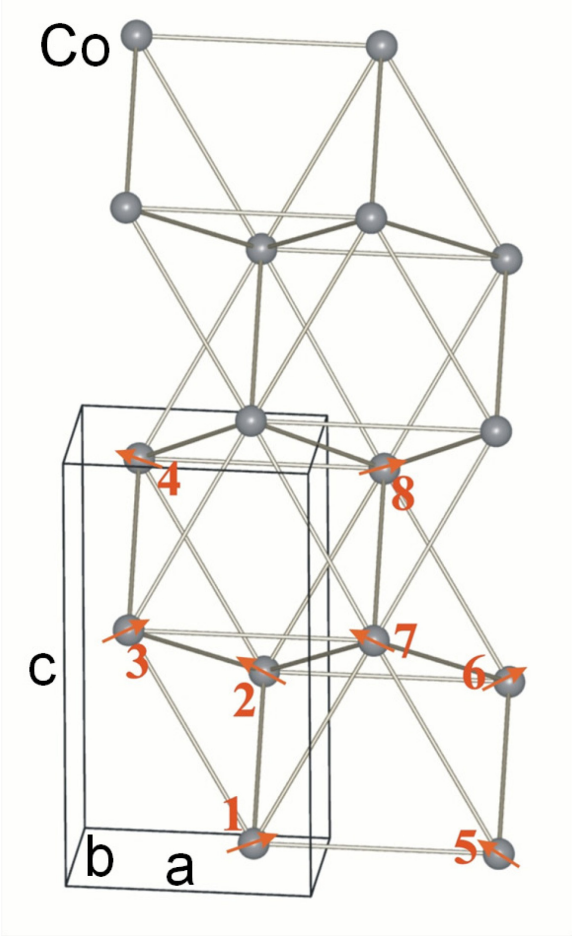

Figure 6.3 3D view of the magnetic structure of Ba_2CoO_4 at 4 K.

6.3 Magnetic Excitations

6.3.1 *Magnetic Order Parameters*

We first utilized TAS to double confirm the AF transition temperature $T_N = 25$ K. The magnetic Bragg peaks were measured at the reciprocal propagation vector position (-0.5, 0, 1.5) in the reciprocal space which gives AF order. The scan was performed along the transverse direction to avoid the affects from the structure factor. The data are represented in two 2D mapping diagrams (see Fig. 6.4) for both warming and cooling

processes, respectively. The temperature range of cooling and warming is from 8 K to 35 K which is around the Néel temperature.

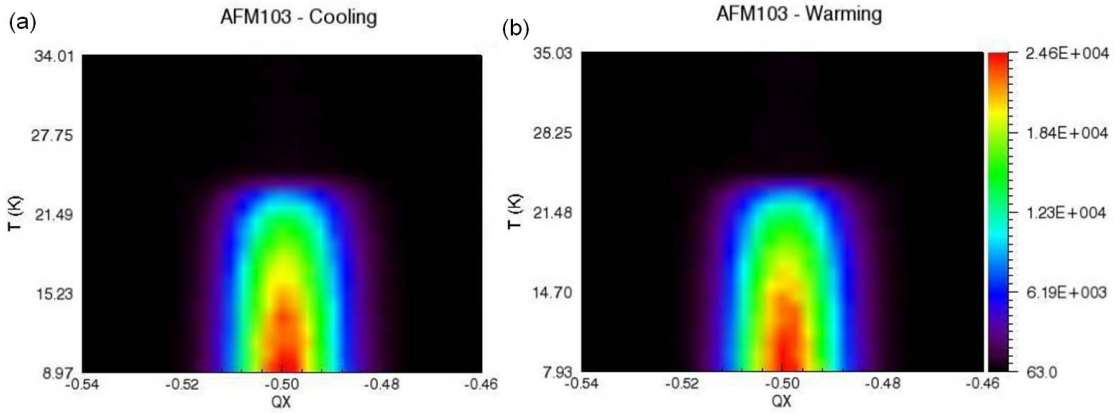

Figure 6.4 2D mapping diagrams of the magnetic Bragg peaks at (-0.5, 0, 1.5) as a function of temperature of Ba_2CoO_4 in (a) cooling and (b) warming.

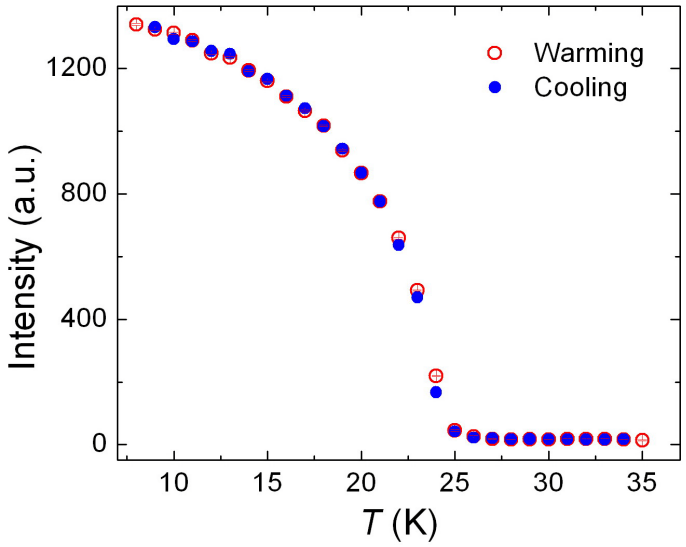

Figure 6.5 Magnetic Bragg peak intensities at (-0.5, 0, 1.5) as a function of temperature of Ba_2CoO_4 shown in cooling (blue solid circle) and warming (red open circle).

Very clearly, the AF peaks begin to arise when the temperature is decreasing below 25 K which confirms our magnetic susceptibility measurements that the AF transition at $T_N = 25$ K.

The magnetic Bragg peak intensities were also calculated by fitting as a Gaussian function. As seen in Fig. 6.5, the AF transition starts at Néel temperature T_N = 25 K. The measurements from cooling and warming show no thermal hysteresis.

6.3.2 *Lattice Constants*

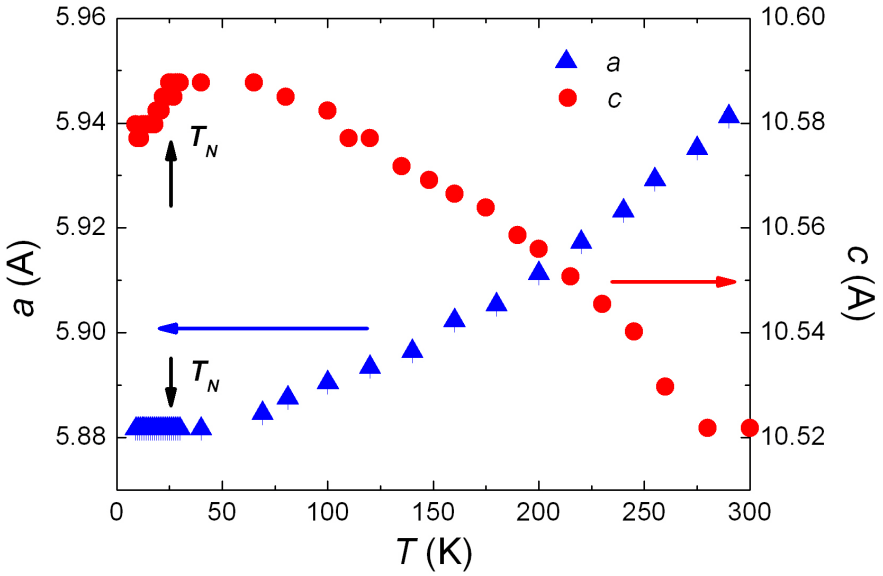

Figure 6.6 Lattice constants of *a* (blue triangle) and *c* (red circle) measured as a function of temperature.

The magnetic susceptibility measurements have showed that Ba_2CoO_4 has an anti-ferromagnetic (AF) transition at a Néel temperature of T_N = 25 K [123]. However, there is no associated structural transition from room temperature to 4 K [124]. We measured the temperature dependence of lattice constants (*a* and *c*) in the scat- tering plane. The temperature range is from 9 K to 300 K (see Fig. 6.6). As the temperature increases, the lattice constant of *a* keeps constant below T_N and begins to increase right above T_N. However, the lattice constant of *c* first slightly increases as the temperature increases below T_N and then decreases above T_N. A magnetoelastic effect is clear due to the

opposite thermal expansion behavior along the *c*-axis when the system undergoes the AF transition at T_N. Although the monoclinic structure maintains at the whole temperature range, there may implicitly still be certain correlations between the lattice structure and magnetic properties. We will discuss it later.

6.3.3 *Magnetic Excitations*

In order to understand the nature of magnetic properties in this unique high-spin state of cobaltates, we have studied the magnetic and spin dynamics of the system. We carried out some results from NIST on spin excitations, indicating that there is a magnetic excitation feature at ~ 3 meV at zone-center. As shown in Fig. 6.7, this feature is dispersive along *a*-axis but almost not dispersive along *c*-axis. The magnetic excitation does disappear when $T > T_N$, which is indicative of AFM spin wave excitation origin.

The complete Energy-wavevector dispersion relation is illustrated in Fig. 6.8. This low energy excitation is slightly broadened at the zone center.

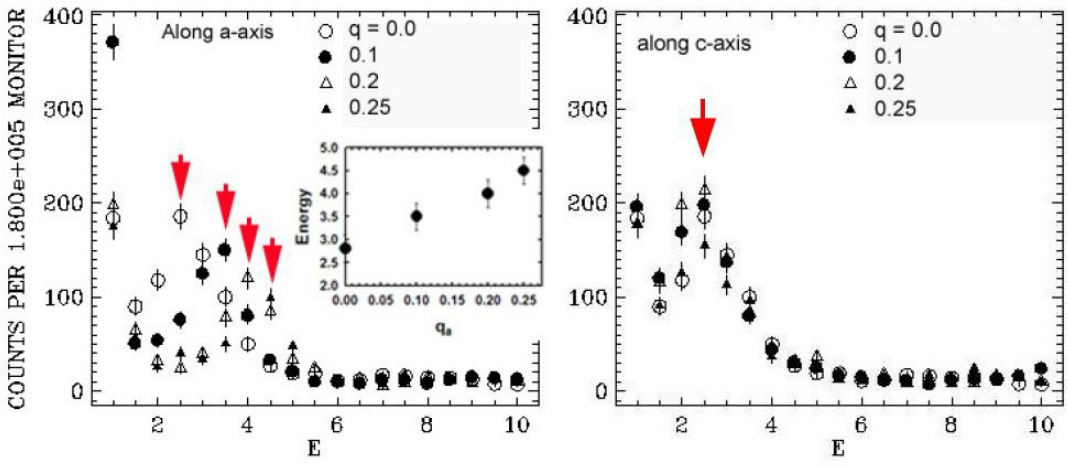

Figure 6.7 The excitation spectra along *a*-axis (left) and *c*-axis (right) from energy scans at different fixed wavevectors. The dispersion along *a*-axis is shown in the inset. The arrows indicate the positions of the excitation peak at different wavevectors.

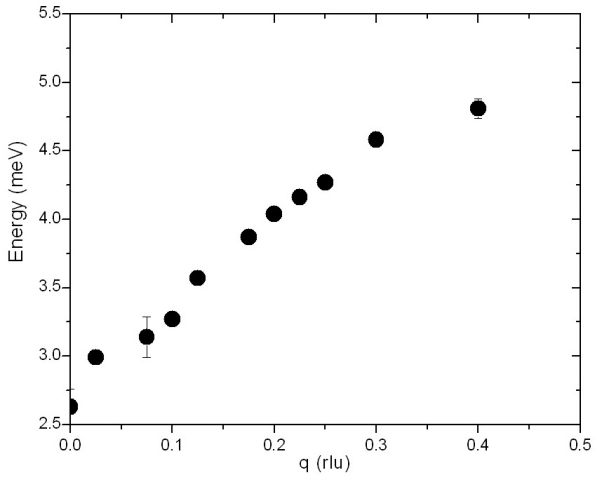

Figure 6.8 Energy scans for the complete dispersion relation along *a*-axis.

CHAPTER 7

DISCUSSION AND SUMMARY

In summary, we have successfully synthesized single crystals of $Ba_{2-x}Sr_xCoO_4$ with the doping $0 \leq x \leq 0.7$ using the floating-zone technique. The X-ray diffraction refinement results show the monoclinic structure for the doping of $0 \leq x \leq 0.4$ and orthorhombic structure forms in $0.5 \leq x \leq 0.7$. The Néel temperature T_N slightly increases in the monoclinic regime until it reaches the maximum at $x = 0.5$, then it drastically decreases when the structure converts into orthorhombic, which indicates the correlations between structure and magnetic properties. By studying the magnetic susceptibility, we confirmed this system has an antiferromagnetic ground state. The fact of a large $|\theta|/T_N$ ratio for every doping level suggests either reduced-dimensionality in spin interaction and/or the magnetic frustration.

The studies of the magnetic structure of single crystalline Ba_2CoO_4 also raise questions regarding the existence or absence of magnetic frustration and/or low-dimensional magnetic interactions, since the Curie-Weiss temperature ($\theta \sim -110$ K) is much larger than $T_N \sim 25$ K. Also, we note that $\chi(H \parallel a) \neq 0$ when $T \rightarrow 0$ K. This leads to the question of spin canting and/or the existence of defects. As stated above, the Weak transverse field μ^+SR (wTF- μ^+SR) results suggest a single second-order phase transition occurring throughout the entire volume of the sample. Neutron powder diffraction from Boulahya *et al*. [124] shows a marked difference from the μ^+SR results. Even though the transition temperature is roughly the same, the Boulahya results decrease rapidly in the 10 – 20 K range. Boulahya's NPD experiment was done on a polycrystalline sample; this might be a factor. Our more recent neutron scattering results on a single crystal sample show a temperature dependence more like that of the μ^+SR data.

Also recently, two opposing magnetic structures of Ba_2CoO_4 have been proposed. Work by Boulahya *et al*. [124] suggests that the spins are mostly aligned antiferromagnetically along the *c* axis with canting out of the *ac* plane. Their work was primarily based on an elastic neutron scattering experiment with a powder sample. We have proposed a similar magnetic structure but with the spins mostly aligned along the *a* axis (see Fig. 6.1). Since μ^+SR is highly sensitive to the local magnetic environment, it should be helpful in distinguishing which AF structure is correct via the μ^+SR results. The μ^+SR evidence shows Ba_2CoO_4 seems to have a relatively straightforward AF structure, but there remains the question of why magnetic interactions are lacking along the *c* axis. At this time there does not seem to be a single satisfactory explanation of how the magnetic moments are actually coupled.

From the μ^+SR measurements, we have observed a sharp magnetic transition in a single crystal of Ba_2CoO_4. From the wTF asymmetry we find that the whole sample enters into a magnetic phase below $T \sim 25$ K. Subsequent zero-field μ^+SR (ZF- μ^+SR) measurements clearly show the existence of static magnetic order for $T < 23$ K. The ZF-μ^+SR spectra also confirm commensurate AF order below T_N. The *T*-dependence of the ZF signals is consistent with an AF transition of the 2D-Ising type, although the CoO_4 tetrahedra are well isolated from each other. The reduced frequencies all go to zero together with a similar *T* dependence, which indicates that all muons see magnetic environments governed by the same interactions. Finally, μ^+SR verified the AF magnetic structure we proposed by probing the local magnetic environment. The spins are mostly directed along the *a* direction rather than the *c* direction. Our results, while giving basic information on the magnetic structure, still leave unresolved how the Co ions are

coupled together. Thus, this compound continues to represent interesting opportunities for further investigation.

On the other hand, Layered perovskite cobalt oxides Sr_2CoO_4 can be synthesized under high pressure and high temperature conditions. Structure refinement revealed that this compound crystallizes in K_2NiF_4–type structures with space group I4/mmm. Sr_2CoO_4 undergoes a ferromagnetic transition with $T_C = 255$ K. Low temperature magnetization data suggest the itinerant electron ferromagnetism. Fairly large negative magnetoresistance was observed for Sr_2CoO_4 near the ferromagnetic transition temperature of 255 K and in the lower temperature region. The magnetoresistance near T_C is explained by the intrinsic mechanism while that at lower temperatures is ascribed to the field suppression of the spin-dependent scattering at grain (or domain) boundaries.

It is also worth noting here that Sr_2CoO_4 can be synthesized in the form of a single-crystalline thin film with square-lattice CoO_2 sheets (K_2NiF_4-type structure). This form of compound was found to be a metallic ferromagnet, with appreciable magnetic anisotropy and quasi two-dimensional transport properties. Thus it was demonstrated that the CoO_2 layers can act as a stage for two-dimensional ferromagnetism as well as superconductivity. The fairly high T_C (250 K) of Sr_2CoO_4, which is similar to the powder material, may provide intriguing opportunities to explore the spintronic functionality of CoO_2 layers.

In future research, the objective is to explore the complete phase diagram of $Ba_{2-x}Sr_xCoO_4$ and to fully understand its unusual structural, electronic, and magnetic properties as a function of temperature and doping. We will especially focus on the doping concentration samples approaching the Sr_2CoO_4 end.

We currently prepared the single crystalline and polycrystalline samples with the doping level (x) up to 0.7. We need a high pressure growth technique when approaching Sr_2CoO_4 side although we started from Ba_2CoO_4 side. We will use elastic and inelastic neutron scattering to study the structural and magnetic properties, including their dynamics.

LIST OF REFERENCES

[1] The April 21st issue of science **288**, was dedicated to correlated electron systems, (2000).

[2] E. Dagotto. Complexity in Strongly Correlated Electron System. *Science* **309**, 257 (2005).

[3] R. J. Birgeneau and M. A. Kastner. Frontier Physics with Correlated Electrons. *Science* **288**, 437 (2000).

[4] Y. Tokura. Correlated-Electron Physics in Transition-Metal Oxides. *Phys. Today* **56**, 50 (2003).

[5] Y. Tokura and N. Nagaosa. Orbital Physics in Transition-Metal Oxides. *Science* **288**, 462 (2000).

[6] M. Imada, A. Fujimori, and Y. Tokura. Metal-Insulator Transitions. *Rev. Mod. Phys.* **70**, 1039 (1998).

[7] J. Orenstein and A. J. Millis. Advance in the Physics of High-Temperature Superconductivity. *Science* **288**, 448 (2000).

[8] Patrick A. Lee, Naoto Nagaosa, and Xiao-Gang Wen. Doping a mott insulator: Physics of high-temperature superconductivity. *Rev. Mod. Phys.* **78**, 17 (2006).

[9] Y. Maeno, H. Hashimoto, K. Yoshida, S. Nishizake, T. fujita, G. Bednorz, and F. Lichitenberg. Superconductivity in a Layered Perovskite without Copper. *Nature* **372**, 532 (1994).

[10] Yoshiteru Maeno, T. Maurice Rice, and Manfred Sigrist. The Intriguing Superconductivity of Strontium Ruthenate. *Physics Today* **54**, 42 (2001).

[11] S. Sachdev. Quantum Criticality: Competing Ground States in Low Dimensions. *Science* **288**, 475 (2000).

[12] P. Coleman and A. J. Scholfield. Quantum Criticality. *Nature* 433, 226 (2005).

[13] J. Bonča, P. Prelovšek, A. Ramšak, and S. Sarkar. *Open Problems in Strongly Correlated Electron Systems.* Kluwer Academic Publishers, (2001).

[14] J. Singleton. *Band Theory and Electronic Properties of Solids*. Oxford University Press, (2001).

[15] H. K. Onnes. On the sudden change in the rate at which the resistance of mercury disappears. *Commun. Phys. Lab. Univ. Leiden* **124C**, 1 (1911).

[16] Leon N. Cooper. Bound Electron Pairs in a Degenerate Fermi Gas. *Phys.Rev.* **104**, 1189 (1956).

[17] J. Bardeen, L. N. Cooper, and J. R. Schrieffer. Microscopic Theory of Superconductivity. *Phys. Rev.* **106**, 162 (1957).

[18] J. Bardeen, L. N. Cooper, and J. R. Schrieffer. Theory of Superconductivity. *Phys. Rev.* **108**, 1175 (1957).

[19] C. Kittel. *Introduction to Solid State Physics, 7th ed.* John Wiley & Sons, New York, (1995).

[20] J. G. Bednorz and K. A. Műller. Possible High T_C Superconductivity in the Ba-La-Cu-O System. *Z. Phys. B Cond. Matt.* **64**, 189 (1986).

[21] J. R. Waldram. *Superconductivity of Metals and Cuprates*. Institute of Physics Publishing, (1996).

[22] D. Vaknin, S. K. Sinha, D. E. Moncton, D. C. Johnston, J. M. Newsam, C. R. Safinya, and H. E. King. Antiferromagnetism in La_2CuO_{4-y}. *Phys. Rev. Lett.***58**, 2802 (1987).

[23] G. V. M. Williams, J. L. Tallon, E. M. Haines, R. Michalak, and R. Dupree. NMR Evidence for a *d*-Wave Normal-State Pseudogap. *Phys. Rev. Lett.* **78**, 721 (1997).

[24] J. M. Tranquada, D. J. Buttrey, V. Sachan, and J. E. Lorenzo. Simultaneous Ordering of Holes and Spins in $La_2NiO_{4.125}$. *Phys. Rev. Lett.* **73**, 1003 (1994).

[25] I. A. Zaliznyak, J. P. Hill, J. M. Tranquada, R. Erwin, and Y. Moritomo. Independent Freezing of Charge and Spin Dynamics in $La_{1.5}Sr_{0.5}CoO_4$. *Phys. Rev. Lett.* **85**, 4353 (2000).

[26] H. Yoshizawa, T. Kakeshita, R. Kajimoto, T. Tanabe, T. Katsufuji, and Y.Tokura. Stripe order at low temperatures in $La_{2-x}Sr_xNiO_4$ with $0.289 \leq x \leq 0.5$. *Phys. Rev. B* **61**, R854 (2000).

[27] K. McElroy, D.-H. Lee, J. E. Hoffman, K. M. Lang, J. Lee, E. W. Hudson, H. Eisaki, S. Uchida, and J. C. Davis. Coincidence of Checkerboard Charge Order and

Antinodal State Decoherence in Strongly Underdoped Superconducting $Bi_2Sr_2CaCu_2O_{8+\delta}$. *Phys. Rev. Lett.* **94**, 197005 (2005).

[28] M. v. Zimmermann, A.Vigliante, T. Niemőller, N. Ichikawa, T. Frello, J. Madsen, P. Wochner, S. Uchida, N. H. Andersen, J. M. Tranquada, D. Gibbs, and J. R. Schneider. Hard-X-ray diffraction study of charge stripe order in $La_{1.48}Nd_{0.4}Sr_{0.12}CuO_4$. *Europhys. Lett.* **41**, 629 (1998).

[29] S. B. Wilkins, P. D. Spencer, P. D. Hatton, S. P. Collins, M. D. Roper, D. Prabhakaran, and A. T. Boothroyd. Direct Observation of Orbital Ordering in $La_{0.5}Sr_{1.5}MnO_4$ Using Soft X-ray Diffraction. *Phys. Rev. Lett.* **91**, 167205 (2003).

[30] U. Schwingenschlogl and V. Eyert. Orbital Ordering in the Two-Dimensional Ferromagnetic Semiconductor Rb_2CrCl_4. *J. Magn. Magn. Mater.* **312**, L11 (2007).

[31] F. A. Kroger, H. J. Vink, and J. Volger. Resistivity, Hall Effect and Thermo-Electric Power of Conducting and Photo-Conducting Single Crystals of CDS from 20-700-Degrees-K. *Physica* **20**, 1095 (1954).

[32] R. M. Kusters, J. Singleton, D. A. Keen, R. McGreevy, and W. Hayes. Magnetoresistance Measurements on the Magnetic Semiconductor $Nd_{0.5}Pb_{0.5}MnO_3$. *Physica B: Condensed Matter* **155**, 362 (1989).

[33] R. von Helmolt, J. Wecker, B. Holzapfel, L. Schultz, and K. Samwer. Giant Negative Magnetoresistance in Perovskitelike $La_{2/3}Ba_{1/3}MnO_x$ Ferromagnetic Films. *Phys. Rev. Lett.* **71**, 2331 (1993).

[34] Ken ichi Chahara, Toshiyuki Ohno, Masahiro Kasai, and Yuzoo Kozono. Magnetoresistance in magnetic manganese oxide with intrinsic antiferromagnetic spin structure. *Applied Physics Letters* **63**, 1990 (1993).

[35] H. L. Ju, C. Kwon, Qi Li, R. L. Greene, and T. Venkatesan. Giant Magnetoresistance in $La_{1-x}Sr_xMnO_z$ Films Near Room Temperature. *Applied Physics Letters* **65**, 2108 (1994).

[36] Y Tokura, Y Tomioka, H Kuwahara, A Asamitsu, Y Moritomo, and M Kasai. Origins of Colossal Magnetoresistance in Perovskite-type Manganese Oxides. *Journal of Applied Physics* **79**, 5288 (1996).

[37] Y. Tomioka, A. Asamitsu, Y. Moritomo, H. Kuwahara, and Y. Tokura. Collapse of a Charge-Ordered State under a Magnetic Field in $Pr_{1/2}Sr_{1/2}MnO_3$. *Phys. Rev. Lett.* **74**, 5108 (1995).

[38] H. Kuwahara, Y. Tomioka, A. Asamitsu, Y. Moritomo, and Y. Tokura. A First- Order Phase-Transition Induced by a Magnetic Field. *Science* **270**, 961 (1995).

[39] Z. Jirak, S. Vratislav, and J. Zajicek. Magnetic Structure of $Pr_{0.9}Ca_{0.1}MnO_3$. *Physica Status Solidi A-Applied Research* **52**, K39 (1979).

[40] S. Nakatsuji and Y. Maeno. Quasi-Two-Dimensional Mott Transition System $Ca_{2-x}Sr_xRuO_4$. *Phys. Rev. Lett.* **84**, 2666 (2000).

[41] Metal-Insulator Transitions in Layered Ruthenates. *Materials Science and Engineering B* **63**, 70 (1999).

[42] S. Nakatsuji, D. Hall, L. Balicas, Z. Fisk, K. Sugahara, M. Yoshioka, and Y. Maeno. Heavy-Mass Fermi Liquid near a Ferromagnetic Instability in Layered Ruthenates. *Phys. Rev. Lett.* **90**, 137202 (2003).

[43] O. Friedt, M. Braden, G. André, P. Adelmann, S. Nakatsuji, and Y. Maeno. Structural and Magnetic Aspects of the Metal-Insulator Transition in $Ca_{2-x}Sr_x RuO_4$. *Phys. Rev. B* **63**, 174432 (2001).

[44] Andrew Peter Mackenzie and Yoshiteru Maeno. The Superconductivity of Sr_2RuO_4 and the Physics of Spin-Triplet Pairing. *Rev. Mod. Phys.* **75**, 657 (2003).

[45] Z. Fang and K. Terakura. Magnetic Phase Diagram of $Ca_{2-x}Sr_xRuO_4$ Governed by Structural Distortions. *Phys. Rev. B* **64**, 020509 (2001).

[46] S. N. Ruddlesden and P. Popper. New Compounds of the K_2NiF_4 Type. *Acta Crystallographica* **10**, 538 (1957).

[47] V. G. Bhide, D. S. Rajoria, G. R. Rao, and C. N. R. Rao. Mőssbauer Studies of the High-Spin-Low-Spin Equilibria and the Localized-Collective Electron Transition in $LaCoO_3$. *Phys. Rev. B* **6**, 1021 (1972).

[48] K. Asai, P. Gehring, H. Chou, and G. Shirane. Temperature-induced Magnetism in LaCoO3. *Phys. Rev. B* **40**, 10982 (1989).

[49] M. Itoh and I. Natori. Hole-Doping Effect on the Spin State and Microscopic Magnetic Properties of $La_{1-x}Sr_xCoO_3$ ($0 \leq x \leq 0.5$): ^{59}Co and ^{139}La NMR Measurements. *J. Phys. Soc. Jpn.* **64**, 970 (1995).

[50] M. Abbate, J. C. Fuggle, A. Fujimori, L. H. Tjeng, C. T. Chen, R. Potze, G. A. Sawatzky, H. Eisaki, and S. Uchida. Electronic Structure and Spin-state Transition of LaCoO3. *Phys. Rev. B* **47**, 16124 (1993).

[51] S. R. Barman and D. D. Sarma. Photoelectron-spectroscopy Investigation of the Spin-state Transition in $LaCoO_3$. *Phys. Rev. B* **49**, 13979 (1994).

[52] S. Yamaguchi, Y. Okimoto, H. Taniguchi, and Y. Tokura. Spin-state Transition and High-spin Polarons in $LaCoO_3$. *Phys. Rev. B* **53**, R2926 (1996).

[53] Y. Moritomo, K. Higashi, K. Matsuda, and A. Nakamura. Spin-state transtion in layered perovskite cobalt oxides: $La_{2-x}Sr_xCoO_4$ ($0.4 \leq x \leq 1.0$). *Phys. Rev. B* **55**, R14725 (1997).

[54] M. Cwik, M. Benomar, T. Finger, Y. Sidis, D. Senff, T. Lorenz, and M. Braden. Magnetic Correlations in $La_{2-x}Sr_xCoO_4$ Studied by Neutron Scattering: Possible Evidence for Stripe Phases. *Phys. Rev. Lett.* **102**, 057201 (2009).

[55] K. Takada, H. Sakurai, E. Takayama-Muromachi, F. Izumi, R. A. Dilanian, and T. Sasaki. Superconductivity in Two-dimensional CoO_2 Layers. *Nature* **422**, 53 (2003).

[56] A. R. Moodenbaugh, Youwen Xu, M. Suenaga, T. J. Folkerts, and R. N. Shelton. Superconducting Properties of $La_{2-x}Ba_xCuO_4$. *Phys. Rev. B* **38**, 4596 (1988).

[57] P. G. Radaelli, D. G. Hinks, A. W. Mitchell, B. A. Hunter, J. L. Wagner, B. Dabrowski, K. G. Vandervoort, H. K. Viswanathan, and J. D. Jorgensen. Structural and Superconducting Properties of $La_{2-x}Sr_xCuO_4$ as a Function of Sr content. *Phys. Rev. B* **49**, 4163 (1994).

[58] Yimei Zhu, A. R. Moodenbaugh, Z. X. Cai, J. Tafto, M. Suenaga, and D. O. Welch. Tetragonal-Orthorhombic Structural Modulation at Low Temperature in $La_{2-x}Ba_xCuO_4$. *Phys. Rev. Lett.* **73**, 3026 (1994).

[59] J.-S. Zhou and J. B. Goodenough. Electron-Lattice Coupling and Stripe Formation in $La_{2-x}Ba_xCuO_4$. *Phys. Rev. B* **56**, 6288 (1997).

[60] Spin State Equilibria and the Semiconductor to Metal Transition of $LaCoO_3$. *Solid State Communications* **44**, 1213 (1982).

[61] Suzanne R. English, J. Wu, and C. Leighton. Thermally Excited Spin-Disorder Contribution to the Resistivity of $LaCoO_3$. *Phys. Rev. B* **65**, 220407 (2002).

[62] S. J. Blundell. *Magnetism in Condensed Matter*. Oxford University Press, (2001).

[63] P. M. Raccah and J. B. Goodenough. First-Order Localized-Electron Collective-Electron Transition in $LaCoO_3$. *Phys. Rev.* **155**, 932 (1967).

[64] Y. Kobayashi, Thant Sin Naing, M. Suzuki, M. Akimitsu, K. Asai, K. Yamada, J. Akimitsu, P. Manuel, J. M. Tranquada, and G. Shirane. Inelastic Neutron Scattering Study of Phonons and Magnetic Excitations in $LaCoO_3$. *Phys. Rev. B* **72**, 174405 (2005).

[65] M. Cwik, M. Braden, M. Kriener, and K. Schmalzl. I.L.L Exp. Report CRG, (2005).

[66] A. P. Ramirez. Colossal Magnetoresistance. *Journal of Physics: Condensed Matter* **9**, 8171 (1997).

[67] E. Dagotto. *Nanoscale Phase Separation and Colossal Magnetoresistance - The Physics of Manganites and Related Compounds*. Springer, (2003).

[68] M. N. Baibich, J. M. Broto, A. Fert, F. Nguyen Van Dau, F. Petroff, P. Etienne, G. Creuzet, A. Friederich, and J. Chazelas. Giant Magnetoresistance of (001)Fe /(001)Cr Magnetic Superlattices. *Phys. Rev. Lett.* **61**, 2472 (1988).

[69] M. Kriener, C. Zobel, A. Reichl, J. Baier, M. Cwik, K. Berggold, H. Kierspel, O. Zabara, A. Freimuth, and T. Lorenz. Structure, Magnetization, and Resistivity of $La_{1-x}M_xCoO_3$ (M = Ca, Sr, and Ba). *Phys. Rev. B* **69**, 094417 (2004).

[70] J. Wu, H. Zheng, J. F. Mitchell, and C. Leighton. Glassy Transport Phenomena in a Phase-Separated Perovskite Cobaltite. *Phys. Rev. B* **73**, 020404 (2006).

[71] J. Wu and C. Leighton. Glassy Ferromagnetism and Magnetic Phase Separation in $La_{1-x}Sr_xCoO_3$. *Phys. Rev. B* **67**, 174408 (2003).

[72] Von Hj. Mattausch and Hk G. A. Candela, A. H. Kahn, and T. Negas.. Műller-Buschbaum. The Understanding of Ba_2CoO_4. *Z. Anorg. Allg. Chem.* **386**, 1 (1971).

[73] G. A. Candela, A. H. Kahn, and T. Negas. Magnetic Susceptibility of Co^{4+} (d^5) in Octahedral and Tetrahedral Environments. *J. Solid State Chem.* **7**, 360 (1973).

[74] K. Boulahya, M. Parras, A. Vegas, and J. M. González-Calbet. A Comparative Crystal Chemical Analysis of Ba_2CoO_4 and $BaCoO_3$. *Solid State Sci.* **2**, 57 (2000).

[75] J. Matsuno, Y. Okimoto, Z. Fang, X. Z. Yu, Y. Matsui, N. Nagaosa, M. Kawasaki, and Y. Tokura. Metallic Ferromagnet with Square-Lattice CoO2 Sheet. *Phys. Rev. Lett.* **93**, 167202 (2004).

[76] X. L. Wang, H. Sakurai, and E. Takayama-Muromachi. Synthesis, Structures, and Magnetic Properties of Novel Roddlesden-Popper Homologous Series $Sr_{n+1}Co_nO_{3n+1}$ (n = 1,2,3,4, and ∞). *J. Appl. Phys.* **97**, 10M519 (2005).

[77] X. L. Wang and E. Takayama-Muromachi. Magnetic and Transport Properties of the Layered Perovskite System $Sr_{2-y}Y_yCoO_4$ ($0 \leq y \leq 1$). *Phys. Rev. B* **72**, 064401 (2005).

[78] M. Kidwai. Dry media reactions. *Pure Appl. Chem*. **73**, 147 (2001).

[79] A. Barone. *Principles and Applications of Superconducting Quantum Interference Devices*. World Scientifc, (1992).

[80] Quantum Design Inc. *PPMS Manual*, *11th edition*. Quantum Design Inc., (2004).

[81] G. L. Squires. *Introduction to the Theory of Thermal Neutron Scattering*. Dover Publications Inc, Mineola, New York, (1996).

[82] A. J. Freeman. Atomic Scattering Factors for Spherical and Aspherical Charge Distributions. *Acta Crystallographica* **12**, 261 (1959).

[83] S. Shamoto, M. Sato, J. M. Tranquada, B. J. Sternlieb, and G. Shirane. Neutron-scattering Study of Antiferromagnetism in $YBa_2Cu_3O_{6.15}$. *Phys. Rev. B* **48**, 13817 (1993).

[84] W. I. F. David, K. Shankland, L.B. McCusker, and Ch. Baerlocher. *Structure Determination from Powder Diffraction Data*. Oxford University Press, (2002).

[85] A.K. Cheetam and Angew A.P. Wilkinson. Synchrotron X-ray and Neutron Diffraction Studies in Solid-State Chemistry. *Angew. Chemie Int. Ed. Engl*. **31**, 1557 (1992).

[86] K.D.M. Harris. Crystal Structure Determination from Powder Diffraction Data. *Tremayne Chem. Mater.* **8**, 2554 (1996).

[87] J.I. Langford and D. Louer. Powder diffraction. *Rep. Prog. Phys*. **59**, 131 (1996).

[88] D. M. Poorjay and A. Clearfield. Application of X-ray Powder Diffraction Techniques to the Solution of Unknown Crystal Structures. *Acc. Chem. Res*. **30**, 414 (1997).

[89] A. Meden. Crystal Structure Solution from Powder Diffraction Data - State of the Art and Perspectives. *Croat. Chem. Acta*. **71**, 615 (1998).

[90] K.D.M. Harris, M.Tremayne, and B.M. Kariuki. Contemporary Advances in the Use of Powder X-Ray Diffraction for Structure Determination. *Angew. Chemie Int. Ed.* **40**, 1626 (2001).

[91] A. Le Bail. Trends in structure determination by powder diffractometry. *Advances in Structure Analysis*, (1998).

[92] Juan Rodríquez-Carvajal. Structural analysis from powder diffraction data the rietveld method. *Ecole Thématique: Cristallographie et Neutrons*, (1997).

[93] T. Negas and R.S. Roth. *Solid State Chem.* **364**, 233 (1972).

[94] Computer code saint, v. 5.04, (1995).

[95] G. M. Sheldrick. *Computer code SHELXTL v. 5.0*. Siemens Analytical X-ray Instruments, Inc., (1994).

[96] R. H. Blessing. *Acta Crystallogr., Sect. A: Found. Crystallogr.* **51**, 33 (1995).

[97] Computer code genimi, v. 1.02, (2000).

[98] M.C. Burla, R. Caliandro, M. Camalli, B. Carrozzini, G.L. Cascarano, L. DeCaro, C. Giacovazzo, G. Polidori, and R. Spagna. *J. Appl. Cryst.* **38**, 381 (2005).

[99] Shelxtl 6.12, (1997).

[100] J. Matsuno, Y. Okimoo, M. Kawasaki, and Y. Tokura. Variation of the Electronic Structure in Systematically Synthesized Sr_2MO_4 (M = Ti, V, Cr, Mn, and Co). *Phys. Rev. Lett.* **95**, 176404 (2005).

[101] M. A. Se□arís-Rodríquez and J.B. Goodenough. Magnetic and Transport Properties of the System $La_{1-x}Sr_xCoO_{3-\delta}$ ($0 < x \leq 0.50$). *J. Solid State Chem.***118**, 323 (1995).

[102] J.B. Goodenough. Coexistence of localized and itinerant *d* electrons. *Mater. Res. Bull.* **6**, 967 (1971).

[103] P. Ravindran, P. Korzhavyi, H. Fjellvag, and A. Kjekhus. Electronic structure, phase stability, and magnetic properties of La1-xSrxCoO3 from first-principles full-potential calculations. *Phys. Rev. B* **60**, 16423 (1999).

[104] R. Potze, G.Sawatzky, and M.Abbate. Possibility for an intermediate-spin ground state in the charge-transfer material $SrCoO_3$. *Phys. Rev. B* **51**, 11501 (1995).

[105] F. Fauth, E. Suard, and V. Caignaert. Intermediate spin state of Co^{3+} and Co^{4+} ions in $La_{0.5}Ba_{0.5}CoO_3$ evidenced by Jahn-Teller distortions. *Phys. Rev. B* **65**, 060401(R) (2002).

[106] T. Matsuura, J. Tabuchi, J. Mizusaki, Y. Yamauchi, and K. Fueki. Electrical properties of $La_{2-x}Sr_xCoO_4$-I: Structure, electrical conductivity, and Seebeck coefficient of single crystals (x = 0.0, 0.5, 1.0 and 1.5). *J. Phys. Chem. Solids* **49**, 1403 (1988).

[107] T. Matsuura, J. Tabuchi, J. Mizusaki, Y. Yamauchi, and K. Fueki. Electrical properties of $La_{2-x}Sr_xCoO_4$-II: Models and analysis of the relationship between cobalt 3*d* electron state and structural, electrical and magnetic properties. *J. Phys. Chem. Solids* **49**, 1409 (1988).

[108] Y. Furulakawa, S. Wada, and Y. Yamada. Phase Transition from Antiferromagnetic Insulator to Ferromagnetic Metal in $La_{2-x}Sr_xCoO_4$: Magnetization and NMR Studies. *J. Phys. Soc. Jpn.* **62**, 1127 (1983).

[109] E. Iguchi, H. Nakatsugawa, and K. Futakuchi. Polaronic Conduction in $La_{2-x}Sr_xCoO_4$ ($0.25 \leq x \leq 1.10$) below Room Temperature. *J. Solid State Chem.* **139**, 176 (1998).

[110] M. Itoh, M. Mori, Y. Moritomo, and A. Nakamura. NMR study of the spin state and magnetic properties of layered perovskite cobalt oxides $La_{2-x}Sr_xCoO_4$. *Physica B* **259**, 997 (1999).

[111] J. Wang, W. Zheng, and D. Y. Xing. Magnetic structure of the layered perovskite $LaSrCoO_4$. *Phys. Rev. B* **62**, 14140 (2000).

[112] J. Wang, Y. C. Tao, W. Zheng, and D. Y. Xing. Theoretical study on the spin-state transition in doped $La_{2-x}Sr_xCoO_4$. *J. Phys.: Condens. Matter* **12**, 7425 (2000).

[113] K. Lukaszewicz. Die Kristallstruktur Einiger Strontium und Bariumtitanate. *Angew. Chem. Int. Ed.* **70**, 320 (1958).

[114] N. W. Ashcroft and N. D. Mermin. *Solid State Physics*. Holt, Rinehart and Winston, New York, (1976).

[115] L. J. de Jongh and A. R. Miedema. Experiments on Simple Magnetic Model Systems. *Adv. Phys.* **23**, 1 (1974).

[116] A. P. Ramirez. Geometrically Frustrated Matter - Magnets to Molecules. *MRS Bull*. **30**, 447 (2005).

[117] E. S. R. Gopal. *Specific Heats at Low Temperatures*. Plenum Press, New York, (1966).

[118] B. C. Sales, D. Mandrus, and B. C. Chakoumakos. *Recent Trends in Thermoelectric Materials Research II*, volume 70. Academic Press, New York, (2001).

[119] N. F. Mott. *Metal-Insulator Transitions*. Taylor and Francis, London, (1974).

[120] W.A. Phillips. Two-Level States in Glasses. *Rep. Prog. Phys.* **50**, 1657 (1987).

[121] J. A. Bland. The Crystal Structure of Barium Orthotitanate, Ba_2TiO_4. *Acta Crystallogr.* **14**, 875 (1961).

[122] M. Jansen and R. Hoppe. Neue Oxocobaltate (IV): $K_6[Co_2O_7]$ und Li_4CoO_4. Naturwissenschaften **60**, 104 (1973).

[123] R. Jin, Hao Sha, P. G. Khalifah, R. E. Sykora, B. C. Sales, D. Mandrus, and Jiandi Zhang. Ba_2CoO_4: Crystal Growth, Structure Refinement, and Physical Properties. *Phys. Rev. B* **73**, 174404 (2006).

[124] K. Boulahya, M. Parras, J. M. González Galbet, U. Amador, J. L. Martínez, and M. T. Fernández Díaz. Structural, Magnetic, and Electrical Behavior of Low Dimensional Ba_2CoO_4. *Chem. Mater.* **18**, 3898 (2006).

VITA

HAO SHA

January, 1979	Born, Nanjing, Jiangsu, P. R. China
1997 – 2001	B. S., Physics Nanjing University, Nanjing, P. R. China
2001 – 2003	Research Assistant Nanjing University, Nanjing, P. R. China
2003 – 2004	Teaching Assistant Physics, University of Miami Miami, Florida, USA
2004 – present	Doctoral Candidate, Teaching/Research Assistant Physics, Florida International University Miami, Florida, USA

PUBLICATIONS

1. P. L. Russo, J. Sugiyama, J. H. Brewer, E. J. Ansaldo, S. L. Stubbs, Y. Ikedo, K. Mukai, K. H. Chow, R. Jin, H. Sha, and J. Zhang, Muon Spin Rotation/Relaxation Study of Ba_2CoO_4, Phys. Rev. B **80**, 104421 (2009).

2. Hao Sha, F. Ye, Pengcheng Dai, J. A. Fernandez-Baca, D.Mesa, J. W. Lynn, Y. Tomioka, Y. Tokura, and Jiandi Zhang, Signature of Magnetic Phase Separation in the Ground State of $Pr_{1-x}Ca_xMnO_3$, Phys. Rev. B **78**, 052410 (2008).

3. Jiandi Zhang, F. Ye, Hao Sha, Pengcheng Dai, J. A. Fernandez-Baca, and E. W. Plummer, Magnons in Ferromagnetic Metallic Manganites, J. Phys.: Condens. Matter **19**, 315204 (2007).

4. R. Jin, Hao Sha, P. Khalifah, R. E. Sykora, B. C. Sales, D. Mandrus, and Jiandi Zhang, Ba_2CoO_4: Crystal Growth, Structure Refinement, and Physical Properties, Phys. Rev. B **73**, 174404 (2006).

5. F. Ye, Pengcheng Dai, J. A. Fernandez-Baca, Hao Sha, J. W. Lynn, H. Kawano-Furukawa, Y. Tomioka, Y. Tokura, and Jiandi Zhang, Evolution of Spin-Wave Excitations in Ferromagnetic Metallic Manganites, Phys. Rev. Lett. **96**, 047204 (2006).

6. W. S. Tan, B. Shen, H. Sha, H. L. Cai, X. S. Wu, Y. D. Zheng, S. S. Jiang, W. L. Zheng, Q. J. Jia, and Q. He, Microstructures and Strain Relaxation in Modulation-doped $Al_xGa_{1-x}N$/GaN Heterostructures, International Journal of Modern Physics B **18**, 989 (2004).

7. H. Sha, X. S. Wu, Y. M. Xu, A. Hu, and S. S. Jiang, X-Ray Diffraction Studies on Yttrium-Doped $La_{0.67}Ca_{0.33}MnO_3$, Journal of Superconductivity **17**, 247 (2004).

8. W. S. Tan, L. Yang, H. Sha, X. S. Wu, J. Gao, and S. S. Jiang, Surface Structure and Transport Properties of $YBa_2Cu_3O_{7-\delta}$ Using $La_{2/3}Ca_{1/3}MnO_3$ as Buffer, Surface Review and Letters **10**, 317 (2003).

9. TAN Weishi, SHA Hao, SHEN Bo, et al., Microstrain in Modulation-Doped $Al_xGa_{1-x}N$/GaN Heterostructures, Nuclear Techniques (Chinese) **25**, 799 (2002).

10. W. S. Tan, X. S. Wu, H. Sha, and S. S. Jiang, Resistivity Behavior of $La_{0.67}Ca_{0.33}MnO_3/YBa_2Cu_3O_{7-delta}$ Epitaxial Heterostructure, International Journal of Modern Physics B **16**, 3847 (2002).

11. X. S. Wu, H. Sha, W. S. Tan, Tao Yu, A. Hu, and S. S. Jiang, The Crystal Structure of $La_{0.7}Pr_{0.3}Ba_2Cu_3O_d$ Ceramic Compound, Powder Diffraction **17**, 25 (2002).